Novel Physical Security Devices Exploiting the Optical Properties of Low-Dimensional Materials

---

Matthew James Fong

Department of Physics

Lancaster University
March 2022

This thesis is submitted in partial fulfilment of the requirements for the degree of Doctor of Philosophy

Preface

This thesis is the result of work which I performed at Lancaster University, between October 2017 and July 2021. Except where otherwise stated the contents of this thesis are the results of my own work, and is not the same as any others I have already submitted, or in the process of submitting, for any degree at any university or institution. The word count on this thesis does not exceed the maximum limit of 80,000 words.

M. J. Fong

“Ambition is a funny thing. It tends to take you on a
journey away from where you started. That's fine, maybe inevitable. But no one ever
tells you that the biggest days aren't always the best days. And the richest prizes
aren't the ones you remember.”

Andrew ‘Freddie’ Flintoff

Acknowledgements

"Go Well."

During my time as a PhD student, I have worked with and made friends with many people, without whom this thesis would not have been possible. Firstly, the utmost thanks must be given to my supervisor, Prof. Rob Young, for his continued guidance, support and direction: this thesis would not exist without your help. Thanks also to Dr Ben Robinson for his invaluable help and advice during the project, which has aided my experiments throughout.

Next, I'd like to extend my thanks to the wider group members, past and present. Each of you have all helped me in some way, either helping in the lab, for constructive chats, or well-needed coffee breaks: Alex, Angelo, Elliott, Fangling, Kieran, Leo, Marta, Nema, Somak, Ramón, Tom, Yameng, and, in particular, Chris, who helped with much of my lab work, and made the lab and the office a fun place to work.

I must thank my friends and family who have made my time in Lancaster so enjoyable. There are too many of you to list, including coffee club customers, pub regulars (Rip Grad bar), lunchtime shed players, Aroma Chef trippers, and Lake District walkers, but I'd like to particularly thank Tom McGrath, for chaotic adventures in China and putting up with my grumbles in the office; Josh Chawner, Theo Noble and Xiao Collins for various adventures and cricket musings; and Elliott Ball, for being a new Three Mariners regular.

Special thanks go to John Hardy, who gave me the opportunity to do some weird science in chemistry over the last year.

Finally, thank you to Mum, Dad and Rebecca for their endless support, and to Charlotte, for your unconditional love and patience.

"Cheers!"

Greg James, Felix White, James Anderson

Contributions

The fabrication of the samples discussed in Chapters 4 and 5, including electro spray deposition of quantum dots, and photolithography for aluminium arrays were performed by C. Woodhead and N. Abdelazim at Lancaster University. Scanning electron microscopy images of AuNP distributions were taken by C. Woodhead. Deposition of dielectric films of TiO_2 and Al_2O_3 was performed by A. Jones and K. Lulla at Lancaster University. AFM characterisation of the liquid-phase exfoliated MoS_2 inks was performed by A. Lamantia.

List of Publications

M. Fong, C. Woodhead, N. Abdelazim, D. Abreu, A. Lamantia, E. Ball, K. Longmate, D. Howarth, B. Robinson, P. Speed, R. Young, "*Using intrinsic properties of quantum dots to increase security when uniquely identifying devices*", Accepted for publication, Scientific Reports, 2022

A.Lamantia, X.Wang, **M.J.Fong**, M.Mucientes, L.Forcieri, S.Jarvis, O.Kolosov, R.J.Young, and B.J. Robinson, "*Tailoring optical and electrical properties in monolayer of MoS2 using non-covalent bonded interspacer self-assembled monolayer of Fullerene*", Under Preparation, 2022

N. Abdelazim, **M. J. Fong**, T. McGrath, C. Woodhead, F. Al-Saymari, I.E. Bagci, A. Jones, X. Wang, R. Young, "*Hotspot Generation for Unique Identification with Nanomaterials*", Scientific Reports 11, 1528, (2021).

Elliott M. Ball, Kieran Longmate, Joonas Majaniemi, Angelo Lamantia, Daniel Abreu, **Matthew J. Fong** and Robert J. Young, "*Smartphone-based Fingerprint Extraction from Quantum-Optical PUFs*", Under Submission, IEEE Transactions on Information Forensics & Security, 2022

Sara J. Baldock, Punarja Kevin, Garry R. Harper, Zhiyi Zhao, Zijian Zhang, Yaochun Shen, Hungyen Lin, **Matthew J. Fong**, Mark D. Ashton, Mathew J. Haskew, Rebecca Griffin, Jack R. Martin, Catherine Au, Olga Efremova, Reza N. Esfahani, Hedley Emsley, Alexandre Benedetto, John B. Appleby, Beverly Stewart, David Cheneler, Damian M. Cummings* and John G. Hardy, "*Creating 3D objects with integrated electronics via multiphoton fabrication*", Under Submission, Advanced Materials Technologies, 2022

Abstract

The works in this thesis discuss mechanisms to improve the intrinsic security of nanomaterial-based optical physical unclonable functions (O-PUFs). A PUF is an object which is very difficult or physically impossible to replicate or predict, the security of which originates from random properties which arise during device fabrication, either naturally (implicit), or induced (explicit). Many different PUFs have been discussed and developed for several applications, where each implementation requires the satisfaction of several key figures of merit to be both secure and practical. PUFs are attractive as unique objects in the field of anti-counterfeiting, as secure alternatives to other optical means, including holograms and watermarks.

This thesis aims to demonstrate and validate modifications in measurement and construction to quantum-confined optical semiconductors as the basis of an effective O-PUF. The optical properties of quantum dots and 2D materials are exploited, utilising their nonlinear optical response and sensitivity to local defects to improve the PUF's evaluability and entropy density.

The works presented here propose three modifications to an existing category of O-PUF to improve their robustness against replay and simulation attacks and increase their overall entropy density.

Firstly, the measurement technique of QD-based O-PUFs is modified: several O-PUFs are based on the position of, or scattering from, optical nanoparticles, so a verification technique of a quantum dot-based O-PUF utilising the fundamental optical properties of the quantum dots used in the tag is developed, ensuring simulation attacks are more difficult. Secondly, the optical emission from the QDs in an O-PUF are modified with the addition of plasmonic nanoparticles, locally enhancing the electromagnetic field to create photoluminescence emission 'hotspots' to image the dynamic range of emission peak intensity. Finally, the fabrication of O-PUFs using optically emitting 2D materials is explored, instead of quantum dots (QDs), which potentially paves the way for cheaper, easier to fabricate quantum O-PUFs.

Table of Contents

Chapter 1

Introduction and Motivation

1.1 Unique Objects

The modern world is striving towards continuous interconnectivity and dependencies on trust and authentication. The security and authenticity of electronic devices and physical objects are necessary for trust to be achieved. However, with any desirable object of value, from banknotes to pharmaceuticals, there is a continuous arms race between nefarious parties producing counterfeited goods and genuine goods and identities. The requirement for security devices in modern society has become ubiquitous, from authenticating online identities to verification of banknotes and protecting goods from counterfeiting. The game of cat and mouse wherein counterfeiters attempt to clone, forge, or impersonate real devices, tags, or identities is leading to the development of increasingly complex security devices. A common solution is holograms, which require complex fabrication methods to ensure they are detailed and complicated enough to be difficult to copy, but use a technique that is repeatable, such that each tag is identical. The consequence of this symmetrical mechanism is that it is complex and difficult to fabricate identical units repeatedly. However, the repeatability of their fabrication method is the intrinsic flaw with this concept. Additionally, to be secure, they also require knowledge on behalf of the consumer to know how the genuine tag should appear: whilst it may be difficult to counterfeit a genuine tag accurately, a consumer may not have the required knowledge to verify it is an authentic hologram, so a ‘good’ counterfeit is likely to be sufficient.

Conversely, a fundamental property of a physical unclonable function (PUF) is that all devices are individually unique as a natural consequence of the fabrication technique. In all types of PUF, the intrinsic security arises from the non-reproducibility of the fabrication method. This work uses the non-reproducibility of the spatial emission properties of low-dimensional optically active semiconductors. Originally, PUFs were based on the scattering of incident light on an array of randomly deposited particles, set in a resin[1]. This random scatter pattern (response) is unique to the given challenge from a laser, which arises from the unpredictable fabrication method. It is this key principle of uniqueness that is used throughout this work for all PUFs, wherein both the random fabrication process and unpredictable nature of the emission properties yield a unique response for each device.

1.2 Thesis Outline

The work described in this thesis aims to demonstrate the potential of using optical low-dimensional semiconductors as the foundation of an optical physical unclonable function (O-PUF, to pave the way for these devices to be ubiquitous.

Firstly, the measured non-linear emission properties of electrospray-deposited colloidal quantum dots (CQDs) on a surface is used as an initial method of authentication for these tags. Next, the overall dynamic range of these QD-PUFs is improved to increase the overall number of challenge-response pairs available to an authenticator, with the addition of plasmonic nanoparticles. This increases the number of challenge-response pairs (CRPs) available in the same size device, increasing its security. Finally, the potential and efficacy of optically emitting direct band gap 2D materials (WS_2) as O-PUFs are investigated, with both natural and induced localised defects using plasmonic nanoparticles, to reduce their cost and toxicity.

Chapter 2 introduces key figures of merit and properties of O-PUFs, laying the foundational principles of O-PUF design, and discusses the current state-of-the-art in nanomaterial-based PUF, followed by the shortcomings or areas for potential improvements that exist in the literature. Next, the fundamental concepts of semiconductor physics relevant to low dimensional materials is discussed, including their optical properties, quantum confinement, and how local plasmons can affect the local electromagnetic field.

Chapter 3 introduces the key methods for fabrication of the O-PUFs, including nanoparticle deposition and 2D material preparation. Subsequently, the characterisation methods of these devices for verification and interrogation including microscopy and optical spectroscopy methods are detailed.

Chapter 4 introduces the concept of colloidal quantum dots (CQDs) for a secure O-PUF. The optical emission response of QDs is intrinsically nonlinear when excited by a linear excitation source. The motivation for this chapter is to discuss the feasibility of an additional verification step for QD O-PUFs to confirm the presence of quantum emitters. This check for a nonlinear pattern as part of the authentication process verifies quantum material is present on the surface of the tag, reducing the opportunities for replay attacks. Subsequently, plasmonic gold nanoparticles (AuNPs) are introduced as a means of modifying the local electromagnetic field to enhance the emission intensity at random points over the sample, improving the overall dynamic range of emission. This technique increases the number of challenge-response pairs (CRPs) available, increasing the sample's entropy density, and therefore the relative security of the tag. It generates a new dimension of challenge for this classification of PUF, of not only the NP's position, but also their relative emission intensity.

Chapter 5 then develops the model of constellation style O-PUF with plasmonic nanomaterials, but moves from QDs to 2D materials, adding plasmonic nanoparticles to the substrate underneath a layer of micro mechanically exfoliated WS_2. Again, this modifies locally the emission properties of the flakes by introducing an enhanced electromagnetic field and inducing local defects. 2D materials have some properties which are advantageous over quantum dots in the application of O-PUFs, including cost and toxicity.

Finally, the key results of this work are summarised, and potential future developments, modifications and improvements of quantum O-PUFs using low-dimensional optical materials are discussed in Chapter 6.

The work presented in this thesis was conducted between October 2017 and March 2021. Whilst I was able to perform the experiments for the contents of the works as planned, due to interruptions to lab time and availability due to COVID-19, some of the experiments planned to be completed in Chapter 6 have instead been introduced as potential future experimental works or modifications.

Chapter 2

Physical Unclonable Function Background and Semiconductor Device Theory

This chapter introduces physical unclonable functions (PUFs) as unique objects. Existing optical PUFs (O-PUFs) are introduced, detailing their key figures of merit (FoMs), including high entropy density with a large number of challenge-response pairs (CRPs), evaluability, and uniqueness. A discussion of the properties of optical semiconductor nanostructures then introduces how the use of QDs and 2D materials can help improve O-PUF FoMs. Current O-PUFs are discussed, with their key properties and advantages, and what potential remains for modifications and improvements. Subsequently, some of the fundamental concepts of semiconductor and semiconductor device physics, which are relevant for understanding the properties of low-dimensional semiconductor PUFs, are introduced, including their band structures, optical properties, and their sensitivity to defects. Finally, the concept and mechanism of plasmonic enhancement using noble-metal plasmonic nanoparticles, is introduced and discussed.

2.1 Physical Unclonable Functions

A PUF is a form of unique primitive, which is able to generate a set of responses to a given challenge, in the form of CRPs[2]. There are several key figures of merit that must be addressed and satisfied for a device to be an effective and scalable PUF. Scalability in PUF fabrication is important to enable the requirement for large numbers of these unique devices to be fabricated using a facile mechanism. Here, the current state-of-the-art in O-PUF development is established, through their key FoMs, followed by a discussion of existing O-PUFs, how they satisfy these FoMs, and what challenges remain in this field.

There are many types of PUF that have wide-ranging applications within the identification and authentication space: the focus of this thesis are O-PUFs. These are devices that, under interrogation from an external source, exhibit a unique optical pattern. Common O-PUF types involve the random distribution of optical nanomaterials, which interact with incident light to generate a unique response. The security of these devices arises from the unpredictable nature of their fabrication method.

2.1.1 Explicit and Implicit Randomness

Fabrication techniques of PUFs, and the random responses to a given challenge they create, can be divided into two broad classifications: explicit and implicit variations[2]. Explicit random variations arise from a fabrication procedure designed with steps to intentionally introduce random features, which in turn form the basis of the unique response when challenged. Conversely, implicit variations arise naturally during the fabrication process. The works discussed in this thesis utilise both of these variations: the fabrication mechanisms of the O-PUFs introduced here have implicit randomness, but additional modifications are introduced to improve the optical properties of the tag and introduce an extrinsic source of randomness.

2.1.2 Strong and Weak PUFs

For completeness, here a distinction between two types of PUF is introduced. Strong and weak are terms which describe the relative effectiveness and CRP density a certain type of PUF can hold. This is closely related to how the bit and CRP density scales with PUF size. A PUF design with a bit density that scales as a low-order polynomial is classified as a weak PUF. Weak PUFs generally rely on fewer challenges[3] . It is conceivable that, whilst a weak PUF cannot be cloned, it may be possible for a nefarious party to replicate the set of responses to a given challenge. Conversely, a strong PUF has a much higher number of CRPs, which increase with a high-order polynomial or exponentially with device size.

2.1.3 Physical Unclonable Function Figures of Merit

There are several FoMs in the design and fabrication of PUFs that must be considered to create an effective PUF. These range from the requirement for the PUF to have a high level of security with a high bit density, to being practical for fabrication and interrogation for applications in the real world. Not all are within the scope of this thesis, but the fundamental key properties of O-PUFs which are relevant to the improvements discussed in this work are introduced and detailed here[2]. This work will refer to these FoMs throughout, to demonstrate areas of improvement in O-PUF design and the justification for their inclusion.

2.1.3.1 Entropy Density

Firstly, and importantly, to be unique on a scale that is practicable for real-world use, a PUF must have a sufficiently high entropy density. Stronger PUFs are able to support a larger set of CRPs, to the extent where a 'strong PUF' is defined such that it is impractical for an attacker to record all possible sets. The entropy density for a given PUF is the amount of potential information which can be stored per area for a given device from the particular entropy source. The larger the number of sets of CRPs an individual device is able to support, the more secure it can be considered to be, but it should be balanced with the practicality of sample size and measurement resolution. A high entropy density for O-PUFs, such as the type developed in this work, can be created using a few techniques, which form the works in this thesis. A PUF based on optical emission can store more bits by increasing either the dynamic range of optical properties of the device, the size of the device, or the resolution of the measurement. With current technology, increasing the resolution of the measurement would render the PUF characterisation more difficult. The alternatives to increasing the entropy density for this category of PUF include increasing the dynamic range of emission intensity values, or the range of peak emission values.

2.1.3.2 Physical Unclonability and Unpredictability

The physical unclonability and unpredictability of a device is the fundamental property of a PUF. Their fabrication method is crucial: optical security devices, such as holograms, are designed to be very complex, but they require reproducibility. When holograms are printed, whilst complex, each one is identical. This 'symmetrical' fabrication process creates a tag that is both difficult to fabricate, and difficult to replicate. However, a PUF has an 'asymmetrical' construction which, instead of ensuring each device is identical, it ensures unique devices are created each time, with its own unique set of CRPs. This then makes it very easy to generate individual devices, but difficult to replicate: an unpredictable fabrication process, such as the methods discussed in this work, removes the requirement for devices to be identical.

There is a subtle difference from true, mathematical unclonability, which is restricted by the finite limit of possible CRPs, for a device of finite, reasonable size, and physical unclonability. It is impossible for the constellation-style O-PUFs detailed in this thesis to be mathematically unclonable, whilst satisfying other practical requirements. Physical unclonability is simply the requirement for the device to be hard to physically replicate.

2.1.3.3 One-Wayness

The concept of ‘one-wayness’, introduced by Pappu, is the asymmetry of complex system fabrication: there should be no straightforward way to clone, simulate, or reverse-engineer a process that can replicate a PUF[1,2]. Furthermore, if a nefarious party were to develop the process to fabricate reasonable forgeries of a device, such as a hologram, it would enable countless replication, due to the fact they are all identical. This weakness is avoided with PUFs: if the time was taken to replicate an individual optical PUF, it wouldn’t compromise the security of any other device. This asymmetry makes attacks on this classification of security device much less practical or attractive to counterfeiters.

2.1.3.4 Evaluability

The straightforward fabrication method of many PUFs extends to the simplicity of characterisation: a key FoM of PUFs, required for them to be used as tags for anti-counterfeiting, is that they should also be easily characterised and verified. This property is known as the evaluability of the device. Unlike holograms, which are identical, each PUF fabricated using the same methodology will be unique, therefore generating a unique set of responses to a given challenge. However, for it to be useful in many settings, the technique to measure the response should be straightforward. The PUF types used in this thesis are designed to be characterised, or have the potential to be able to be characterised, with macroscopic optical techniques, including macro-photoluminescence, or even with excitation and measurement with a smartphone’s optical system[4].

2.1.3.5 Other Practical Considerations

In addition to a PUF needing to be reasonably practical to characterise for it to be useful, an O-PUF which can be used in more settings is advantageous. For example, in the constellation-style O-PUFs, which are used in settings for anti-counterfeiting, such as where holograms are currently used, the ability to be deposited on different surfaces presents advantages. Additionally, O-PUFs constructed from non-toxic materials will be beneficial, for applications such as pharmaceutical security. Counterfeited drugs cost almost over 75 billion USD each year and naturally lead to an increase in deaths: it is estimated that over 700,000 deaths are caused annually from ‘sub-standard’ medicines, so verification of pharmaceutical authenticity is a very desirable point of research[5]. A food-safe O-PUF would enable the verification of the actual pharmaceuticals and reduce the opportunities for counterfeited drugs in real or counterfeited packaging.

Most O-PUFs of the type that are discussed in this work produce a unique pattern or response, which is characterised and recorded as part of the fabrication process. This response is binarised and stored in a database. An entry of the unique response set to a given challenge is recorded in the database is for each unique device, which is used to compare subsequent challenges of the same device for verification. This process is displayed in Figure 2-1.

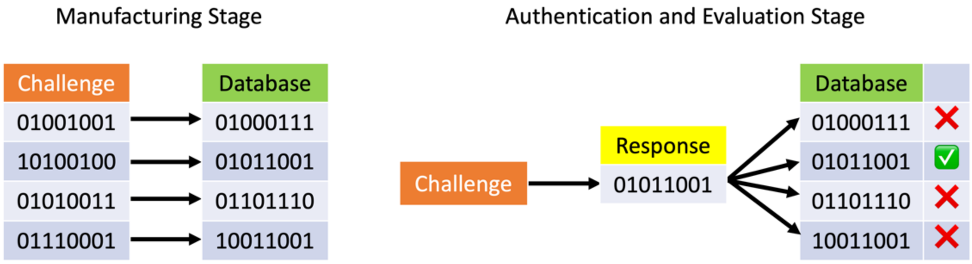

Figure 2-1: Demonstration of weak-PUF verification. During manufacture, each device is challenged and its response is stored in a database. When the device is interrogated later, its response is then compared back against the database.

2.1.4 Optical Physical Unclonable Functions

An optical physical unclonable function (O-PUF) is a classification of PUF which is evaluated and/or interrogated using light. All O-PUFs are known as having 'extrinsic' evaluation, which describes a PUF which must be evaluated by an external technique or instrument. (Conversely, PUFs which are 'intrinsic' are capable of self-evaluation, which are always electronic PUFs). In the case of the O-PUFs in this work, this is with a coherent or broad-band illumination source and CCD during photoluminescence.

Whilst most O-PUFs have explicit randomness, some do have an implicit source of unpredictability. One type of implicit O-PUF is the compact disc (CD) PUF. This PUF was designed for the authentication and identification of CDs. It measures the length of the lands and pits on the surface of the CD and compares this with their expected lengths: the manufacturing process of the CD creates slight random variations compared with the expected lengths[6]. These are compared with the pit and land lengths characterised of the CD during fabrication for authentication.

The paper PUF uses the implicit random arrangement of paper fibres as its unique fingerprint[7-9]. Designed to authenticate banknotes, or other physical paper documentation, a fingerprint is generated from a high-resolution image captured of a specific region on the page, where the implicit randomness arises from the unique and unpredictable arrangement of the fibres on each page during paper fabrication.

Many O-PUFs, including the ‘constellation-style’ O-PUFs described here are known as having ‘extrinsic’ evaluation, where they are not self-evaluating. The final step of the manufacturing process of an O-PUF is device characterisation, where the devices are interrogated with a known challenge, and their response is recorded and stored for authentication. When the challenge is presented again to the same PUF, its response is compared with the initial challenge for validation.

2.1.4.1 Constellation-Style Nanoparticle Optical Physical Unclonable Functions

Here, a ‘constellation-style’ O-PUF is defined as one that utilises the physical position of nanomaterials, such as optical nanoparticles, and the unique response that the position of these particles generates from an optical challenge.

The optical one-way function introduced by Pappu is an example of an explicit O-PUF. The scattering of light through a refractive nanoparticle-containing resin plate generates a unique response[1]. The pattern created is characterised and stored, to be measured and compared with the stored pattern under interrogation. Many nanoparticle constellation O-PUFs exploit the photoluminescence emission or the absorption or scattering of incident light [10-15].

The nanowire distribution PUF is a type of constellation-style PUF, which utilises the random position of silver nanowires (NWs) deposited on a PET film[16]. This film is then characterised using far-field optical microscopy to measure the position of the NWs. Similar nanomaterial constellation-style O-PUFs utilise the position of plasmonic nanoparticles on a surface, or embedded within a polymer, where the particle position or plasmonic resonance is used for the unique response. Like the nanowire distribution PUF, this distribution can be challenged with both far-field optical and higher resolution techniques, such as surface-enhanced Raman spectroscopy (SERS), to determine the unique signature created from the scattering of light from the NPs[17,18]. Similarly, an alternative nanoparticle-based PUF utilises phosphor particles blended and deposited into a surface as the foundation for an O-PUF[19]. Upon illumination with ultra-violet light, the unique distribution of the particles is revealed.

The manipulation of perovskite quantum dots and characterisation of fluorescent speckles which are produced under photoluminescence is a recent proposal for an optical PUF[20]. The argon ion beam etching of a poly-methyl methacrylate (PMMA) film creates ‘chaotic metasurfaces’, which enables random positioning of the fluorescent particles on the surface. Fabrication of these devices is illustrated in Figure 2-2. These samples had a very high bit density, with an encoding capacity (the number of potential bits a PUF can store), of over $2^{156,250}$ and demonstrated the potential for characterisation of the fluorescent particles with a phone or small portable optical setup.

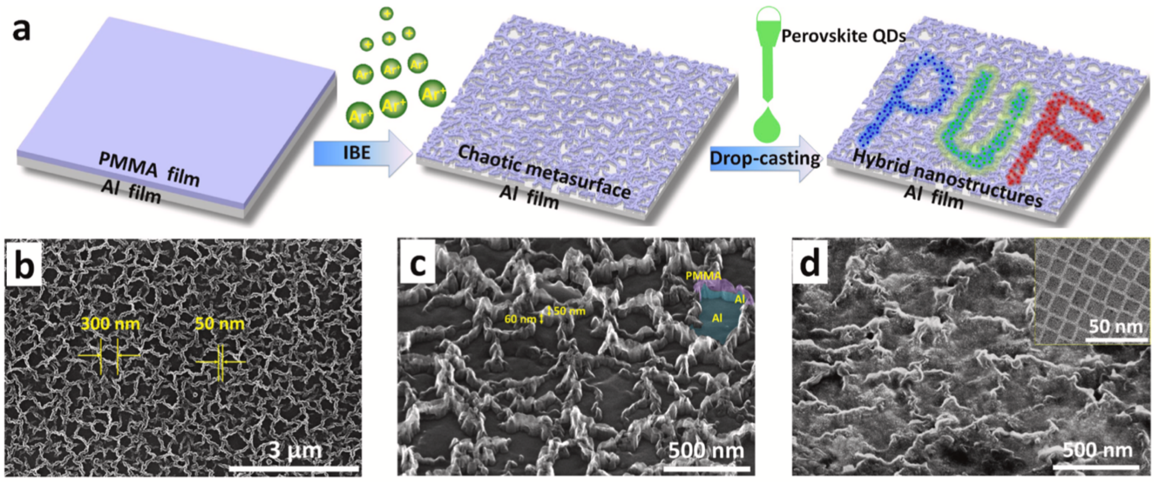

Figure 2-2 Fabrication of ‘chaotic metasurfaces’ using ion etching of PMMA for an OPUF. Reprinted from Chemical Engineering Journal, 411 (2021) 128350, F. Chen et al., with permission from Elsevier.

2.1.4.2 Two-Dimensional Material-Based Optical Physical Unclonable Functions

A variation of constellation-style O-PUFs utilises the optical properties of 2D materials, and the position-dependence of their optical response to a given challenge. This utilises their optical emission properties’ sensitivity to defects as the extrinsic source of randomness and unpredictability. A 2D O-PUF uses the optical properties of monolayers of chemical vapour deposition (CVD) grown WS_2 layers, which are highly sensitive to local structural and chemical defects in the monolayer[4]. Characterisation of the photoluminescence emission of the monolayers, and subsequent spatial mapping of the emission as a function of both peak intensity and frequency, generates a unique signature of that monolayer. Fabrication of 2D layers, even with relatively repeatable techniques, such as CVD, naturally introduces defects, including grain boundaries, cracks, vacancies, and substitution defects, which will locally modify the photoluminescence. These crystals are characterised using both micro-photoluminescence (μ-PL), and far-field macro-PL, utilising band pass filters to observe emission peaks.

An alternative 2D material-based O-PUF utilises the unpredictable nature of the CVD process in forming islands of materials and the layer-dependent band structure of transition metal dichalcogenides (TMDCs) (this is discussed further in Chapter 2.2.5.7)[21]. The CVD process to deposit islands of MoS_2 is initiated on an SiO_2 substrate. During CVD, under high temperatures, precursors (for MoS_2, S and MoO_3 powder) are injected into the chamber, where they can react, to form layers of material. The positions of growth of the islands on the surface are unpredictable, and growth is initiated randomly. Only the regions on the surface which are a single layer thick will emit brightly when illuminated by a laser, and areas that have no TMDC layers, or which have more than one layer, will not emit brightly, due to its indirect bandgap. Only the single layers are brightly emitting due to the direct band gap, which shifts to indirect when in a crystal of >1 layer. This arises from the confinement of charge carriers in a single plane. During initial interrogation, the substrate is divided into an array, and each cell is a region for an individual challenge. This produces a binary array, the binarisation of which arises from the layer-dependent emission properties of the CVD MoS_2. This process of challenging the array of CVD MoS_2 is displayed in Figure 2-3.

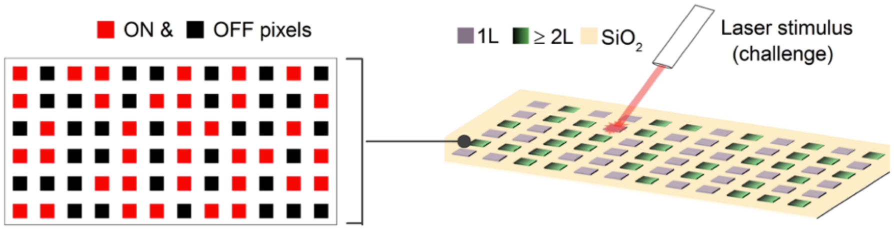

Figure 2-3: Islands on CVD-grown MoS_2 in a 2D array. Each pixel is individually optically challenged, and the random growth patterns form a unique response. Reprinted with permission from Abdullah Alharbi et al. Copyright 2017 American Chemical Society.

2.1.4.3 Advantages and Shortcomings of Existing O-PUFs

To be practical in a real device, not only do these devices need to have a high density of CRPs, but they should be easily fabricated, implemented, and characterised in the real world. It is relatively trivial to fabricate something incredibly complex with a high degree of confidence about its uniqueness, but without means of stable distribution and simple characterisation by an end-user it is much less useful. Some existing constellation-style PUFs have very high levels of complexity, making them much more difficult to replicate, but have characterisation and interrogation techniques that involve high-resolution measurements, often with expensive or impractical laboratory equipment, such as transmission electron microscopy (TEM), or SERS[22,23]. Naturally, as the entropy density of an O-PUF is increased, with increased complexity, the interrogation often will necessitate a higher resolution or more detailed technique. There is always a balance between the security of the tag and the feasibility of the characterisation method.

The development of constellation-style O-PUFs often focuses on the position or orientation of nanoparticles on a surface or within an object, often without much consideration for other optical properties, such as absolute emission intensity, or how they respond to multiple challenges. It is these avenues of development that this thesis strives to improve.

2.2 Semiconductor Background

In this thesis, it is demonstrated how optical semiconductor nanostructures, including how quantum dots (QDs) and 2D materials (2DMs), can be optically fingerprinted for security applications. To do this, here a brief background of semiconductor physics is introduced, including their optical properties, band structure, and how the quantum confinement of charge carriers in semiconductor nanostructures modifies these properties.

2.2.1 Semiconductor Band Structure

Semiconductors are a class of material, whose properties lie somewhere between an insulator and a conductor[24]. A bandgap is a region of forbidden states, within which any electronic state is disallowed between the valence band (VB) and conduction band (CB). Therefore, for a material to be able to conduct, charge carriers must be able to move from the VB into the CB.

In an insulator, the bandgap is large, so it requires a lot of energy to elevate charge carriers from the VB into the CB. For example, single-layer MoS_2 has a bandgap of 1.3eV, so a photon in the UV/visible/IR range is able to promote electrons to the conduction band. Whilst the line between a wide-gap semiconductor and an insulator is blurry, it is generally defined as one with a large enough band gap that, even at high temperatures (room temperature) there are a negligible number of thermally excited electrons in the conduction band. Conversely, in a conductor, the bands overlap, enabling their valence electrons to be free, so the material conducts electricity. Semiconductors have smaller band gaps, so only a small amount of energy is required to move the electron from the VB to CB, therefore their properties are very sensitive to their temperature[24]. This difference between insulator, semiconductor and conductor is illustrated in Figure 2-4. At T=0K, insulators do not conduct charge carriers, but as T increases, there is a non-zero probability that charge carriers will be thermally excited into the conduction band. From the Fermi distribution (discussed further in section 2.2.2), the number of charge carriers in the conduction band has the approximation which follows:

$$\mathrm{n}(T) \propto e^{\frac{-E_G}{2k_BT}}$$

(2-1)

where *n(T)* is the density of thermally excited charge carriers, E_G is the material band gap, k_B is the Boltzmann constant, and T is the system temperature. With a band gap of E_G = 1eV, this proportionality is around 10^{-9} at T=300k, but for an insulator with E_G=5.2eV, such as hexagonal boron nitride (hBN), this factor reduces down to around 10^{-44}, where conductivity is not observed. For the number of charge carriers in the CB for an insulator with E_G=5.2eV to be equivalent to that in a semiconductor with E_G = 1eV at T=300K, the system temperature would need to be around 1500K.

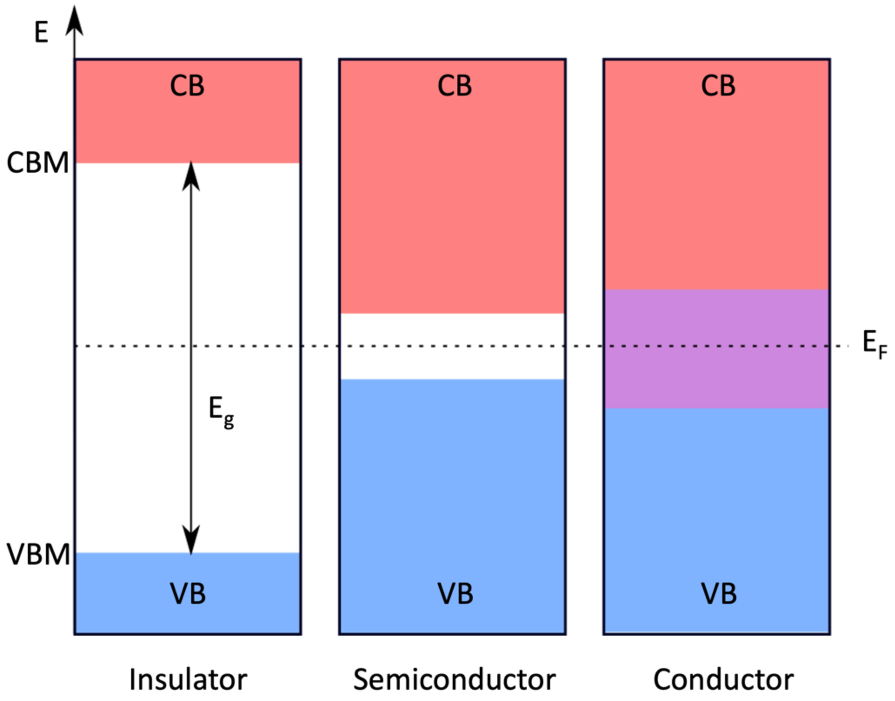

Figure 2-4: Band structure differences between (a) insulators, (b) semiconductors and (c) conductors, with the equilibrium Fermi level marked E_F. In an insulator, there is a large band gap between the valence band maximum (blue), and conduction band minimum (red). For a semiconductor, this gap is small enough for electrons to be thermally excited to the CB, for example, in silicon, E_g = 1.3eV. Hexagonal boron nitride is an insulator, due to a very wide bandgap of E_g = 5.2eV.

2.2.2 Fermi Distribution

The Fermi level is the highest energy level at which, at 0K, electrons are filled. It is the energy at which the available states in a system are half-filled. In conductors, the Fermi level is within the conduction band. We can describe the region of filled states within the valence band as the ‘Fermi sea’ of electrons.

At 0K, all semiconductors are insulators, but, due to their smaller bandgap, their properties are very sensitive to temperature, so electrons in the semiconductor VB can be excited thermally across the bandgap to the CB.

The Fermi distribution, also known as the ‘filling factor’, dictates the probabilities of certain states being occupied:

$$\mathrm{f(E)} = \frac{1}{\mathrm{e}^{(\mathrm{E}-\mathrm{E_f})/\mathrm{k_B T}} + 1} \tag{2-2}$$

where E is the electron energy, E_F is the Fermi energy, $k_B$is the Boltzmann constant, and T is the system temperature. From this, it follows that as the temperature of the system increases, a small fraction of charge carriers can populate the conduction band[25]. In the high-temperature limit $E - E_F \gg k_B T$, $f(E)$ tends towards the Boltzmann approximation of states $\mathrm{f(E)} \approx \mathrm{e}^{E-E_F/(k_B T)}$. Figure 2-5 shows the change in occupation probability as temperature increases, allowing states in the conduction band to become occupied from thermal excitation.

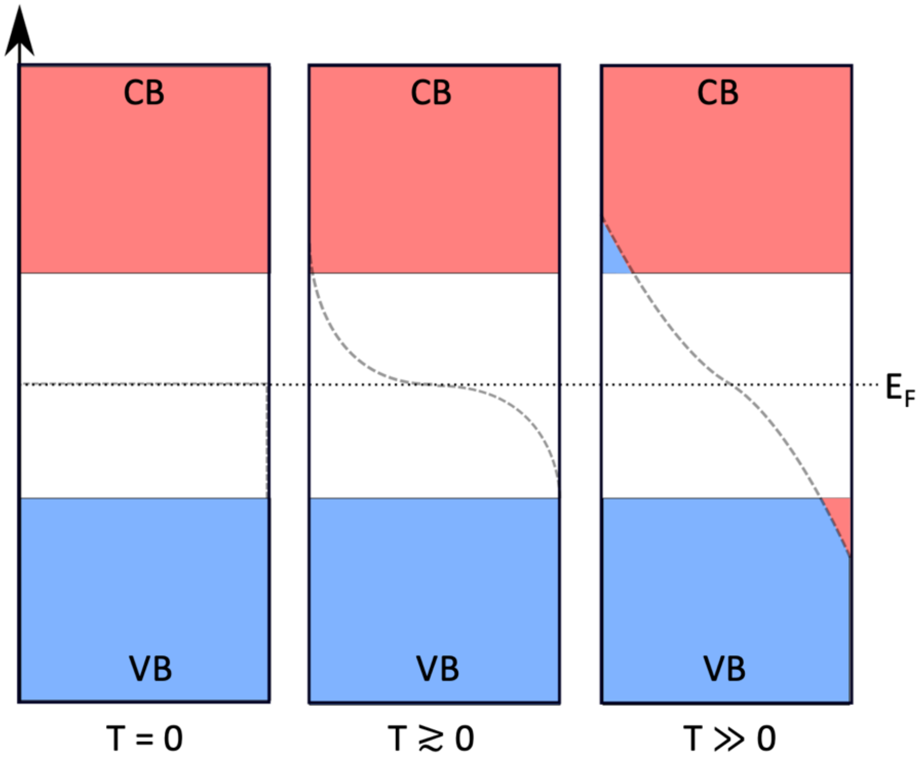

Figure 2-5: Demonstration of the change in Fermi function with increasing temperature. At $T = 0$, the highest level an electron can occupy is E_F. As the temperature increases, the distribution becomes 'smeared', enabling charges to occupy states within the CB. The blue regions indicate the allowed states, the red regions show the forbidden regions, and E_F shows the Fermi energy. When T>>0, the distribution smears enough such that states become allowed in the VB, allowing conduction of charge carriers.

The total population of charge carriers within a system is determined by the product of the Fermi distribution and the system's density of states:

$$\mathrm{N(E)dE = f(E)D(E)dE} \tag{2-3}$$

where $D(E)$ is the density of states.

2.2.3 Brillouin Zone

A lattice is a repeating, periodic array of points in space, each with translational symmetry, which can be described by a set of primitive vectors. Due to its periodicity, the whole lattice can be described by a single primitive cell, known as a Wigner-Seitz cell[26]. To describe the band structure of a material, we must consider the reciprocal lattice: the Fourier transformation of the Bravais lattice. This reciprocal lattice is the representation of the Bravais lattice in momentum space, which is described by a set of periodic wave vectors. In k-space, the building block of the reciprocal lattice is known as the first Brillouin zone and, like the Wigner-Seitz cell in physical space, this zone describes the band structure for the whole lattice.

2.2.4 Direct and Indirect Band Gap Semiconductors

The band gap of a material is the difference between the maximum energy of the valence band (VBM), and the minimum of the conduction band (CBM), in which no electronic states are permitted. If these occur at the same value in k-space, this is known as a direct band gap semiconductor. An indirect band gap semiconductor has the VBM and CBM at different positions in k-space, requiring additional momentum in the form of a phonon to excite a charge carrier between them. Direct band gap semiconductors are therefore much more efficient optical materials: for an electron to be raised up to the conduction band, it requires a photon with an energy $E_\gamma \geq E_g$. However, in an indirect gap material, a photon does not have the momentum to provide the shift required in k-space to move an electron into the CB. This difference in momentum is obtained by the electron through the interaction with a phonon: a quasiparticle that propagates vibrations through the crystal lattice. For an electron to successfully move into the CB, it must interact with both a photon of the correct wavelength and a phonon with the correct wavevector. Whilst phonons are common in lattices where $T \gg 0K$, this remains a suppressed mechanism because it is a 3-body process, so the probability of a transition is significantly reduced, compared with a direct transition. This creates much longer radiative lifetimes for indirect transitions, so most electron-hole recombination instead occur non-radiatively, through defects or grain boundaries. For these reasons, direct gap semiconductors, such as GaAs, single-layer TMDCs, and InP CQDs are preferred as optical emitters over indirect gap materials, such as silicon. This difference between types of semiconductor bandgap is illustrated in Figure 2-6.

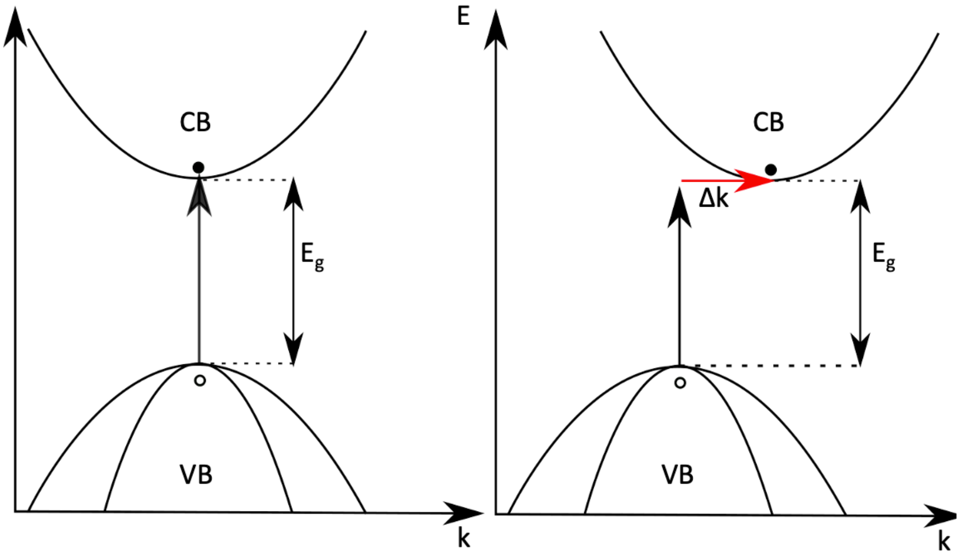

Figure 2-6: Band structure differences between (a) direct band gap materials and (b) indirect band gap materials. A phonon (red arrow) is required for the momentum shift Δk, with momentum equal to the difference between the electron and hole momentum.

2.2.5 Quantum Confinement

Nanostructures which are small enough that the charge carriers are confined in one or more dimensions are referred to as 'low-dimensional', depending on the number of dimensions they are confined within. As the scale of the material approaches the wavelength of the charge carrier, the available energy states of the charge carriers do not remain continuous and become discrete allowed energy levels. In quantum dots, the confinement is in all dimensions, so they are referred to as '0-Dimensional'. Likewise, monolayers of van der Waals crystals are described as '2D' semiconductors due to the charge-carrier confinement in one direction. This confinement allows for bandgap-tuning of the materials by adjusting their size: a smaller quantum dot will blueshift the emission properties. Likewise, the bandgap and optical properties of van der Waals crystals can be strongly dependent on the number of layers in the sample.

2.2.5.1 Top-down vs. Bottom-up Fabrication

Low-dimensional semiconductors, with their desirable properties from electron confinement, can be fabricated in two key classes of fabrication: top-down and bottom-up. Concisely put, top-down fabrication involves the reduction of larger, bulk materials to small and confined structures, such as reactive ion etching (RIE) and lift-off lithography. Bottom-up, or self-assembly, fabrication is the fabrication of quantum-confined nanostructures from precursors which are grown, such as chemical vapour deposition (CVD) or atomic layer deposition (ALD).

In Chapter 4, the colloidal quantum dots, which are fabricated in a bottom-up approach, are deposited as an array on a surface.

Later, in Chapter 5, a quantum O-PUF is developed with micro-mechanically exfoliated WS_2. Micromechanical exfoliation of van der Waals (vdW) crystals is one of the most common methods of top-down fabrication, using the 'Scotch-tape' technique, where 2D vdW crystals are mechanically separated using adhesive tape. This technique is described in detail in Chapter 3.1. Alternative top-down approaches can include liquid-phase exfoliation, where the individual layers of a crystal or powder of a vdW crystal are separated through sonication or shear-force treatment, alongside the interaction with a solvent. 2D materials can be fabricated using bottom-up techniques, such as with chemical vapour deposition (CVD), where precursors are injected into a furnace, where they react on a surface to form islands and subsequently large areas of 2D materials.

2.2.5.2 Excitons

Once an electron has been excited to the conduction band, it leaves behind a 'hole' in the valence band. Instead of an absence of an electron, a hole can be considered a particle with positive charge and its own effective mass m_h. As the electrons in the Fermi sea move into the vacancy created, it can be thought of as a particle moving though the VB. The coulomb attraction between the electron and hole leads to the creation of a quasi-particle, known as a Wannier-Mott exciton, which can freely move through the material without being bound to a specific site within the lattice, or transferring net charge. The formation of an exciton in a confined semiconductor is shown in Figure 2-7.

To determine the binding energy of the exciton, we can model the exciton as a hydrogen-like system, albeit with a much lower binding energy. With this description, we can model their separation with the Bohr radius:

$$a_0 = \frac{4\pi\epsilon_0\hbar^2}{\mu e^2} \tag{2-4}$$

where ϵ_0 is the material's dielectric constant, μ is the exciton's effective mass, and e is the electric charge. In the Bohr model of a Hydrogen atom, the energy of the n^{th} state is defined as:

$$E_n = -\frac{R_E}{n^2}$$

(2-5)

where R_E is the Rydberg energy, which we can modify to determine the binding energy of the exciton:

$$\mathrm{R_E} = \mathrm{BE_x} = \frac{\mu e^4}{2(4\pi\epsilon_0\hbar)^2}$$

(2-6)

where μ is the reduced mass of the exciton.

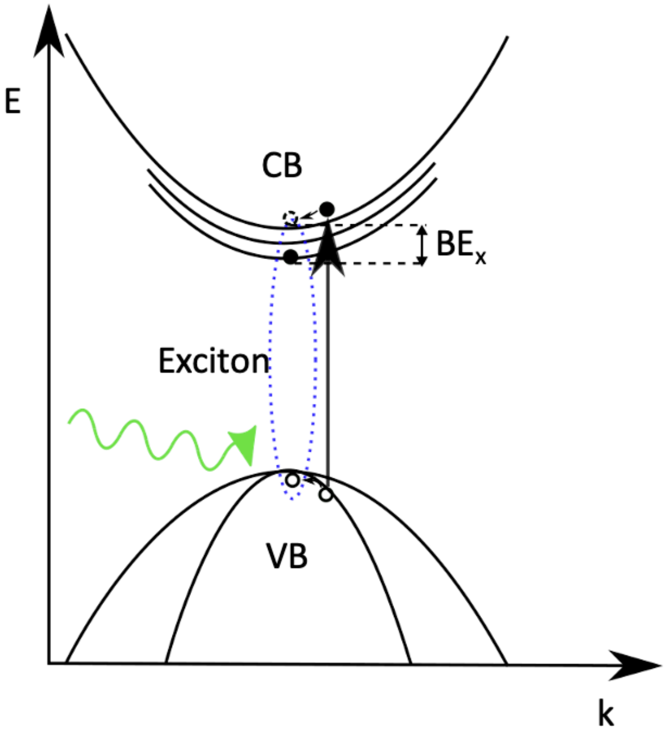

Figure 2-7: Band diagram of a direct band gap semiconductor creating an exciton (blue), with binding energy BE_X.

2.2.5.3 Radiative and Non-Radiative Recombination

For the recombination of excitons in semiconductors, there are radiative and non-radiative mechanisms, and the dominance of a specific mechanism dictates the internal quantum efficiency of the material.

During radiative recombination, the energy of the exciton is emitted as a photon, from either a band-to-band, donor-band, or donor-acceptor transition. However, defects such as grain boundaries in the lattice, vacancies, or substitutions create new pathways for the exciton to recombine. The primary non-radiative recombination methods are Shockley-Read-Hall (SRH) and Auger recombination. SRH recombination exploits additional energy levels which trap charge carriers, inducing a two-step recombination process. The electron becomes trapped in an energy level which is within the bandgap, where the electron in the trap then falls into an empty state in the VB, so no photon is emitted, and the energy is dissipated by phonons. Finally, Auger recombination is also a band-to-band transition, but instead of the emission of a photon, the energy excites another electron or hole to a higher energy band, which then thermalises through multiple phonons. Both of these processes reduce the total quantum efficiency of the system.

The quantum efficiency of the material can be expressed as:

$$\eta_q = \frac{\frac{1}{\tau_{rad}}}{\frac{1}{\tau_{rad}} + \frac{1}{\tau_{non-rad}}}$$

(2-7)

where τ is the recombination lifetime. In direct-gap materials, the non-radiative lifetime is much longer than the radiative lifetime, due to the strongly phonon-mediated mechanisms, suppressing the non-radiative channels. However, in an indirect bandgap material, the radiative and non-radiative lifetimes are comparable, so they have a much lower QE. For example, in 1L MoS_2, $\tau_{rad} = 0.85\text{ns}$ at room temperature, but this lengthens to $\tau_{rad} = 2.6\text{ns}$ for bulk MoS_2[27]. This difference in lifetime explains the significant increase in quantum efficiency from bulk MoS_2 to a single layer: an effect which is observed in many 2D TMDCs.

2.2.5.4 Fermi's Golden Rule

The mechanism through which light couples with electric transitions in semiconductors for the generation of excitons can be described by Fermi's Golden Rule (FGR):

$$\lambda_{i-f} = \frac{2\pi}{\hbar} |\mathrm{M_{if}}|^2 \mathrm{g(E)}$$

(2-8)

where M_{if} is the matrix element for the transition, and *g(E)* is the density of final states. The transition matrix element for an interaction is obtained from the Hamiltonian for the interaction and provides the probability of an interaction taking place. FGR describes the probability of a given transition taking place, where $\lambda_{i-f} = 1/\tau$ is the transition probability, and τ is the exciton's radiative lifetime.

Due to the coulomb attraction within the exciton, there is a strong overlap of the electron and hole wavefunctions, increasing the transition probability. It is clear from equation (2-8) that an interaction is more likely if the matrix element M_{if} is greater. The matrix element contains all of the particle physics of the interaction, and its magnitude is dictated by the wavefunction overlap of the electron and hole. The charge carrier's wavefunction expresses the probability of finding that particle at a specific point in space. Therefore, a greater wavefunction overlap indicates a higher probability they will interact.

2.2.5.5 Quantum Confined Density of States

Nanostructures on the same scales as excitons create boundary conditions on the electron-hole wavefunctions. In bulk crystals, the allowed energy bands form a continuous distribution of states but confining the physical size of the semiconductor creates a rigid boundary condition on the wave functions of the electron and hole. We can therefore use the 'particle in a box' model: the energy levels of confined particles in low-dimensional materials can be evaluated using the time-independent Schrödinger equation:

$$\frac{-\hbar^2}{2\mathrm{m}}\nabla^2\psi = \mathrm{E}\psi \tag{2-9}$$

Using the boundary conditions at the edge of the box $\psi(0) = \psi(L) = 0$, the solution can be expressed as:

$$\mathrm{E} = \frac{\hbar^2}{2\mu}\left(\frac{\pi}{L}\right)^2 \tag{2-10}$$

where μ is the exciton's effective mass, and L is the confinement scale of the semiconductor.

Therefore, at the scale of the de Broglie wavelength, energy levels in a system are no longer continuous. This boundary requirement results in the quantisation of allowed energy levels. In quantum dots, this restriction is in all dimensions, equivalent to electron orbitals in atoms, reducing the density of states to a set of delta functions. In reality, these functions are broadened slightly, due to the size distributions of QDs.

When confined to a plane, such as in a 2D material, we obtain a quantum well, and confinement in two dimensions yields a quantum wire (a '1D system'). In a 2D material, the density of states per unit energy per unit area is constant, independent of energy, leading to a set of steps in the DoS, each level contributing $\mathrm{m_X}/\pi\hbar^2$. The density of states for materials with confinement in different numbers of dimensions is shown in Figure 2-8.

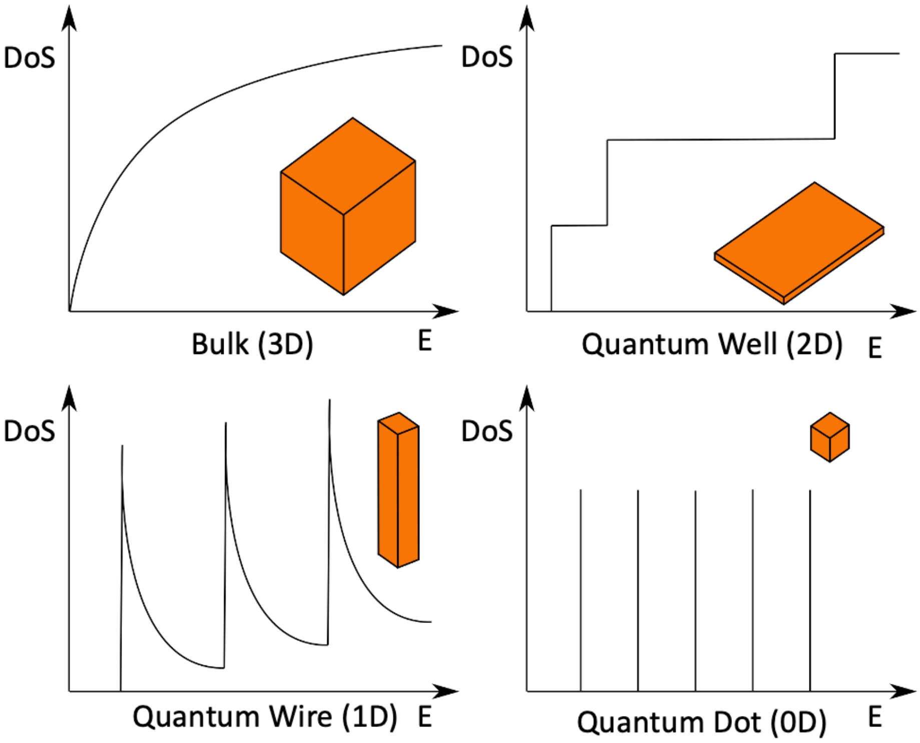

Figure 2-8: Density of states for different levels of quantum confinement. In a bulk crystal, there is a continuous distribution of states available, which become more confined, as the dimensions of the material are reduced to the order of the wavelength of the charge carriers.

2.2.5.6 Quantum Dots

A quantum dot (QD) is a semiconductor nanostructure whose size is such that the electrons are confined in all three dimensions Because of this, they are referred to as 'artificial atoms', due to their similarity of discrete electronic states to the electron states in an atom. Core-shell QDs are a radial semiconductor heterojunction, consisting of an island (core) of one semiconductor (InP for the O-PUFs described in this work), surrounded by a 'shell' semiconductor with a different bandgap (ZnS in this work). They are desirable as optical emitters due to the high degree of tunability of emission wavelength: their emission frequency is strongly dependent on their size due to the quantum confinement. In semiconductor heterojunctions, the band alignment of the two materials determines the confinement potential[28]. The band gap difference between InP and ZnS ensures there is a very high confinement potential between the two semiconductors, so the excitons are confined to the InP core, increasing their quantum yield[29,30]. The band structure for an InP/ZnS core-shell QD is shown in Figure 2-9.

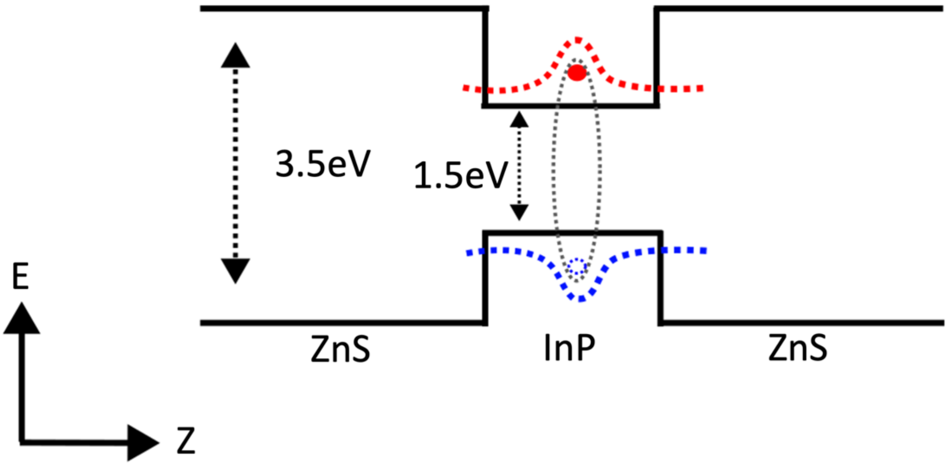

Figure 2-9 Band structure of InP/ZnS QDs. Grey dotted line indicates the exciton. Red shows the exciton and its wavefunction, blue dotted line indicates the hole and its wavefunction.

Colloidal quantum dots (CQDs) are QDs that are fabricated in suspension. The methods of fabrication of QDs are out of the scope of this work, but commonly include the 'hot-injection' method, which typically have a range of sizes from 2-50nm containing from a few hundred to thousands of atoms[31]. For more details on the fabrication techniques of colloidal QDs, see Sinatra et al. for a comprehensive guide[32].

CQDs have several advantageous properties for O-PUFs. Firstly, due to their colloidal nature, fabrication and scalability is very flexible, but their small size means their optical properties are very sensitive to fabrication conditions, enabling the ability to carefully tune the energy levels of the dots. From the particle in a box approximation, as the size of the dot decreases, the allowed energy level spacing widens. From equation (*2-10*), the change in emission wavelength as a function of core diameter follows:

$$\mathrm{E} = \mathrm{E_G} + \frac{\hbar^2\pi^2}{8\mu r^2} \tag{2-11}$$

where E_G is the semiconductor band gap, μ is the reduced mass, and r is the QD core radius. The QDs in this work were InP/ZnS core/shell QDs, with a peak emission wavelength of λ=620nm, with an InP core r=1.95nm. Therefore, if r=2.45nm, the emission wavelength would shift to λ=701nm. This property gives very high tunability to their emission properties. An increase in the core thickness by a single atom will change the peak emission energy by several E_V. This sensitivity to emission properties in core thickness makes them desirable optical nanoparticles for O-PUFs.

2.2.5.7 Two Dimensional Materials

A van der Waals (vdW) two-dimensional material is material from a crystal whose bonds are very strong in one plane, held together with weak vdW forces between planes, for example sheets of graphene stacked in a crystal of graphite; hexagonal boron nitride (hBN); phosphorene; and transition metal dichalcogenides (TMDCs)[33-36]. Due to their weak inter-layer bonds, it is straightforward to reduce the crystals from a bulk material down to few and single-layer samples, essentially creating a quantum well to confine the charge carriers within the plane, creating the ability to tune the material properties.

TMDCs are particularly interesting for their optical properties because, unlike graphene, which is a semi-metal with no bandgap, TMDCs have bandgaps that are often sensitive to layer thicknesses. They have the formula MX_2, where M is a transition metal, usually tungsten (W) or molybdenum (Mo), which is sandwiched between two layers of chalcogen atoms (X), such as sulphur (S) or selenium (Se). Monolayer TMDCs generally have a direct bandgap in the optical-NIR range, making them very attractive for optoelectronic applications.

MoS_2, WS_2 and other TMDCs have unique band structures, which creates interesting optical properties: when in a few-layer to bulk form, it has an indirect band gap, making it a poor choice of optical material, due to the inefficient recombination. However, when reduced to a monolayer, it becomes a direct gap semiconductor. There is a significant change to the valence band at the edge of the Brillouin zone, shifting the gap from indirect; in MoS_2 the point of charge carrier transition is near the Γ point, to a direct band gap at the k point[35]. This evolution from indirect in bulk, to direct in monolayer bandgap semiconductor also occurs in WS_2 and is illustrated by its band diagram, shown in Figure 2-10. In addition to having a band gap that is layer-dependent, the optical emission properties of TMDCs are highly sensitive to other external factors, such as local strain and doping[37]. These are properties that have been used to tune the local emission properties of 2D materials. Uniaxial and biaxial strain applied to layers of 2D materials can modify the band gap, or even induce a direct-indirect band gap transition. For example, under uniaxial strain, the A excitonic peak of MoS_2 redshifts[38-40]. Doping is a common, sometimes uncontrollable or unintentional, modification to an optical 2D TMDC, which can have significant consequences for the excitonic behaviour. It can arise from the adsorption of molecules in ambient conditions, from the substrate, or can arise during the fabrication process. Adsorption of molecules onto the surface can modify the exciton binding energies in the material – this effect has been exploited to make effective gas sensors from 2D TMDCs[41]. Localised defects, especially point defects, such as sulphur vacancies (S_V) significantly affect the efficiency and exciton binding energy, and reducing the external quantum efficiency (EQE) of the 2D material[42,43].

All of these local effects on the exciton binding energy, whilst often disadvantageous for improving the overall optical properties of 2D TMDCs, all add to an increased dynamic range of emission, including both emission intensity range, peak emission wavelength, and photoluminescence line shape. All of these variations, some of which are intentionally induced, and others which arise naturally, contribute to the spatial variation in emission properties required for an effective O-PUF.

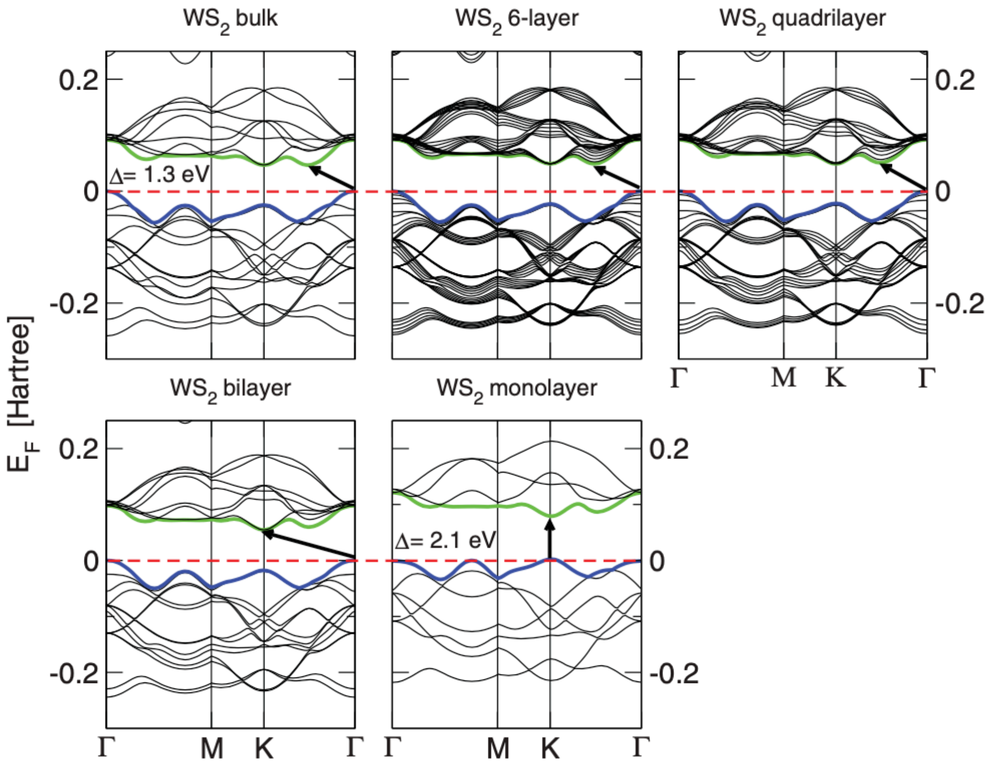

Figure 2-10: Shows the evolution of the bandgap of WS_2 as layer thickness reduces. Once a monolayer is reached, the bandgap becomes direct at the K point. Only when it is a monolayer, the CBM (green) and VBM (blue) are at the same point in K space, at which the bandgap becomes direct. Reprinted figure with permission from A. Kuc, N. Zibouche, and T. Heine, Physical Review B, 83, 245213, 2011. Copyright (2021) by the American Physical Society.

2.3 Plasmonic Enhancement

There has been an interest in the use of metallic nanoparticles and their interactions with light since the mid 1800s[44]. Historically used to modify the colour of stained glass, more recently the use of localised plasmonic resonances is a key technique in enhancing the photoluminescence of optical quantum emitters, such as fluorescing molecules, quantum dots, and 2D materials. A localised surface plasmon is a non-propagating excitation, which arises from the oscillations of the electrons in metal nanostructures[45]. When in an electromagnetic field, the electrons in the metallic nanoparticle are displaced by the incident electromagnetic wave, where then a restorative force from the Coulomb interaction between the electron and the atomic nuclei in the nanoparticle creates a resonant oscillation known as a localised surface plasmon (LSP).

In silver and gold nanoparticles, the resonant frequency of the LSP is in the visible range of the electromagnetic spectrum, making them commonly used for many optical applications, including biomedical imaging. There are two mechanisms through which metallic nanoparticles can help enhance the local PL emission, which is dependent on either the excitation or emission frequency of the sample[46].

Firstly, there is ‘absorption enhancement’. This mechanism is the simpler mechanism, by which the nanoparticles can enhance the local electric field if the absorption peak of the NPs overlaps with the wavelength of the pump laser. This effectively increases the incident light intensity locally at the point of the NP, so the rate of exciton generation increases[47].

The second mechanism, which is predominantly investigated in this thesis, is ‘emission enhancement’. This involves the careful selection of the size of NP, where its surface plasmonic resonance (SPR) is selected such that the absorption peak matches closely the bandgap of the optical material, as opposed to the illumination source, so the emission will couple with the plasmonic nanoparticle. This has the potential to significantly increase the spontaneous emission of a quantum emitter, which can be described by the Purcell effect[48]. Instead of locally increasing the incident radiation, the plasmonic nanoparticles spontaneously enhance the emission: a reciprocal mechanism to optical absorption. In this work, it is this mechanism that causes the spontaneous emission of the plasmon to increase the total emission from the samples. The key mechanisms through which plasmons can interact with fluorescing materials are demonstrated in Figure 2-11. Spontaneous emission enhancement is displayed as mechanism 5 in Figure 2-11, where the emitter can excite plasmons in the metal NP, generating a second radiative decay channel.

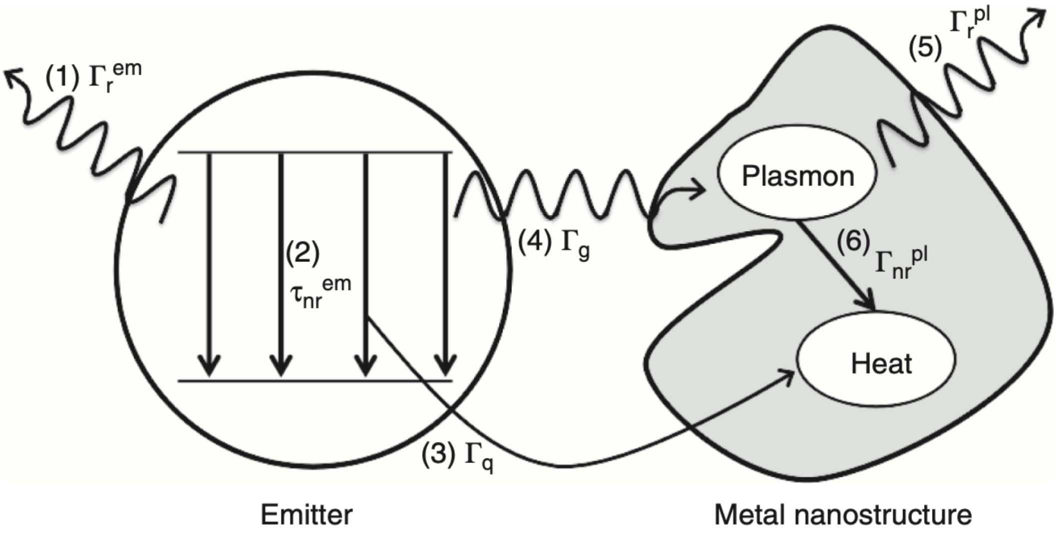

Figure 2-11: Different recombination mechanisms involved in metal NP-mediated fluorescence enhancement. 1) Radiative decay from emitter 2) Nonradiative decay from emitter 3) Direct quenching of the fluorescence through the metal nanostructure 4) Excitation of plasmons in the metal nanostructure from decay in the emitter 5) Radiative decay of plasmons 6) Non-radiative decay of plasmons. Used with permission from Wiley[46].

The Purcell effect is the enhanced spontaneous emission of a quantum system through changes in the environment of the material, such as the presence of local plasmonic nanoparticles. The strongly localised electron excitations at the surface of the metal NPs strongly enhances the local electric field near the quantum emitters, increasing the emission efficiency of the system[49]. A local plasmon resonance which matches the emission wavelength of the material will enhance the radiative decay rate, and therefore increase the quantum efficiency of the system. This is the mechanism that is used throughout this thesis because it does not require the matching of the SPR of the AuNP with the excitation source, so the characterisation method is not dependent on sample composition. This allows the characterisation of the samples with different excitation wavelengths.

If a fluorescing material is in direct contact with a metallic surface, this creates an efficient, non-radiative recombination channel (illustrated as mechanism 6 in Figure 2-11), so a very narrow spacer of dielectric should separate the emitter from the plasmonic nanoparticles, to prevent charge-carrier transfer. The strength of the coupling between the two is very sensitive to the dielectric thickness. Figure 2-12 shows the strength of coupling as a function of spacing for gold nanoparticles with fluorescent molecules[50]. If the fluorescing material (in the work by Anger et al. fluorescing molecules are modelled) is too close to the metal structure, the fluorescence will quench through the metallic structures, so the enhancement rate ($I_{enhanced}/I_0$, where I_0 is the emission without plasmonic structures) tends towards 0. If the spacing is too great, the effect of the plasmonic structures reduces, so the enhancement rate tends to unity.

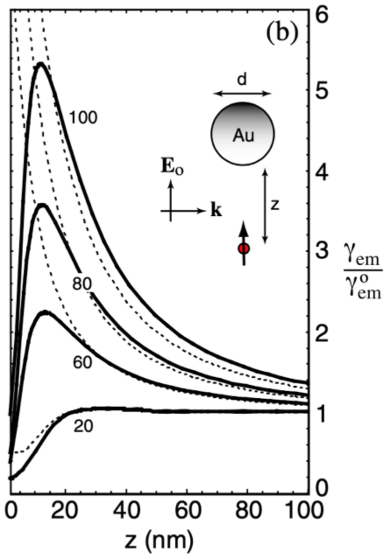

Figure 2-12: Calculated data for peak emission enhancement, as a function of distance from fluorescing molecule to a plasmonic nanoparticle. As the spacing decreases, quenching of emission occurs. As the spacing is increased, the enhancement factor tends towards 1, as the coupling strength between the fluorescence material and the plasmons reduces. There is an enhancement peak where these factors balance. Reprinted figure with permission from Anger et. al, PRL, 96, 113002, 2006. Copyright 2022 by the American Physical Society.

Chapter 3

Experimental Methods

This chapter aims to discuss the experimental methods used to fabricate, validate, and interrogate the optical physical unclonable functions (O-PUFs) using low-dimensional nanomaterials. Firstly, device fabrication is discussed with the techniques required to manufacture the O-PUFs. Next, device characterisation techniques are introduced. These methods are for both sample verification and interrogation, to characterise the properties of each device, and to generate their unique response.

Initially, the fabrication of 2D semiconductor crystals from bulk crystals is detailed, and subsequent manipulation and device manufacture methods are discussed. Deposition methods for colloidal quantum dots (CQDs) and plasmonic gold nanoparticles (AuNPs) are introduced. Subsequently, methods to verify and characterise the samples, including nanoparticle distribution and candidate monolayers are detailed, including optical contrast with optical microscopy, Raman spectroscopy, and atomic force microscopy (AFM). Optical methods to test and verify the tags using photoluminescence are then discussed. Finally, techniques to optimise the quality of the layer and the quality of the interface between the 2DM and substrate are introduced to remove bubbles and contamination from the surface, which could improve their optical and physical properties.

3.1 Fabrication Methods

This section introduces the techniques used to fabricate the O-PUF devices including the deposition of colloidal quantum dots and metallic nanoparticles, and exfoliation and manipulation of 2D materials.

3.1.1 2D Micromechanical Exfoliation

To fabricate the devices with optical 2D materials discussed later in this thesis, individual single-layer crystals of TMDCs were exfoliated from a bulk van der Waals crystal, utilising the weak inter-layer, but strong intra-layer bonds of the materials. First exploited to obtain single layers of graphene using scotch tape from a crystal of graphite, this technique provides a trivial method of exfoliation and manipulation of 2D crystals. This method was used with low-adhesion Nitto tape, chosen to leave as little organic residue on the crystal as possible. The bulk crystals were pressed onto the tape, and repeatedly peeled against another piece of tape, before being pressed onto the required substrate, such as Si/SiO_2, highly orientated pyrolytic graphite (HOPG), or to a polydimethylsiloxane (PDMS) polymer substrate. As the tape is removed from the substrate, it leaves behind crystals of different thicknesses, some of which will be one layer thick. Single layers can then be identified and verified using a variety of characterisation techniques. This method was very effective at producing monolayers up to 50µm in size.

3.1.2 PDMS Transfer of 2D Materials to Substrates

There are two options for subsequently fabricating devices once the bulk crystals have been exfoliated. Firstly, the Nitto tape is pressed directly onto a clean piece of Si/SiO_2 and carefully removed. Once exfoliated, this '2D tape' was pressed onto a glass slide with a small piece of Gel-Film on the surface. Gel-Film is a commercially available sheet of poly-dimethylsiloxane (PDMS), which has physical properties that are advantageous for the identification and manipulation of 2D flakes. At room temperatures, it will retain 2D crystals, but when it is slowly stretched and/or heated, its adhesion reduces significantly. This allows for both exfoliation and pick-up of flakes, and subsequent transfer of flakes to other substrates, including stacking of flakes to make vertical heterostructures with minimised residue and damage to the crystals.

A substrate was affixed to a small Peltier thermoelectric module on a rotating base. These units are desirable as a heating element in the transfer station due to its stable temperatures, which are controllable from a DC power supply. The glass slide with PDMS stamp was affixed to a 5-axis micrometre stage above it, allowing for precise control over its position and angle relative to the substrate. The stamp and substrate can then be manipulated relative to one another with the 5-axis stamp manipulator, and substrate rotation stage so they are aligned in the desired site in position and angle. Once they are positioned correctly, the micrometre stage allows for precise, controlled movement of the stamp towards the substrate. They are carefully brought into contact, so the flake is fully in contact with the substrate. Care must be taken to align the stamp correctly, so an excessive force is not applied to the flake, which could cause structural damage to the sample. A schematic of the 2D PDMS transfer system is shown in Figure 3-1.

The system is left in place for several minutes, and then the stamp is slowly removed. For a successful transfer, the strength of the van der Waals bond between the substrate and 2D layer must be stronger than between the monolayer and the PDMS stamp. PDMS is a non-Newtonian fluid, so becomes more viscous if a higher force is applied to it, and conversely less viscous if a very small force is applied. To aid with a successful transfer of 2D materials, when removing the stamp from the substrate, it is heated to around 60°C which reduces the adhesion of the flake to the PDMS and promotes transfer of the material.

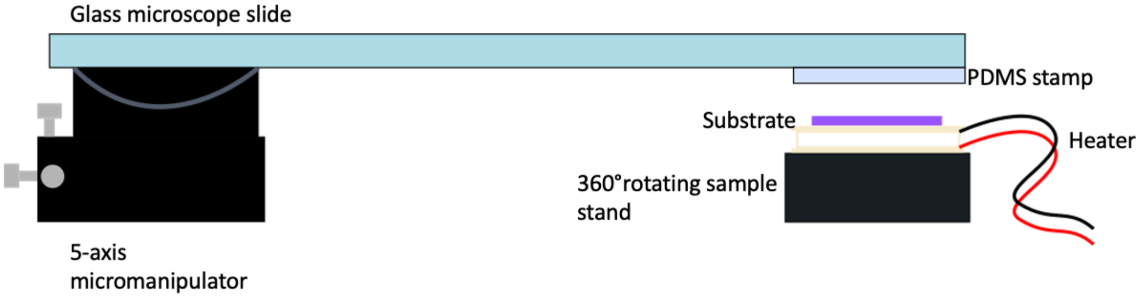

Figure 3-1 Schematic of the deterministic dry transfer station. The 2D flake is identified on the PDMS stamp under an optical microscope, before manipulation and transfer with the micro-manipulator.

3.1.3 Nanoparticle Deposition

Both gold nanoparticles (AuNPs) and colloidal quantum dots (CQDs) are used extensively throughout this work. This section details the key methods used to deposit these NPs with the required distribution onto the sample substrates. AuNPs are used to modify and enhance the optical response from the nanomaterials. To achieve this, a discrete, uniform distribution was required, such that large clusters of AuNPs did not accumulate on the surface, which would encourage quenching of the photoluminescence (PL) from the optical nanomaterials. The size of the AuNPs was chosen to carefully match their local plasmonic resonance peak, with either the excitation wavelength of the laser or the emission wavelength of the emitting material.

Commercially available colloidal AuNPs in phosphate-buffered saline (PBS) were centrifuged so they could be removed from their buffer solution. After centrifugation, the AuNPs form a pellet at the bottom of the Eppendorf tube, so the buffer can be carefully removed, leaving the NPs. These were then redispersed in a carefully optimised volume of ethanol, such that the density of NPs on the surface had the required density for the optical device. Changing the volume of ethanol added to the same mass of AuNPs naturally changes the density of the colloid, so this enables control of NP surface density during deposition.

To deposit the different nanoparticles on the sample surface, two methods were employed: the first is electrospray ionisation of the nanoparticle solution. This process is detailed further in Chapter 4.3, but CQDs are dispersed in a polar solvent (e.g., ethanol, toluene) and put in a syringe with a 30 gauge needle. A high potential difference is then applied between the needle tip and the substrate. A high electrostatic force then forces the solution out of the needle, separating the droplets. The electrostatic force causes the droplets of polarised solvent to repel, splitting into increasingly fine droplets, forming a cone of polarised solvent droplets at the end of the needle, known as a 'Taylor cone'. This process of generating microscopic droplets minimises the volume of solvent reaching the substrate, through evaporation. This technique enables the coverage of a large area or several samples simultaneously. It also generates a much more uniform distribution of NPs on a surface.

The second method used is drop-casting. Drop-casting is a fast and straightforward method of solution deposition, where a single drop (10µl) of NP solution is deposited on a substrate with a pipette and allowed to dry under ambient conditions. This technique is much faster, and in the case of colloidal AuNP deposition, does not require the redistribution of NPs into a different solvent. However, it is not an effective method of distribution over large areas, because it leads to very nonuniform regions, with clustering observed as the solvent dries across the sample in 'coffee-rings', where there are dense regions, alongside sites with no NPs at all. However, for the applications of fabricating O-PUFs described in this work, this inhomogeneity is not necessarily a shortcoming, due to the requirement for their random spatial positioning.

3.2 Sample Identification Techniques

Once the O-PUFs have been fabricated, several techniques are used to verify that their properties match the sample design. Whilst the distribution of CQDs is reasonably uniform across the surface, the density and distribution of QDs and AuNPs are characterised to interpret how their interactions determine their optical properties. For the van der Waals (vdW) crystals, it is important to be able to accurately identify the number of layers of a vdW crystal sample, in particular single layers, because the properties of the material vary significantly as the thickness increases. Two main techniques are used to verify these: optical contrast using bright-field optical microscopy and atomic force microscopy (AFM).

3.2.1 Identification of 2D Materials with Optical Contrast

The first step in the identification of single-layer materials is the use of conventional optical microscopy. The optical contrast of the reflected light from the sample to that of the background is very sensitive to layer thickness. For any given layered material on any substrate, the optical contrast is defined as:

$$\mathrm{C} = \frac{I_{BG} - I_{film}}{I_{BG}} \tag{3-1}$$

where I_{BG} is the reflected intensity from the background substrate and I_{film} is the intensity of the reflected light from the 2D film. Each layer gives an equal contribution to the contrast, so the number of layers can be well-identified. The degree of the contrast depends strongly on the refractive index of the crystal and of the substrate: an Si/SiO$_2$ substrate with 90 or 300nm of oxide will provide the most optical contrast to the human eye, but most TMDCs on PDMS will provide sufficient contrast for crystal identification after exfoliation. A flake with several steps in the crystal of MoS$_2$ is shown in Figure 3-2. This technique of deposition often leads to the trapping of organic compounds underneath the surface[51].

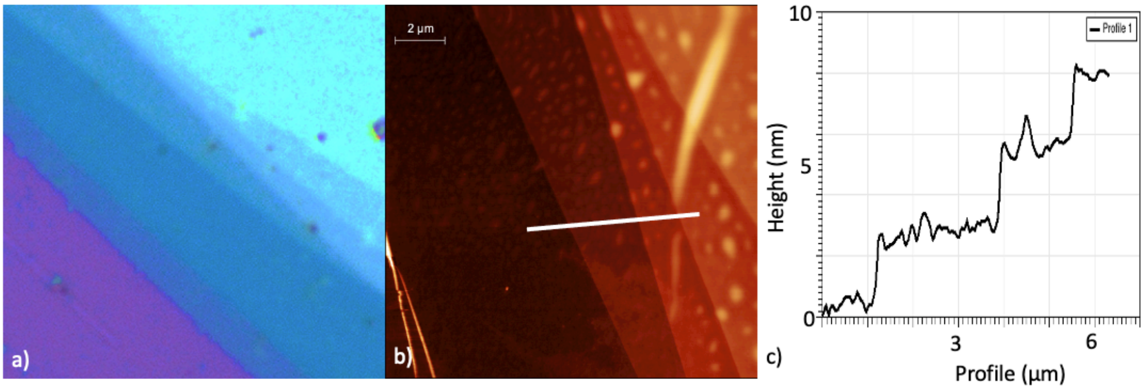

Figure 3-2. a) The optical contrast obtained from different layer thicknesses of a crystal of MoS2 on 300 nm SiO$_2$ b) An AFM image of the transferred flake. The white line indicates the trace shown in (b). c). Each step is around 2nm high, indicating each step in the flake is 3 layers of MoS$_2$[52].

3.2.2 Identification of Plasmonic Nanoparticles

3.2.2.1 *Dark Field Optical Microscopy*

Two techniques were utilised to confirm the distribution of the AuNPs on the surfaces. Firstly, dark-field (DF) optical microscopy was used to very quickly identify the distribution and density of the particles, and AFM to characterise them on a sample.

In DF optical microscopy, a patch stop is placed between the sample and the light source to create an annulus of illumination on the surface. This ensures any light which illuminates the sample is not collected by the objective lens. Therefore, only light scattered, or emitted, by the sample will form the image, with the rest remaining dark.

This technique is therefore very useful for the characterisation of plasmonic nanoparticle distributions. Due to the coherent oscillation of electrons on the surface of the nanoparticle, there is a very strong absorption and scattering of light at the SPR frequency of the particle. Therefore, it becomes very easy to see particles that are smaller than the diffraction limit of the optical microscope. Often, a long integration time, on the order of a few seconds, is required to obtain a good signal-noise ratio. Due to the high sensitivity of the nanoparticles' plasmonic resonance relative to their size, the RGB colour of the NPs on the CCD can be used as a very accurate tool to classify the NPs, with their colour determined by its peak SPR, as illustrated in Figure 3-3[53].

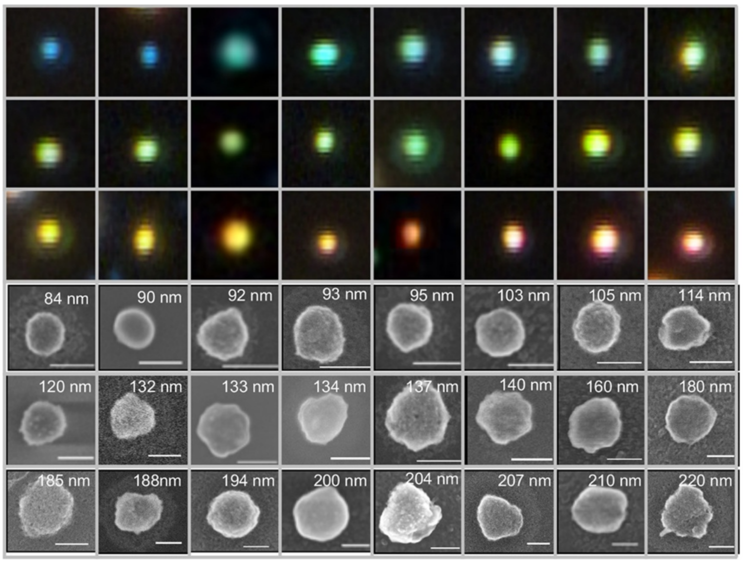

Figure 3-3: Change in colour in RGB response of AuNPs as the physical size changes. Reprinted with permission ACS Nano. Copyright 2019 American Chemical Society[54].

The distribution of 100nm AuNPs deposited on a surface in DF optical microscopy and SEM is shown in Figure 3-4.

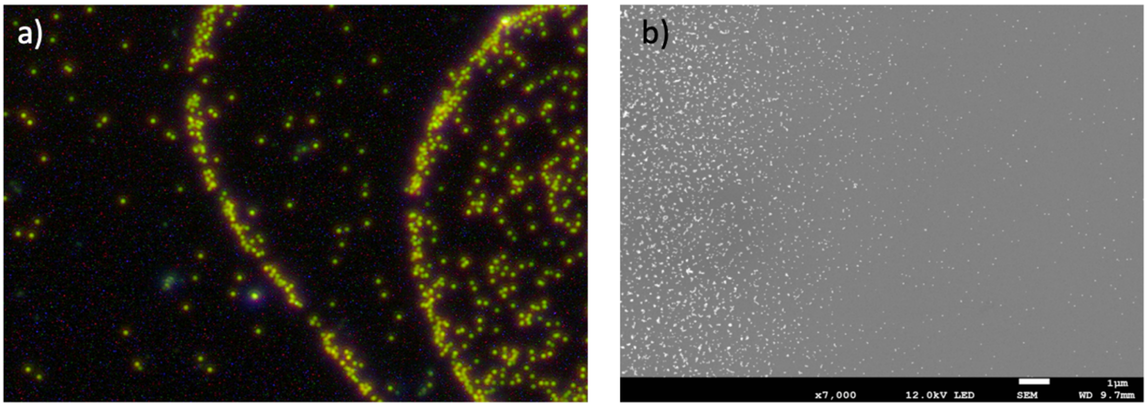

Figure 3-4: a) Dark-field optical imaging of 100nm AuNPs. The observed colour from the scattering is directly related to the SPR of the nanoparticles: larger clusters or different sizes will change their SPr. b) SEM image of AuNPs deposited on a surface, showing the high density at the edge of the 'coffee ring', and very few NPs elsewhere.

3.2.2.2 Scanning Electron Microscopy

Scanning electron microscopy (SEM) was used to characterise the AuNP substrates, as a fast technique to observe the density of AuNPs on a surface. This verified the distribution of NPs across the sample and helped to verify their size. An SEM image of AuNPs on the an SiO_2 surface is shown in Figure 3-4a.

3.3 Atomic Force Microscopy

Atomic Force Microscopy (AFM) was used for characterisation of the material, to observe both the device's structure and its nanomechanical properties. An AFM uses a sharp probe, which periodically raster-scans across the surface to measure its profile. It allows for a much higher resolution image, far beyond the optical diffraction limit imposed by optical microscopy.

The sharp tip is on the end of a long, reflective cantilever, which sits above the surface. A laser is pointed at the end of the cantilever, which is reflected towards a quadrant detector. As the tip moves across the surface, the tip moves up and down with the topography of the surface due to the repulsive coulomb interaction at the tip-surface interaction. These often sub-nanometre movements are then amplified due to the distance from the cantilever to the detector. A feedback loop then moves the height of the sample to ensure the force on the tip remains constant.

PeakForce Quantitative Nanomechanical Mapping (QNM) is a proprietary scanning mode developed by Bruker, but it obtains several additional metrics about the materials nanomechanical properties, including its adhesion, deformation, and Young's modulus which can be extracted. Instead of the probe being in persistent contact with the surface, it oscillates at the resonant frequency of the cantilever. In PeakForce QNM, the maximum force applied by the tip to the sample is fixed. As the tip approaches the sample, the vdW forces attract the tip towards the surface, and eventually the tip is pulled into the surface, at the 'peak force'. A feedback loop within the microscope then starts to withdraw the tip. The force experienced by the tip allows for the characterisation of the surface's adhesion.

Figure 3-5 shows how quantitative sample data can be obtained from the force curves in QNM. Extraction of the data from the force applied to the tip during oscillation allows many additional nanomechanical properties of the sample to be obtained, in addition to the topography, including adhesion, deformation, and a fit of the reduced Young's modulus (DMT modulus). This is extracted from the force applied to the cantilever, as a function of height on the sample surface, and time.

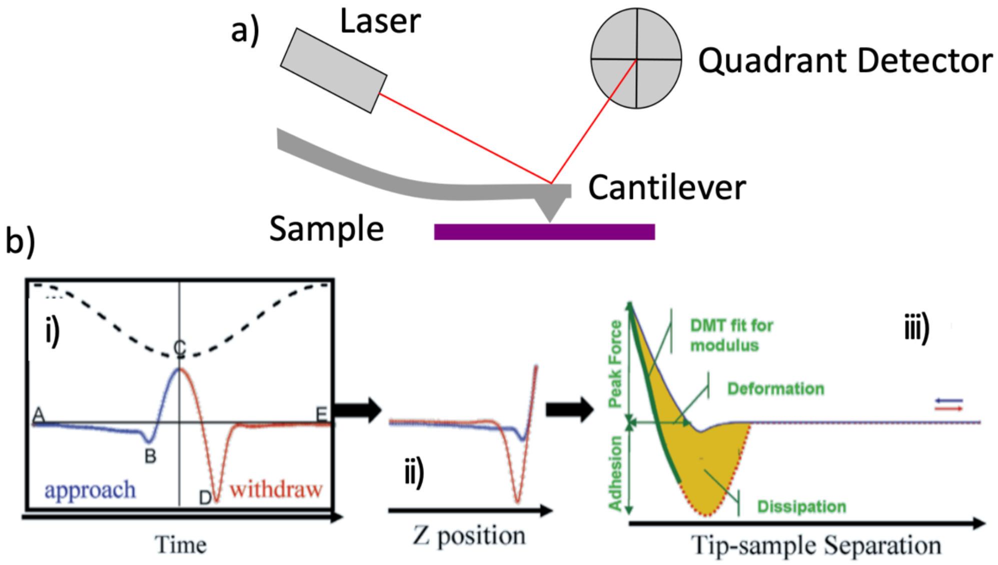

Figure 3-5: a) Schematic of a basic AFM setup. The cantilever raster scans across a surface. As the tip interacts with the surface, the cantilever will move, which is measured by the reflection of a laser on a photodetector. b) i) A force-distance curve showing how the force applied to the cantilever changes as a function of time. A – Cantilever approaching surface B – Tip jumping to contact surface C – Peak Force D – Adhesion of tip to surface E – Tip withdrawal ii) Plot of force vs. distance. From these two sets of information, we can obtain: iii) Mechanical properties obtained from the tip-sample separation vs force for PeakForce AFM, including adhesion, deformation, and a fit of the DMT modulus. Reproduced from Bruker[55].

3.4 Optical Techniques

Methods which measure the optical properties, including Raman and photoluminescence spectroscopy were utilised to confirm the properties of the samples and then interrogate the O-PUFs by measuring their given response to a challenge. The challenges to the O-PUFs include illuminating the devices with either a coherent or broad band light source and measuring the resulting response.

3.4.1 Photoluminescence (PL)

Photoluminescence (PL) is a technique used extensively to characterise materials and, specifically in this thesis, optical semiconductors. The device is exposed to a light source with energy greater than the bandgap of the material, and the light emitted by the sample is measured by a CCD. Some of the photons from the light source are absorbed by electrons in the VB of the semiconductor, which are then promoted to the CB, creating an exciton. In the CB, the electrons then undergo energy and momentum relaxation through Coulomb and phonon scattering, towards the CB minimum, where it can then recombine with the hole in the VB. This recombination can either be radiative, where a photon is then emitted with energy equal to the material's bandgap, or non-radiatively (such as through SRH or Auger recombination).

In this thesis, two types of PL measurements are performed to characterise PUFs: micro-PL and macro-PL, each with their own advantages for measuring the properties of these devices.

3.4.1.1 Micro PL

Micro-photoluminescence was used extensively throughout this work to characterise the emission properties of the O-PUFs. Micro-photoluminescence uses a laser with a 1µm spot size, focussed on a surface to probe the PL properties of a sample at a single point. It was performed both at room temperature, and low-temperature, with samples cooled to 4K. This enabled more information about the structural properties of the samples to be obtained: at low temperatures, phonons are suppressed, decreasing the FWHM of the peak, potentially revealing features in the spectra which are suppressed at room temperatures. This enables the observation of some properties which are mediated by local defects, ordinarily suppressed at room temperatures, due to scattering from phonons. Room temperature PL measurements were performed on a Horiba Jobin-Yvon LabRAM HR Raman spectrometer, with a 532nm CW laser, which enabled maps of the O-PUFs to be taken, where individual spectra were captured over specific sample areas.

3.4.1.2 Macro PL

In macro-photoluminescence, instead of a confocal laser with a small spot size measuring the sample point-by-point, a 50x lens was used to image the whole sample simultaneously. Whilst this provides a much lower power density on the sample surface, it gives a higher degree of spatial resolution, and is faster in characterising the whole sample, compared with several individual measurements. This gives the opportunity to very easily correlate physical characteristics with its optical properties. A schematic for the macro-PL setup is shown in Figure 3-6.

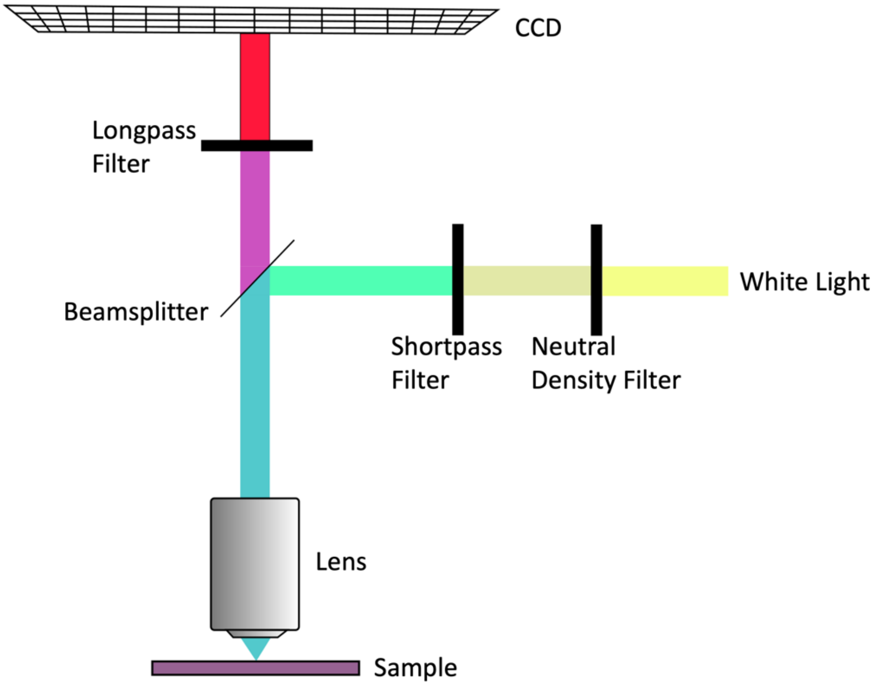

Figure 3-6 Schematic of macro PL setup. The LP filter removes any light which is reflected from the sample surface, so only emitted light from the sample is acquired by the CCD.

Samples are illuminated using a white light source passed through a short-pass filter, so the energy irradiating the sample is greater than the band gap of the material. The emitted and reflected light is then collected by the 50x, 0.75 numerical aperture (NA) lens, where it passes through a long-pass filter before reaching the CCD. This combination of filters ensures only emitted light from the sample is captured by the CCD. This enables a large spatial map ($>100\mu m^2$) to be taken in a single acquisition, which is considerably faster than a point-by-point map taken using micro-PL.

Additionally, Macro-PL is an effective technique for fast identification of single-layers of optically-emitting 2D materials during device fabrication. Only a single layer of WS_2 or MoS_2 emits brightly enough to be detected by a conventional CCD, because the radiative recombination for ≥2 layers is not efficient enough to be visible by most detectors. Figure 3-7 shows a crystal of WS_2 which has been exfoliated onto an Si + 300nm SiO_2 substrate. A large monolayer is visible, attached to a large bulk crystal. Figure 3-7 shows the macro-PL acquisition of the sample, where the only region which is visible is the single layer, emitting flake. It also reveals some features which are not visible using conventional optical microscopy, including folds or cracks.

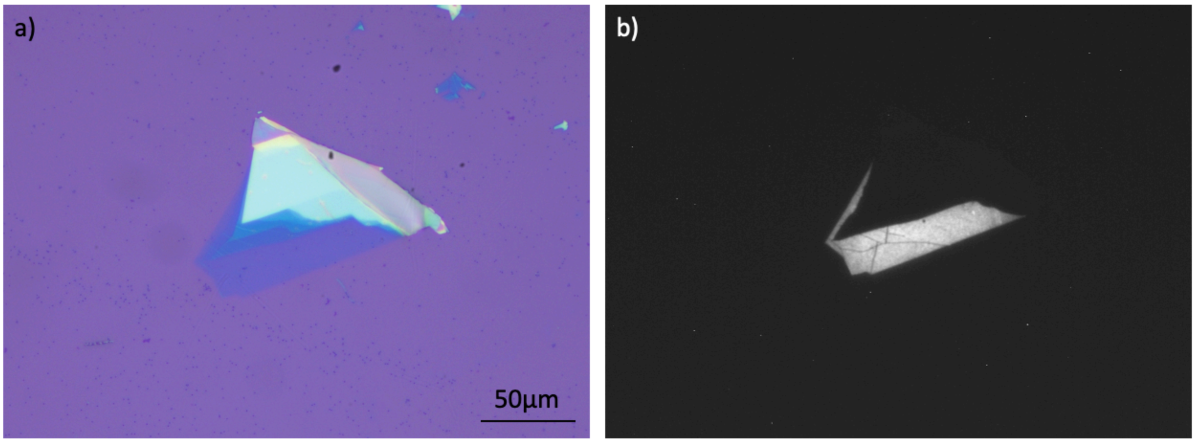

Figure 3-7 a) A multi-layer crystal of WS_2, with a large monolayer flake. b) Macro-PL image captured of the same flake. Only the single layer region with the direct band gap emits brightly enough to be visible. Features invisible by optical microscopy such as the cracks become apparent.

Whilst it has some significant advantages, macro-PL does not allow for the acquisition of the full emission spectra, instead allowing for a faster method to characterise the emission properties of a whole sample simultaneously. Benefits and disadvantages of each type of measurement is detailed in Table 1.

	Micro PL	Macro PL
Illumination Method	Single coherent wavelength. Can excite samples resonantly.	Broad band excitation, with range set by short-pass filter.
PL Map Size	Small, around 50µm^2. Limited by time.	Much larger, over 100µm^2. Limited by objective lens power and diffraction limit.
Acquisition Time	Long, several hours – requires point measurements for each spectrum.	Very fast – can acquire emission from all points simultaneously.
Measurement resolution	Limited by laser spot size, around 1µm.	Limited by light diffraction limit, around 400nm.
Spectra	Full spectra acquisition at each point.	Only emission intensity within the 2 BP filters is acquired. No spectra can be obtained.

Table 1: Comparison of micro and macro-photoluminescence techniques.

3.4.2 Raman Spectroscopy

Raman spectroscopy is an optical characterisation technique used to extract properties of materials through the elastic scattering of a coherent light source, usually a laser, with molecular bonds and phonons. In this project, it is primarily used as a characterisation technique to obtain properties of 2D materials, including layer-thicknesses of vdW crystals, and doping properties.

The Raman spectra of 2D materials, including TMDCs and graphene, are highly sensitive to layer thickness, so this technique can be exploited to quickly identify single-layer candidates. In MoS_2, the absolute separation between the two main spectral peaks is strongly dependent on the number of layers. Likewise, with WS_2, the ratio of the heights of the two main peaks gives a strong indication of the thickness of the crystal. Once possible candidates have been identified using optical contrast, room-temperature Raman spectra were taken of the individual flakes. Raman spectroscopy can reveal not only the layer thickness of a 2D crystal but, because it arises from the fundamental vibrations of the phonons within the crystal lattice, further properties about the strain and doping of the flakes can be obtained.

3.5 Processing Techniques

To optimise the quality of 2D samples on a flat substrate, the SiO_2 substrates with an RMS surface roughness of 0.5nm were cleaned freshly in an Ar/O_2 plasma immediately before the transfer, to remove any contamination from organic adsorbates on the surface which will aid the transfer process[56]. Once transferred to a substrate, the interface between the flake and substrate was optimised by annealing in a vacuum. There is commonly a gap of 1-2nm between the substrate and flake which can be attributed to hydrocarbons trapped during the transfer process. Larger bubbles also appear across the sample which are formed as the 2D layer is pressed onto the surface. To improve the interface, the samples were annealed at 1mbar at 200°C for 3 hours, during which the hydrocarbons are energetic enough to migrate, and aggregate at sites under the flake. This creates areas of the sample with large bubbles, but large areas which are free of these defects with a good interface with the substrate. This process relieves some of the strain in the layer which occurs during the transfer procedure, creating larger areas to study in the absence of strain or contaminating hydrocarbons beneath the surface. The effect of the annealing process is shown in Figure 3-8, with the annealing of a WS_2 + MoS_2 vertical heterostructure, where the organic contaminants become mobile to improve the interface between the crystals, reducing the overall surface roughness. It is shown that the surface interface is improved under these conditions due to limitations of the oven, I was not able to investigate the effect of temperatures >200°C.

Surface roughness calculations were performed for both the substrate flake and the transferred WS_2 before and after this annealing. It was found that the MoS_2 substrate had an average roughness, Ra, of 2.99nm before annealing, which was reduced to 1.20nm. The transferred flake had an average roughness of 7.26nm, which reduced to 3.37nm after annealing. The relatively high roughness for the transferred flake is due to the larger bubbles which remain under the surface after the migration of organic compounds. Figure 3-8 shows AFM images of 2D flakes before and after the vacuum annealing, with profile traces.

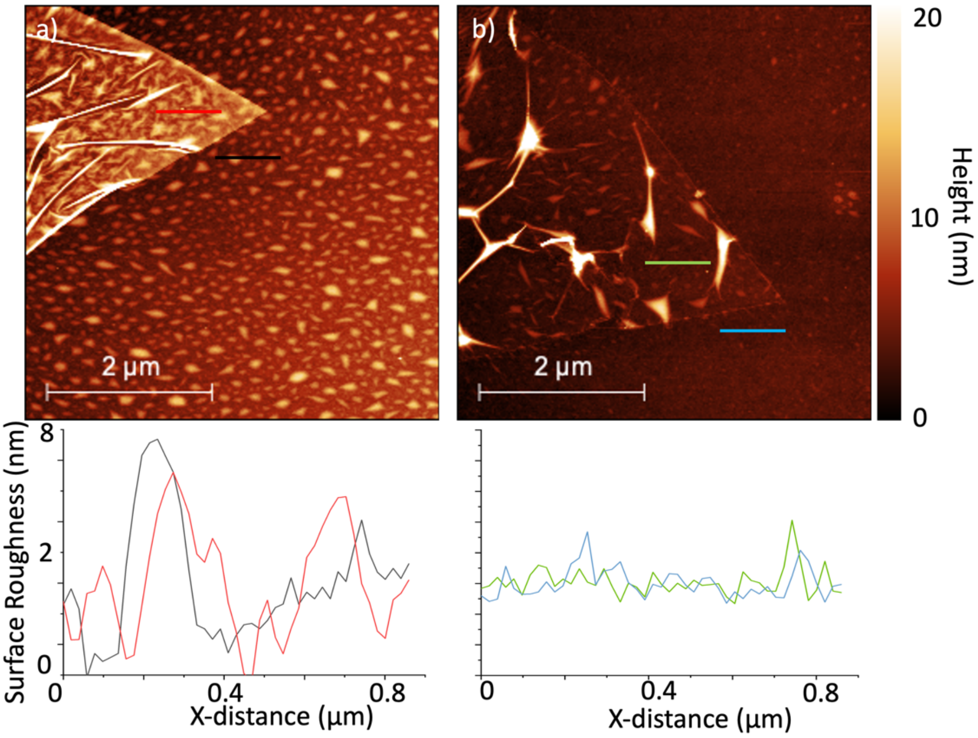

Figure 3-8. 2D material flakes before (a) and after (b) vacuum baking at 200°C. A flake of WS_2 transferred onto a MoS_2 substrate. Large bubbles are created from the migration of organic contamination.

Chapter 4

Nonlinear Emission Characterisation of Quantum Dot-Based Optical Physical Unclonable Functions

This chapter introduces modifications to an existing classification of quantum dot optical PUF (QD O-PUF) by measuring not just the position, but also the intrinsic optical emission properties of the quantum dots to verify the authenticity of the device. Firstly, a photoluminescence map of a sample of randomly distributed colloidal QDs is measured at increasing excitation powers, and the nonlinear response and optical properties as a function of position are characterised. This demonstrates an increased number of possible challenges for a PUF, without increasing the size of the device or the complexity of the measurement technique. The introduction and effective use of the characterisation of the linearity and switch-on response from the samples increases the pool size of challenge-response pairs (CRPs) and, by confirming the presence of quantum material on the surface, makes this design of O-PUF more difficult to replicate or simulate.

Subsequently, a modification to this PUF is demonstrated, using a new technique for modifying the emission properties of the quantum dots through the addition of plasmonic nanoparticles to the surface. The motivation for this modification to the PUF's design is to dramatically increase the dynamic range of emission intensities of the QDs, leading to an increase of the density of CRPs within a tag. If both the position and relative emission intensity shifts of the particles is considered, where most common iterations of this design do not consider the relative intensity of emission across a sample, an additional set of CRPs can be generated. The plasmonic nanoparticles interact with the QDs on the sample surface, dramatically increasing the dynamic range of emission intensity.

4.1 Introduction

Chapter 2 gave a broad background to existing O-PUFs. This chapter focusses on nanoparticle-based PUFs and improving their evaluability with an improvement to the measurement technique. Nanoparticle O-PUFs (NP-PUFs) are a very attractive classification of O-PUFs: they are reliant on the random distribution of an optical nanoparticle, such as quantum dots or plasmonic nanoparticles, and their interaction with the challenge. Their unpredictable fabrication technique ensures that when the nanoparticles are deposited on a surface or embedded within an object, were the fabrication process repeated, it would yield different results[57]. This leaves a pattern of nanoparticles that is unique, so a challenge which is presented will provide a unique response. It is this fundamental property from which this category of PUF obtains its security. The use of a random distribution of nanoparticles as a unique tag is attractive because the size of the particle is directly related to the effort required to replicate a tag: PUFs whose security relies solely on measuring the position of nanoparticles mean that fabrication or simulation on the same scale as the original tag is required to counterfeit it. However, with such high-resolution measurements that are required to authenticate a genuine tag, it makes it much less practical for a consumer to measure a device and interpret the results[58]. Figure 4-1 shows examples of existing nanoparticle PUFs, which all rely on the measurement of a random distribution of NPs, optically, or using higher-resolution techniques. Figure 4-1a shows the uniqueness obtained from the random 'pinning points' obtained as a solution dries, creating a unique fluorescing pattern[12]. An alternative method is the inkjet printing of QD-based inks. Figure 4-1b/c have similar concepts, upon which the PUF described in this chapter is related, where a solution of colloidal NPs is randomly distributed on a surface[58]. The unique pattern created is then characterised using optical techniques, including macro-PL, or surface-enhanced Raman spectroscopy (SERS).

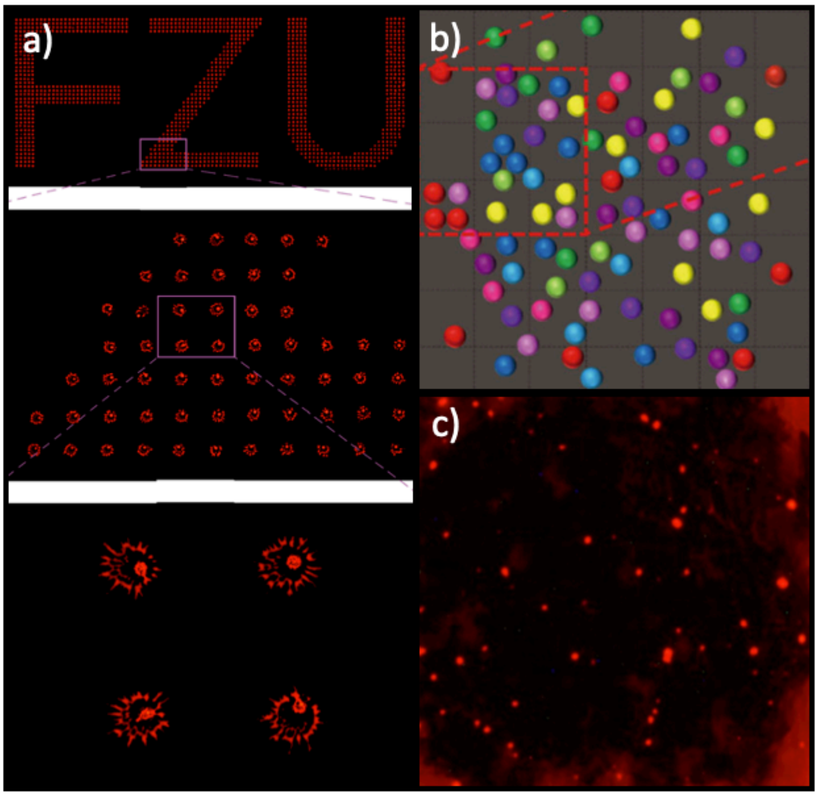

Figure 4-1: Examples of existing nanoparticle O-PUFs. a) The position of the optical emitters arises from random 'pinning points' from drying solvents, b) shows the random positioning of SERS nanoparticles as the source of security, and c) shows a random distribution of colloidal QDs on a surface. a/b used under CC-BY license, c) Reprinted with permission from Arppe-Tabara[58]. Copyright 2019 American Chemical Society.

In this chapter, the concept of nanoparticle PUFs as an optical method of secure authentication is discussed, and new characterisation techniques are introduced to improve their security. The addition of a second optical measurement of the emission linearity and, furthermore, the addition of plasmonic nanoparticles to locally modify the electromagnetic field adds a new dimension of security for the existing device. These additional layers of security improve existing constellation-style O-PUFs, whilst keeping the fabrication methods very simple. Whilst PUFs from distributions of nanoparticles have been widely discussed in the literature, they suffer from a similar set of weaknesses, which can leave them potentially vulnerable to attack, or impractical for a consumer to measure[3]. This chapter demonstrates a simple and powerful method of characterising optical PUFs to create a more secure tag, whilst not requiring the ability to characterise individual nanoparticles. These devices take the form of well-established nanoparticle PUFs, consisting of a random distribution of an optical nanoparticle embedded or deposited within an object, or on a surface, but with a simplified method of characterisation. Due to the balance between ease of characterisation, and resolution and security of the O-PUF, this device has a lower measurement resolution than some other NP O-PUFs, but introduces an additional security check for authentication, with a simpler measurement technique using far-field optical microscopy.

Firstly, the basic properties of position dependent, constellation-style PUFs are introduced, demonstrating the improved level of security with the measurement technique. Subsequently, the relative emission intensity of different regions across the sample as part of the authentication process is introduced. The ‘constellation-style’ category of O-PUF discussed so far focusses on the position of an optical material, as a static object. The introduction of a secondary measurement has the potential to strongly increase the overall security through an additional check of authenticity. In this chapter, the relative emission properties of the sample are used to increase the overall security of the device.

Using a random distribution of QDs on a surface provides uniqueness through the unpredictable and uncontrollable fabrication method, but the relative intensity of the emission of the QDs, whilst it can vary somewhat due to local QD density, is reasonably uniform[14,59].

Secondly, this chapter aims to increase the bit density of a QD O-PUF. The number of useful bits that can be extracted from a PUF is directly related to the full range of analogue values that a given PUF can provide before a digital measurement is made. In this case, to increase the range of CRPs that a QD-PUF can generate, either the spatial resolution of the measurement must increase, or the dynamic range of a measured characteristic can be increased. For this study, the latter is much more attractive: to increase the resolution of the measurement contradicts a key figure of merit of a consumer PUF to be easily characterised, because it comes with additional requirements for more complex measurement techniques[60,61]. Here, a more straightforward method to increase the overall dynamic range of emission intensity values emitted across a sample, using plasmonic nanoparticles, is shown. This method advances current techniques and methods of optical nanoparticle PUFs. This chapter uses InP/ZnS core/shell QDs due to their lower toxicity, high QY, and useful emission wavelength for this application: visible and NIR wavelengths are desirable for PUFs because they are easiest to be detectable by conventional silicon-based sensors[62].

4.2 Optical Properties of Nanoparticles

4.2.1 Optical Properties of Colloidal Quantum Dots

The fundamental origin of security of conventional nanoparticle based PUFs is the random distribution of the optical nanoparticles, as a result of an unpredictable fabrication method. This provides a reasonable level of security, and whilst it guarantees an asymmetry between the ease of initial fabrication and replication, such that it is generally impractical for an attacker to be expected to be able to replicate, they are generally 2-dimensional in response – they require replication or simulation of particle position only. This restriction, whilst potentially impractical for a nefarious party to achieve, opens the door to potential cloning or simulation, for example, by an array of LEDs[60]. To improve the intrinsic security of these types of tags, this chapter aims to add a new dimension of security for existing constellation-style QD-PUFs solely through an improved measurement technique.

The use of colloidal quantum dots as the foundation for constellation-style O-PUFs has significant advantages. Due to their quantum confinement in all dimensions, their emission characteristics are very tuneable to their size[63,64]. This enables the creation of O-PUFs with emission ranges at a wide range of desired wavelengths. QDs also generally are surrounded by a set of ligands, which are either remaining from the fabrication process, or alternatively, can be added or modified to change their properties. From a fabrication point of view, the ability to add and change ligands on the surface of the QDs is beneficial because it enables them to be suspended in a variety of different solvents[65,66]. In this work, the distributions of QDs on surfaces was achieved using an electrospray method, so it was important the ligands on the ZnS/InP QDs for these devices were soluble in a polar solvent.

Additionally, these ligands have the capability to modify the excitonic states in the QD. Different ligands on the QDs impact both the quantum yield of the QDs and their emission peak wavelength and linewidth due to their high sensitivity to confinement energy[63,64]. The unpredictable nature of ligand binding creates a region of unpredictability in the emission properties of an individual QD.

Naturally, ligands also change the bonding and clustering properties of groups of quantum dots, which is beneficial when fabricating random distributions: different sized ensembles of dots will modify their electronic properties, so the optical spectra will change spatially across a sample that contains a varying density of QDs. Clusters of QDs, which are here defined as larger, dense regions of

QDs, which are likely to be interacting with one another will appear to ‘switch on’ earlier than the low-density QDs, which do not interact. This occurs for two reasons: first, due to the relatively high density of the QDs in a small region on the sample, there are more emitters undergoing exciton creation and recombination per unit area, relative to other regions on the surface. This leads to an emission intensity which is greater than the threshold detection intensity of the CCD to be reached earlier than lower density areas. Secondly, when in close contact, charge carriers may tunnel through the interface between two dots, leading to an increased recombination rate[67]. A charge that reaches the surface of the QD may be attracted to another QD. This mechanism, known as ejected charge exchange (EQE), essentially ensures the QDs are constantly excited, shortening the lifetimes of the recombination.

For optically pumped quantum emitters, their radiative emission from neutral excitons saturates as:

$$R_{em} = \frac{R_{sat}}{\left(1 + \frac{I_{sat}}{I_{ex}}\right)} \tag{4-1}$$

where R_{em}, is the emission rate when excited at incident intensity I_{ex}, and R_{sat} is the saturation emission intensity, at I_{sat}[68]. When illuminated with a lower power density, the emission characteristics are dominated by the linear emission from neutral exciton recombination. However, as the excitation power increases, as each exciton recombines, it is immediately replaced by another, so the ground state of the QD is always occupied by an electron-hole pair, saturating the emission[69]. As the pump rate approaches the peak emission rate of the QDs ($1/\tau_{QD}$), the emission is saturated and the rate of emission no longer increases, because no more charge-carrier pairs can be generated. This is the foundation of the new layer of security in our tags, where the nonlinear response of the QDs can be exploited as a supplementary check, to ensure the authenticity of the device. This behaviour in response to a challenge is far more difficult to replicate or simulate. Characterising not only the position of the nanoparticles, but their response at different excitation intensities and different switch-on intensities, creates a further test to authenticate the tags.

Figure 4-2a shows representative data, demonstrating types of response from across a surface, with different switch-on points at different regions and position-dependent peak intensity. The local density of QDs on a surface plays a large part in their emission properties: when tightly packed, they don’t behave in the same way as individual dots[70]. Generally, due to their high density, clusters appear as a very bright region on a sample, but if packed very densely, their emission can quench[71,72]. The random deposition process of electrospray can create nonuniformity in the distribution of QDs on the sample surface, including regions with very few quantum dots, alongside large, dense clusters.

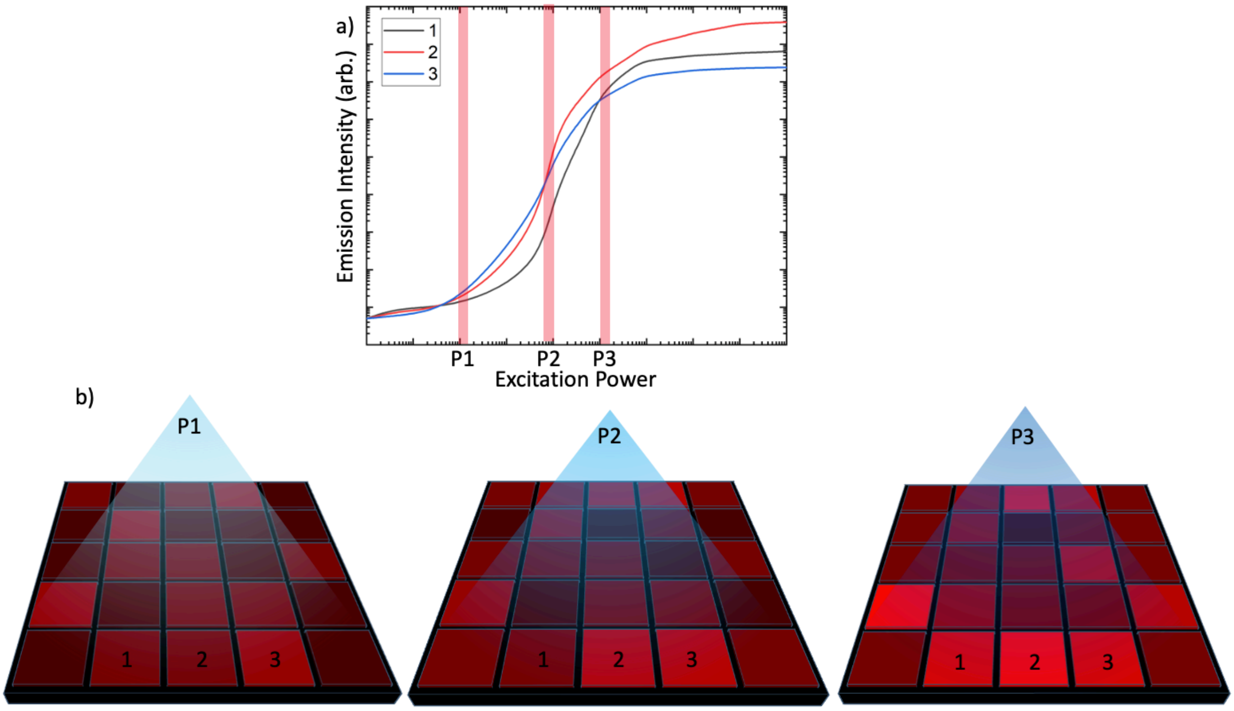

Figure 4-2: a) Representative data showing different responses of QD regions across a nonuniform sample. P1, P2 and P3 refer to the 3 increasing excitation powers. Substrate and local density properties ensure different switch-on rates, and final emission intensity. The three labelled areas on the surface represent three types of region on the sample, which switch on and saturate at different powers.

4.2.2 Optimisation of Conditions for Plasmonic Enhancement

Metallic plasmonic nanoparticles, primarily silver, copper, and gold (AuNPs), have been extensively used in a range of applications, primarily optical applications, such as for medical imaging. Their unique electronic properties allow for them to be exploited for their interaction with the electromagnetic spectrum. The work in this chapter exploits their strong optical properties to create highly localised enhancements to the electric field at the sites of the NPs, producing a significantly enhanced photoluminescence (PL) 'hotspot' around it.

Metallic nanostructures strongly increase the local electromagnetic field at resonant frequencies which are strongly dependent on the size and shape of the NP. Conventionally, this effect is used to enhance the PL or Raman scattering of a nanocrystal for imaging, such as in tip-enhanced Raman Spectroscopy (TERS). However, the proximity of the plasmonic NP to the QD generates a rapid non-radiative relaxation path for the charge carriers, which dominates over the radiative pathway. The mechanism of this optical enhancement is described in detail in Chapter 2.3, but the important effect for this work is that it creates a balancing act of emission enhancement vs suppression that must be considered: if the NPs are too close to the emitting QDs, there will be a strong quenching effect, so the enhancement is heavily dependent on plasmon-QD distance. The energy is transferred from the quantum dot's excited dipole to excitations in the metallic nanostructure through a non-radiative channel, so this distance must be tuned to obtain the optimal coupling[50,73-75]. Therefore, peak overall emission enhancement from the QDs must be obtained by optimising several conditions: firstly, the SPR of a plasmonic nanoparticle is very sensitive to its material, size and shape[76]. If the SPR peak doesn't overlap with the excitation or sample emission wavelength, there will be no increase in local light intensity or radiative transition rate[77,78]. The second factor which is important to optimise is the distance between AuNP and light emitting QDs, so different thicknesses of dielectric were deposited between the AuNPs and the QD film to obtain the best spacer thickness.

In this work, 100nm gold nanoparticles (NPs) were selected for their straightforward manipulation, and peak surface plasmonic resonance (SPR). The most common particle shape is spherical, but as the spheroid elongates, the surface plasmon resonance redshifts. Gold and silver NPs have the most desirable optical properties in the visible and NIR range. Ag has the lowest losses in these ranges, but is less chemically stable than Au, so AuNPs have been selected for this work. Spherical particles create coherent oscillations of the conduction electrons: as they are displaced, the restoring force from Coulomb attraction acts to return them towards the nuclei.

In addition to the dielectric spacer, the physical distance between the AuNPs and QDs is nonuniform, due to the unpredictable nature of the deposition process: the QDs are deposited in the gaps between the AuNPs, but the absolute distance will vary across the sample. For the application of an optical PUF, this is where the increased dynamic range of emission values originates. Some individual QDs will sit within the enhanced electromagnetic field, created by the AuNPs, or between two plasmonic nanoparticles. The site between two nanoparticles can increase the overall light intensity at that site by a factor of up to 10^6, so this will increase the overall radiative transition rate[79]. Conversely, if the QDs are not situated close to an AuNP, or the dielectric is too thin at a particular site, the emission will not be enhanced, and could be quenched by the metallic nanoclusters.

4.3 Fabrication and Characterisation Methods

4.3.1 Electrospray Ionisation

To fabricate these samples, quantum dots were deposited using an electrospray technique. InP/ZnS colloidal QDs were dispersed in toluene, which is a polar solvent, so it is effective for electro-spraying. This method enables the fast deposition of a film of quantum dots (or any colloidal particle) onto a large area.

Electrospray utilises the polar nature of some solvents and exploits their behaviour in a high electric field. The colloidal solution is placed in a syringe with a 30-gauge needle, and a high potential difference of around 1kV is applied between the tip of the needle and the substrate. Due to the polar nature of the solvent, the large electrostatic force experienced by the solvent forces the solution out of the end of the needle. As the droplets move towards the substrate, the repelling charges within them force them to separate into smaller droplets, making it easier for them to evaporate. This reduces the amount of solvent that arrives at the substrate, to prevent excess aggregation due to a solvent film on the surface. It provides an ideal distribution for this type of NP-PUF: whilst this technique does not completely eliminate aggregation, it provides a much more uniform distribution than drop-casting. The experimental setup schematic is shown in Figure 4-3. Whilst drop-casting is a faster technique for individual samples, for these devices to be scalable, electrospray is capable of depositing QDs onto more samples simultaneously. Drop-casting also has severe aggregation problems for this category of device where a more uniform film is desired. As the solvent evaporates to leave the QDs on the surface, the QDs accumulate in the regions where the solvent has dried. This leaves too many regions on the sample surface which are free from QDs, making characterisation more difficult and reducing the overall information density. Whilst the solvent cannot be eliminated entirely from the substrate during deposition, this process reduces the clustering severity of the clustering observed compared with drop-casting by reducing the amount of migration of nanoparticles on the surface.

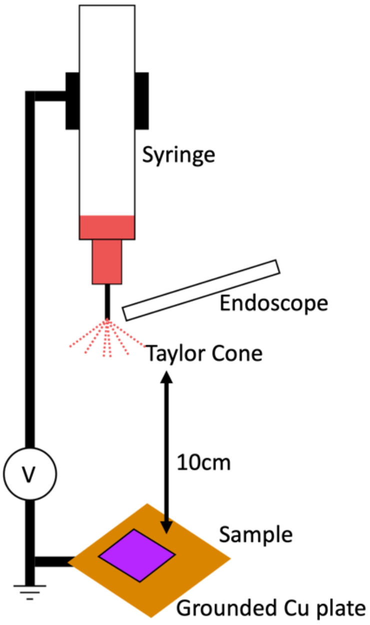

Figure 4-3: Electrospray Ionisation (ESI) experimental setup for deposition of a film of QDs. The high potential difference forces the polar solvent out of the needle, into a Taylor cone, ensuring a uniform distribution, with minimised solvent on the sample surface.

The substrates onto which the QDs were deposited for this project were Si/SiO_2, capped with a 200nm layer of aluminium using thermal evaporation. This reflective layer serves two purposes: firstly, in the range of visible light, its reflectivity is close to unity, so any light from the pump source that was unabsorbed by the QDs is reflected back, enabling another opportunity for it to be absorbed. Additionally, due to the spontaneous emission characteristics of quantum optical materials, a large quantity of the emitted light will be away from the CCD, so the addition of a reflective bottom layer ensures some of this is measured by the detector[80], increasing the external quantum yield of the sample. Aluminium oxidises very quickly in ambient conditions, so this film of Al_2O_3 will prevent the quenching of PL emission from the QDs[81].

To verify the increase of the dynamic range of emission intensity of devices with the modification with gold nanoparticles, two different types of samples were fabricated: sample A was a control sample, and sample B contained a distribution of plasmonic NPs, and an additional reflective layer of an aluminium array on the substrate. In addition to the reflectivity increasing the external quantum yield of the samples, the Al creates reference points on the surface, so specific regions of interest can be located easily. To prevent the emission quenching through the nanoparticles, a thin layer of 5nm TiO_2 dielectric was deposited on top of the Al+AuNP substrate: the thickness of this layer was optimised to obtain the peak emission enhancement. The optimal thickness of TiO_2 was obtained with subsequent studies on the peak emission intensity of samples fabricated with several different dielectric thicknesses, from 1-10nm. Further detail into the optimisation of the TiO_2 thickness optimisation performed by N. Abdelazim can be found in our published work[82].

Figure 4-4 shows the schematic for the fabrication procedure for the plasmonic sample. The pattern of Al rectangles on the SiO_2 substrate was deposited using optical lithography and thermal evaporation. The concentration of NPs in solution is optimised so there is a dense, but discrete, distribution across the surface, with an average coverage of 105-110μm^{-2}. 10µL of this solution was drop-cast onto the prepared substrates and, once the solvent had evaporated, they were treated in an Ar plasma cleaner, to remove any excess ethanol or other organic contamination from the surface. Drop-casting of nanoparticles was chosen for the deposition of the gold nanoparticles because it is very simple. Previous studies have investigated electrostatic deposition, chemical substrate treatment to increase NP adhesion, or other methods, such as Langmuir-Blodgett deposition, which are capable of producing very uniform films but require additional steps or equipment, which is less desirable for O-PUF manufacture scalability[83,84]. Unlike the electrospray deposition of CQDs used in this chapter, which obtained a reasonably uniform distribution, for the applications of unique function generation, a uniform plasmonic AuNP distribution is not desirable. Therefore, drop-casting, which induces localised clustering, was used, to modify spatially the emission properties.

Onto the array of AuNPs, a 5nm layer of titanium is deposited using electron-beam evaporation. The sample was then baked on a hotplate at 200°C in air to oxidise, making a thin layer of TiO_2, which is a dielectric, to prevent fast non-radiative recombination of charge carriers from the QDs. Deposition of a film of Ti this thick has some variability in film thickness due to it being below the percolation distance for this material, leading to island formation[85]. The thin TiO_2 layer has a negligible impact on the overall substrate reflectivity relative to the SiO_2 or Al reflectivity[80,86]. Additionally, the AuNPs cause shadowing of the TiO_2, so the AuNPs are still on the SiO_2 substrate at the bottom. With the substrates prepared, a distribution of QDs was deposited with an electro spray, which allows both control and plasmonic samples to be deposited at the same time to keep a comparable density of QDs across both surfaces.

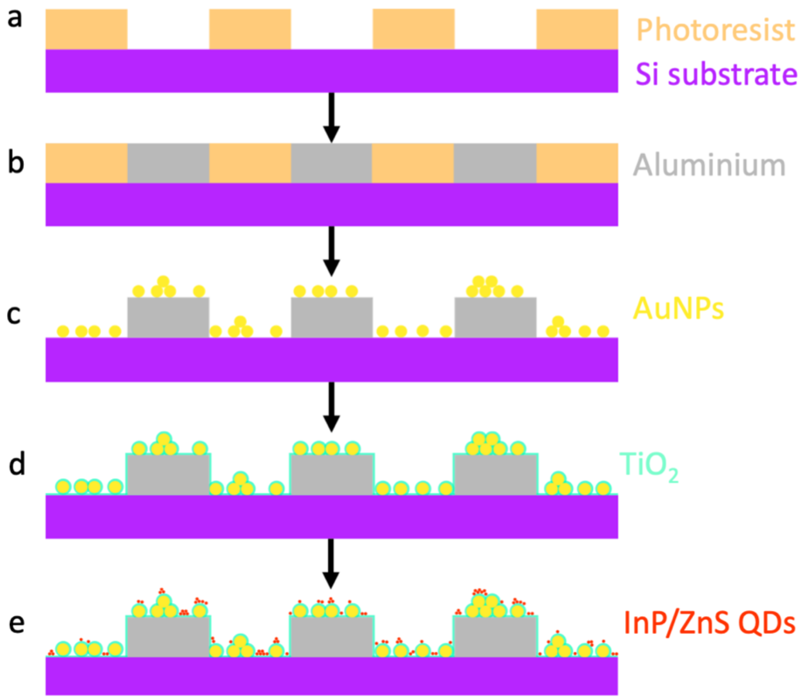

Figure 4-4: Schematic of fabrication steps of the plasmonic QD sample. a) Deposition and subsequent patterning of a positive photoresist on the substrate using optical lithography. b) The Al layer is deposited, and the array of Al grids is left when the resist is lifted off. c) AuNPs are drop-cast onto the substrate, and dried to form a random distribution over the surface. d) A thin layer of Ti is deposited on the surface and oxidised to TiO_2*. e) InP/ZnS CQDs are electro-sprayed onto the sample.*

Figure 4-5a shows the measured emission spectra of the QDs and the absorption peak of the 100nm plasmonic nanoparticles. For this project, the size of the nanoparticles was chosen such that there is a good overlap between their absorbance peak and the emission peak of the QDs. Figure 4-5b shows an SEM image of the QD distribution across the substrate. Importantly, the distribution of the AuNPs should have sufficient density for enough of the plasmonic NPs to interact with the QDs, but not so dense that the QDs don't fit into the gaps between them – there should be a reasonably uniform film of QDs between the AuNPs. The QDs are considerably smaller (around 5nm) than the AuNPs (100nm). AFM images shown in Figure 4-5c/d of the samples with and without AuNPs confirm the QDs are well distributed amongst the AuNPs. Large AuNPs, such as the ones used here have a relatively broad absorbance peak, so, whilst it will couple with a wider range of emission wavelengths, there is a weaker coupling experienced between the plasmons and excitons.

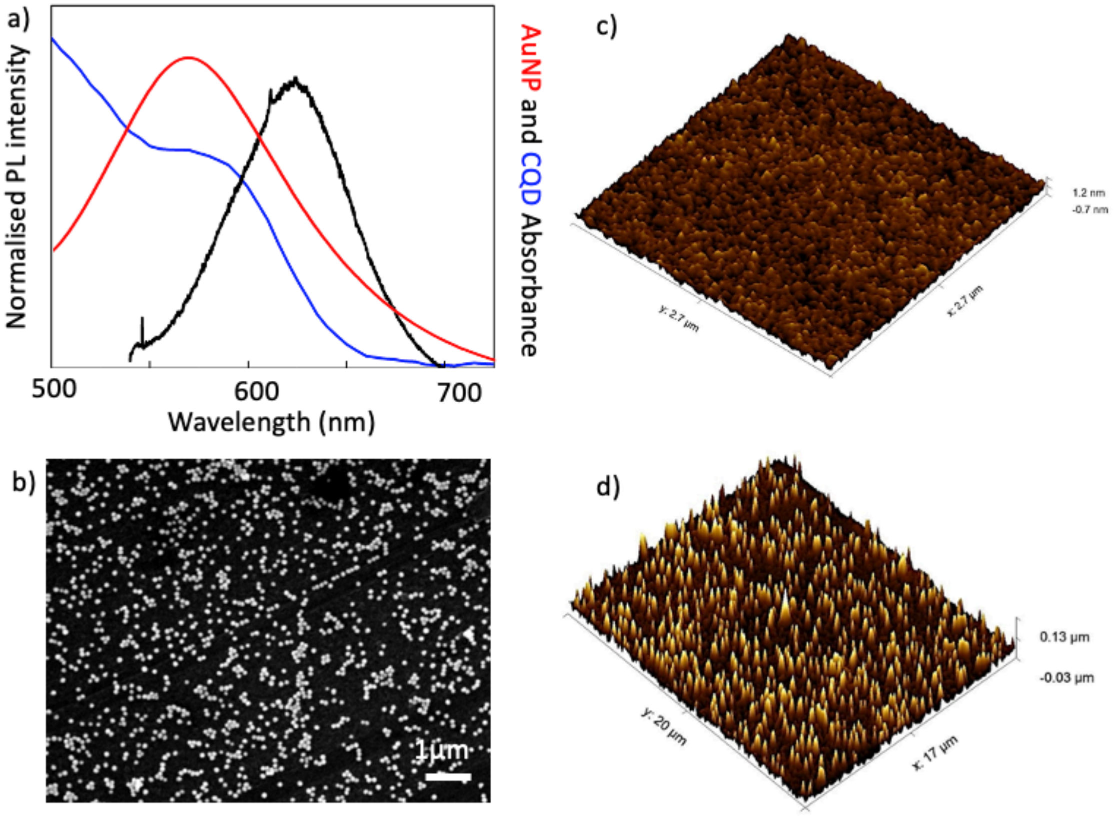

Figure 4-5: a) The absorption peak of the 100nm AuNPs (red) and the InP/ZnS QDs (blue), showing the overlap with the PL peak of the QDs (black). b) shows an SEM image of the distribution of the AuNPs on the sample surface. c) AFM of the QDs without AuNPs, and d) AFM image of the QD sample with AuNPs, showing the presence of the much larger 100nm AuNPs on top of the 5nm QDs. Figures b-d used under CC-BY license.

4.4 Measuring the Nonlinear Optical Response

The nonlinear quantum dot O-PUF was measured using macro photoluminescence (PL). This technique of photoluminescence using far-field optical microscopy is a far simpler and faster technique than many other characterisation methods for constellation-style PUFs, which can involve long, high-resolution measurements. This technique is detailed in Chapter 3.4.1.2, where images were captured of the sample with a 50x lens, with a 550nm short-pass and 600nm long-pass filter, to ensure only emission from the sample is detected by the CCD. A stable white light source and variable ND filter were calibrated with a Thorlabs S121C power meter, to obtain 10 different incident powers for sample excitation. Figure 4-6 shows the greyscale images of the sample, at 4 different representative excitation powers, where the presence of Al clearly increases the external efficiency of the device, and the larger clusters of QDs can be seen as the large bright spots on the sample.

4.4.1 Histograms and Pixel Numbers

The pixel-value histograms are extracted from each 16-bit greyscale image and show the number of recorded values (0 – 65,536) over the whole image. The macro-PL image and the resulting histogram for four excitation powers are shown in Figure 4-6.

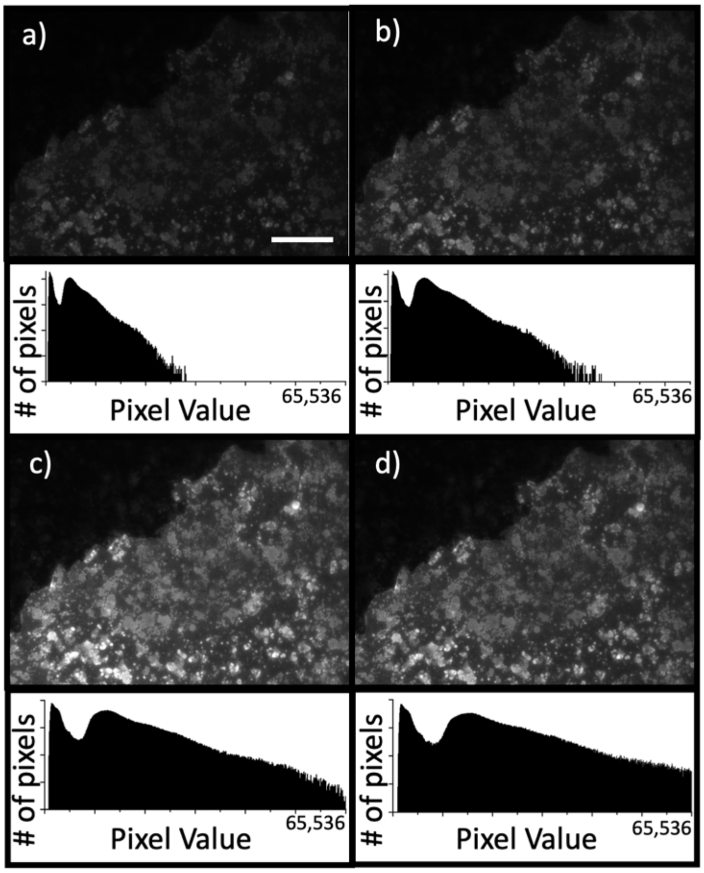

Figure 4-6: Histograms of normalised numbers of each pixel value at different excitation powers: a) 36.4μW, b) 57.6μW, c) 91.4μW and d) 145μW. The initial peak centres around 0 emission, which broadens with increased excitation due to the reflectivity of the sample. As the incident excitation increases, the pixel value starts to saturate at regions with the highest emission intensity. Scale bar indicates 20μm.

There are two peaks seen in each histogram: the first is centred around 0, which is no signal detected by a given pixel. At low intensity, this peak is highest at 0 counts, with a narrow distribution over pixel number, because the emission of the QDs at this power is below the sensitivity threshold of the CCD. This 'zero' peak broadens, with increasing incident intensity, because more light is reflected from the surface. The second peak shows the pixel value shared by most pixels and will be much more closely related to the properties of the material on the surface: in the low incident intensity powers, only a few regions, mainly the large clusters, on the Al-backed regions of the sample start to illuminate above the detection threshold of the CCD, so there is a relatively narrow, low pixel-number peak. As the incident power increases, this peak pixel number increases, due to the increased emission from the sample, and the peak also broadens considerably, as different regions on the sample switch on at different points: the larger clusters switch on first and have a much brighter emission, but the thin uniform distribution on the bare SiO_2 substrate switches on last, with a much dimmer response. As the incident intensity approaches the highest values, and all regions of QDs begin to saturate, the peak plateaus. The peak emission intensity arises from the large clusters of QDs on the Al substrate, but the majority of the surface area of the tag is still a more uniform distribution, which saturates at a much lower intensity.

4.4.2 Linearity Measurements

To characterise the different emission properties across the sample, the emission intensity response of different types of region across the surface were characterised, which is shown in Figure 4-7. When increasing the excitation power, the response of the regions of QDs on the surface was characterised. The three types of area measured are ‘background’ regions, where there is a low-density and uniform distribution of dots; ‘aluminium’ regions, where there is a similar uniform distribution but on the Al substrate; and clusters of QDs , which were the three brightest regions of high-density QDs on the Al substrate. These regions are the same as labelled on Figure 4-7, and their response to increasing incident power is plotted. All regions of the sample display a similar nonlinearity profile but differ in switch-on value and final overall emission intensity.

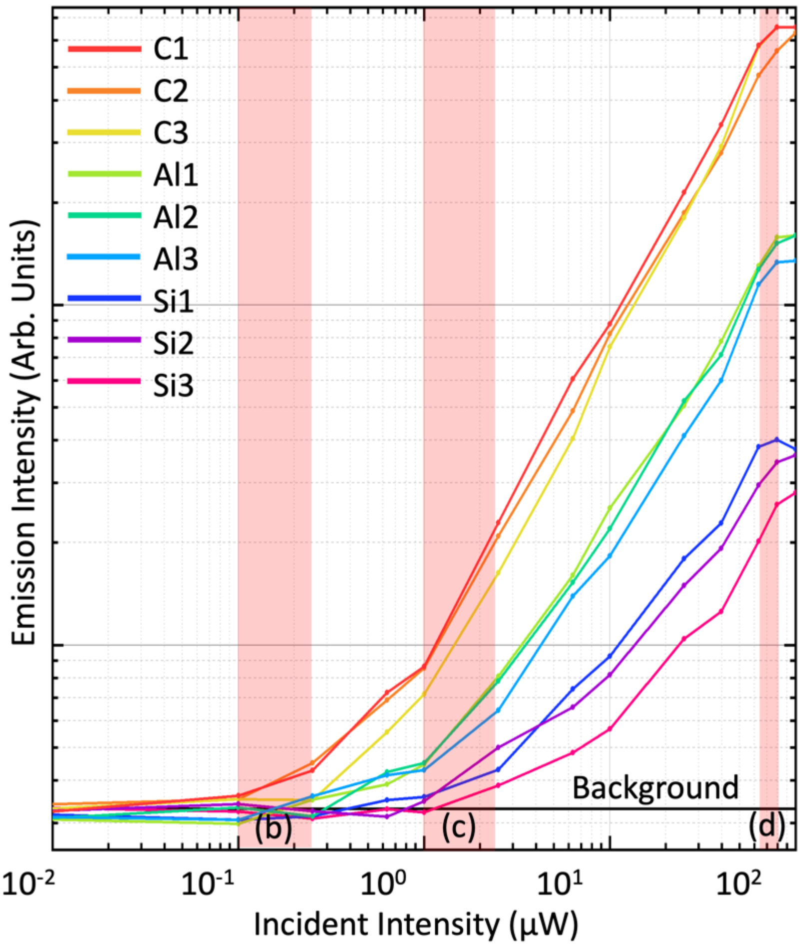

Figure 4-7: Characterising the incident power-dependent properties of the QD sample in different regions of background substrate and quantum dot density. A log-log plot of the emission intensity (arbitrary units) as a function of incident power for regions on the SiO_2 substrate (labelled Si), the Al substrate (Al) and very large clusters (labelled C). Regions labelled (b), (c) and (d) represent the range of emission values for the calculated images in Figure 4-8.

Figure 4-8 shows a series of divided sample images, where the PL map of a higher intensity has been divided by that of lower intensity, to show the ratio of emission intensity. This technique demonstrates the relative changes between adjacent measurements to display and highlight areas with a higher relative increase at different points of increasing power. It is clear that not all regions on the sample respond in the same way to the change in power.

For an increase at low power, only the large clusters on the Al layer are seen to switch on first, with just a little background from the rest of the sample. To demonstrate this, the emission maps of adjacent emission intensities are divided. This is seen in Figure 4-8b-d, where the Z-scale represents the relative increase. Figure 4-8b is the result of the division of the PL map of the sample illuminated with 0.4µW by the map captured at 0.15µW. Likewise, Figure 4-8c is the division of the image captured with an incident power of 3.6µW by the image illuminated by 1.4µW. In this figure, more regions switch on, and there is a more significant difference between the Al substrate and the SiO_2.

The Z range of values for this figure is much wider: this is due to the different switch-on points at different areas on the sample surface, so areas such as the large clusters become very bright quickly, whereas the substrate with a uniform distribution of QDs is only just beginning to switch on. By the point of high excitation intensity, Figure 4-8d shows the 115/90µW image, where the image becomes a lot more uniform, as all areas across the sample saturate. This can be seen in the flattening of the range in Figure 4-8d.

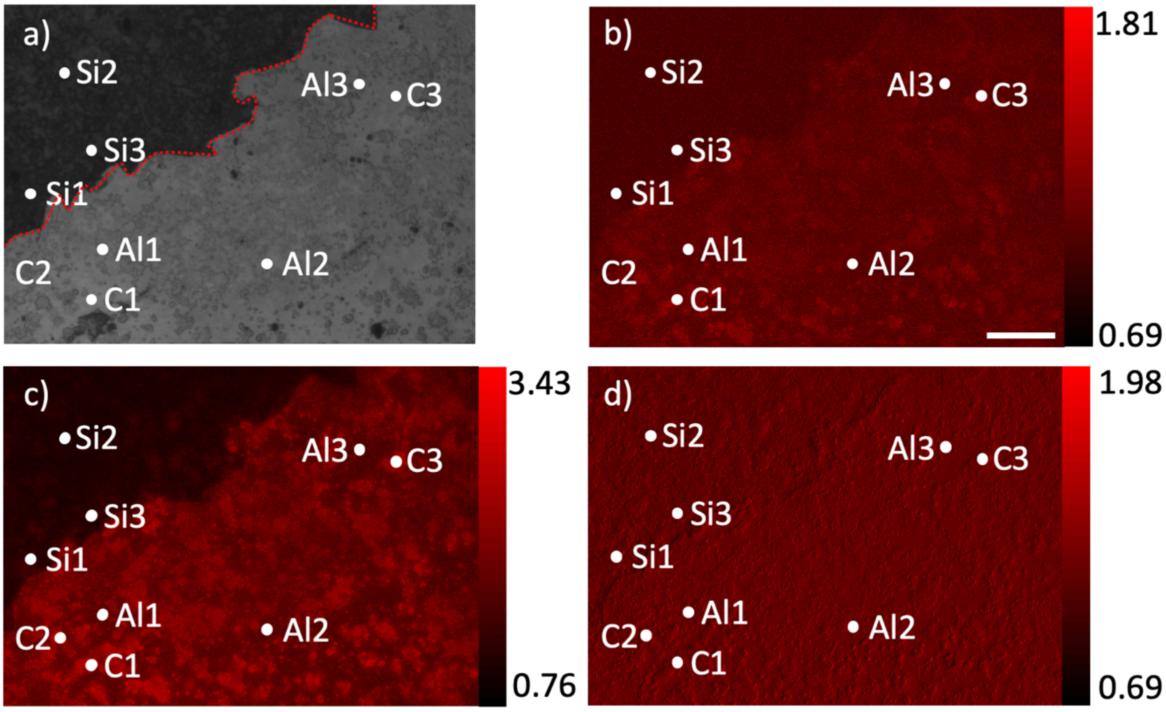

Figure 4-8: a) A white light image of the sample. b-d) shows divided images of the PL capture, to compare changes in gradient at different excitation powers: these are (b) 0.4/0.15µW, (c) 3.6/1.4µW and (d) 115/90µW, as shown in Figure 4-7. Scale bar represents 20µm. Z scale shows the relative difference in percentage increase across the sample. The greatest increase in gradient is in c, where most of the background QDs switch on. Figures reused under CC license. Red dotted line indicates region with Al substrate.

4.4.3 Whole-Sample Imaging

To further analyse and illustrate the variation in density of QDs across the sample surface, the percentage increase of emission intensity at different incident powers is calculated. Figure 4-9a shows for each pixel, at which incident intensity there is the greatest percentage increase. It is very clear that the large clusters on the substrate (in blue) have their greatest relative increase at around 0.36µW. The more uniform regions of the sample on both the bare SiO_2 and the Al have their greatest increase at the same point, at around 14.5µW, independent of substrate. Figure 4-9b demonstrates across the sample the points at which different regions ‘switch on’. To reduce the effects of noise in the processing, ‘switch-on’ is defined as when the measured intensity on the CCD is twice that of the background level, measured with no excitation intensity.

The background level is the ‘null’ measurement of the sample, taken when the sample was not illuminated. The earliest switch-on point is the largest clusters on the Al surface, which switch on between 0.15 and 0.36µW, followed by smaller clusters on the SiO_2 surface. This shows clearly the largest clusters have the earliest switch-on point, and more uniform areas on the surface require a higher incident intensity for their emission to become visible. These patterns start to reveal characteristics and properties of the sample which cannot be interpreted by the physical locations of the QDs alone (by a white light image, or a single PL map), and they originate from the random and unpredictable nature of the fabrication process, in addition to their interaction with the substrate. This behaviour becomes visible when subject to multiple challenges.

There is a clear boundary in required incident intensity for QD switch on, as demonstrated by the edge of the Al background. In Figure 4-9b, the majority of the image is covered by the large blue area, which follows the position of the Al substrate: the QDs on the reflective surface have a much lower switch-on threshold, due to the increase in effective incident power to the dots. However, this boundary does not feature in Figure 4-9a; the rate of increase in emission intensity is not impacted by the substrate in the same way and is heavily dependent on the local density of QDs. All regions where there is a uniform distribution of QDs have the same peak gradient: whilst the substrate will have a big impact on overall peak intensity, and how quickly their emission is visible, it does not affect the emission characteristics.

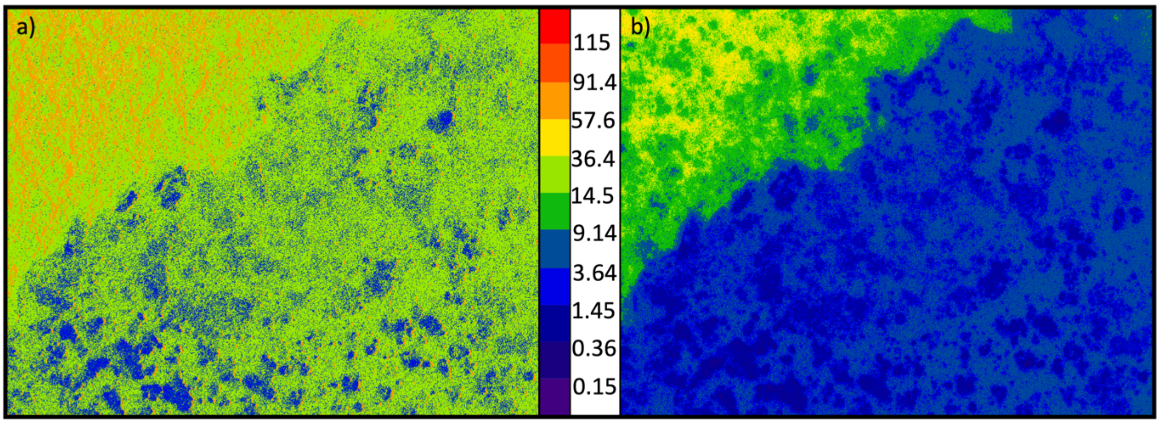

Figure 4-9: Variation in the emission properties across the QD sample. a) shows the excitation intensity at which there is the greatest relative increase in emission intensity. b) shows the 'switch-on' intensity at different regions across the sample, showing the largest clusters of QDs switch on first. The reflective substrate has a high impact on the point at which emission from the QDs is measurable. The colour scale indicates the incident power (µW) at which the optical effect occurs.

4.5 Plasmon-Induced Photoluminescence Intensity Hotspots

To characterise the emission properties of the samples with and without AuNPs, micro-PL measurements maps were taken at various regions, to observe the spatial variations in emission intensity and peak position. Figure 4-10 shows the PL spectra taken from across a 25x35um area of sample B, covering the same area as Figure 4-5d, showing the position of the plasmonic NPs. Factors such as the density of both AuNPs and QDs and their interaction change the overall emission properties. There is one very bright 'hotspot' which has an emission intensity of around 6x the emission intensity of the more uniform regions of the QD sample. A slight redshift of 15-20nm of the peak position for the PL emission of the plasmonic sample is observed, which could be caused by variations in the local dielectric constant, due to slight variations in the TiO_2 thickness: using e-beam evaporation for a metallic layer which is only a few nm thick is often not completely uniform[87-89]. Whilst the emission intensity units are arbitrary for each measurement, we can compare the range of intra-measurement emission intensities to obtain comparable measurements.

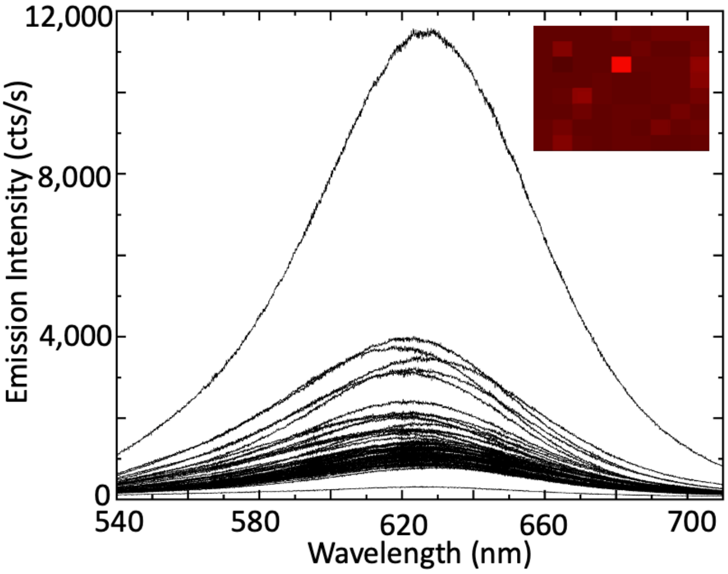

Figure 4-10: Each PL spectrum across a mapped area of plasmonic NP + QD sample showing variation in emission intensity, including one very bright 'hotspot', and several brighter areas. Inset: spatial map of part of the plasmonic sample, displaying spatial variation in emission intensity Lighter shades indicate brighter peak emission.

To compare quantitatively the emission from the control sample and plasmonic sample, Figure 4-11 shows a comparison of PL maps taken across areas of both samples. Figure 4-11a shows the average emission measured across both samples. On average, the emission intensity at the PL peak is around 1,500 counts/s, whereas the average emission intensity for the control sample is only 1,000 counts/s. Whilst this difference is relatively small on a macroscopic scale, Figure 4-11b/c demonstrates the important differences between the samples. Figure 4-11b shows one of the PL heatmaps taken across the plasmonic sample, where a brighter pixel indicates brighter emission. To compare the absolute differences between control and plasmonic samples, the z scale was normalised to the maximum emission intensity of the plasmonic sample, to highlight the much narrower range of emission intensities in the control sample. Whilst the plasmonic sample has a background emission higher than that of the control sample, this can be attributed to the impact of the reflective substrate. Whilst this substrate will not impact the interaction between AuNPs and QDs, it does increase the base level of emission (from the uniform areas, and regions with no AuNPs), making it easier to be measured by a conventional CMOS or CCD sensors.

From these measurements, we can demonstrate the dramatic increase in the overall dynamic range by comparing the standard deviation in their emission rate: the control sample, with a peak emission intensity at around 1,500 cts/s, had a standard deviation across all measurements of σ=260 cts/s. This is in comparison with the plasmonic device, which has a peak emission intensity of around 11,000 cts/s, and a standard deviation of σ=3360 cts/s. Not only is the overall emission of the sample brighter due to the reflective substrate, but the total range of emission values is also much wider. This creates a wider range of analogue values that are possible to be generated by the device, increasing the number of digitised CRPs possible. Due to the uniform and simultaneous QD deposition process, and with confirmation from AFM and optical microscopy, it is reasonable to attribute the bright spots and higher variation in emission intensity to the combination of the reflective substrate and plasmonic AuNPs. The control sample had only the deposited CQDs, and the plasmonic sample utilised the both a reflective substrate to increase the external QY, the plasmonic resonant nanoparticles, and the dielectric layer. Inter-QD interactions, such as from clustering of QDs on the surface may even lead to quenching of the PL emission[71,72].

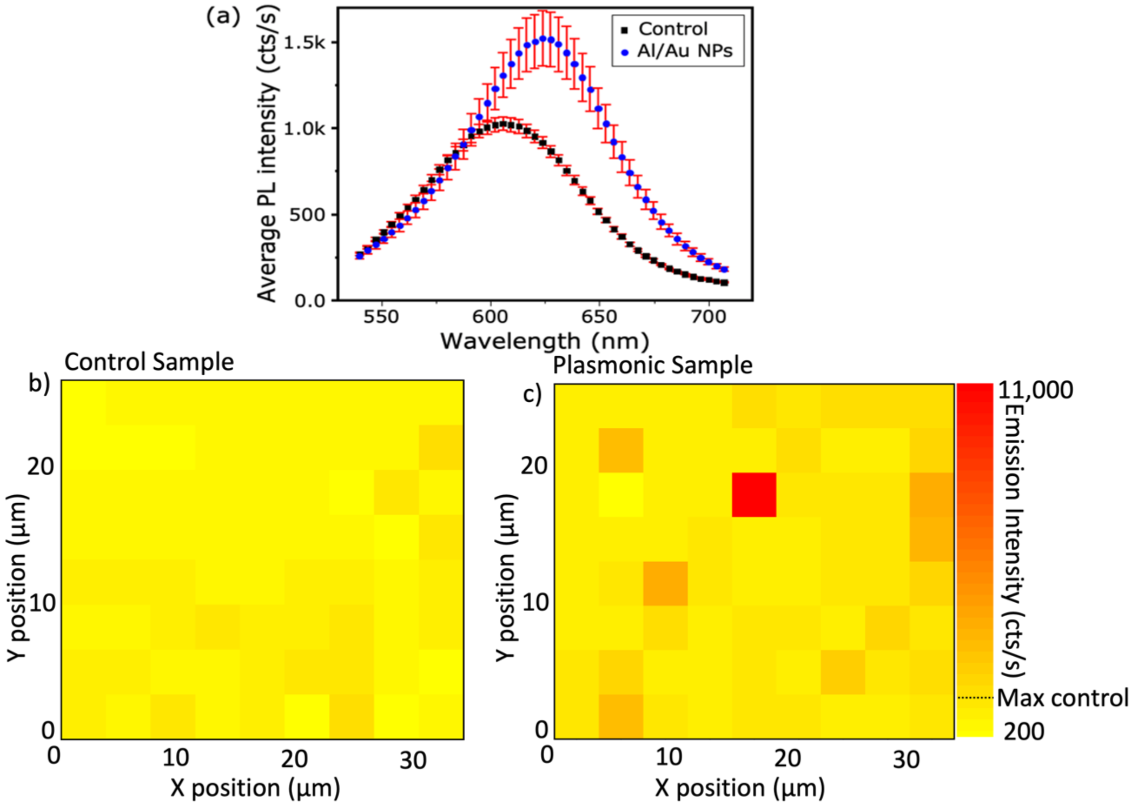

Figure 4-11: Comparison of PL emission intensity between plasmonic and control samples. a) shows the average PL spectra for both control and plasmonic samples. Used under CC-BY license. b) and c) PL maps of the plasmonic (b) and control (c) sample. The single very bright hotspot and several other hotspots can be seen, increasing significantly the dynamic range of emission, relative to the control sample. The maximum emission intensity of the control peak (1,150 cts/s) is labelled on the z scale, to demonstrate the increased range of emission from the sample with added AuNPs. a)

In this device, the nanoparticles have an impact on not only the intensity distribution of an array of NPs, but also the line shape of emission. For the applications of creating a PUF with a high dynamic range of emission intensity, any additional source of variation in emission intensity, including QD density and dielectric thickness adds to the unpredictability of the sample's emission properties.

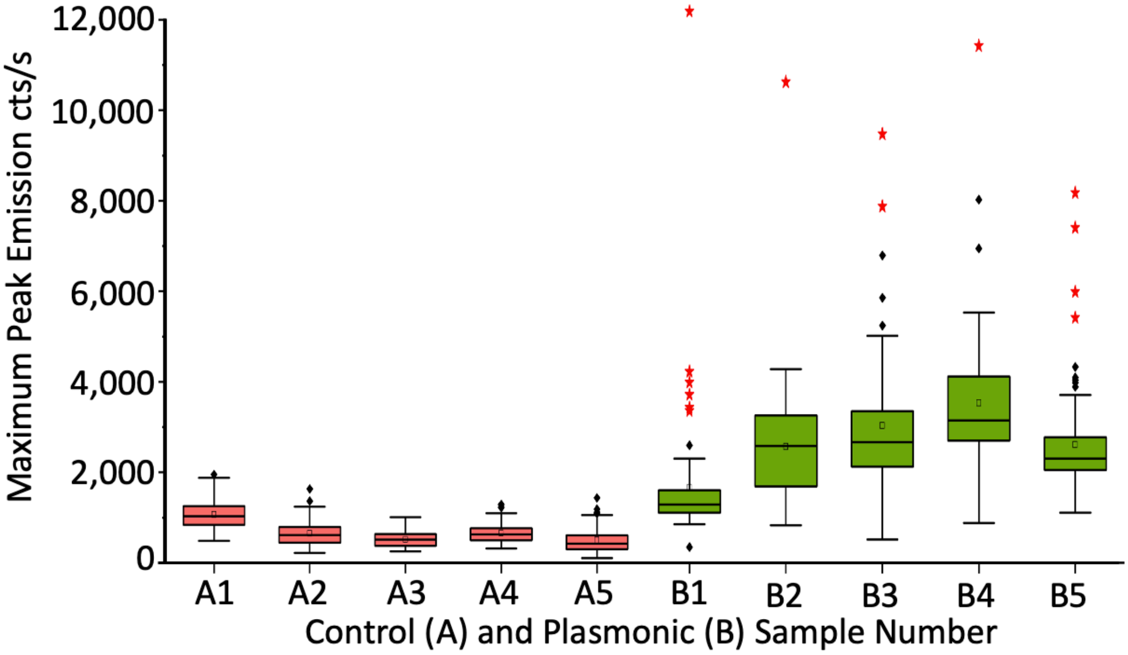

Figure 4-12: Boxplot displaying the distribution of the maximum peak intensity of the PL from 5 measured areas on the two different samples. Sample A (control sample) shows a narrower distribution of maximum emission intensity values compared with sample B. Outlier values are marked in black, and extreme values are marked as red stars, which are only present on the plasmonic samples, are attributed to the presence of AuNPs.

Quantitative analysis of the maps taken over the samples was used to obtain useful information about the emission characteristics and differences between the samples with and without plasmonic NPs. Figure 4-12 shows a boxplot of the emission intensities, showing the overall distribution of 5 maps taken over different areas on both types of sample each. The plot shows the peak emission intensity at each point on a 35x25um map. The boxplot details the upper and lower quartiles, and the whiskers indicate 1.5xIQR (inter-quartile range). Outliers, which are outside this range, are marked in black, and the extreme values, which have a maximum peak emission of greater than 3xIQR, are labelled with a red star. It is clear that the much wider range of emission values arises from the plasmonic sample. The mean values for the plasmonic sample (2643cts/s) are much higher than that of the control sample (648cts/s). With the addition of solely an Al reflective back layer, the expected peak emission counts are 2x higher, due to the >90% reflectivity of the incident, and emitted light back towards the QDs and CCD, but the increased average emission intensity and significantly increased range of emission values can be attributed to the addition of the plasmonic AuNPs[90]. Even with a widened IQR, which arises predominantly from the increased EQY due to the aluminium layer, there are several extreme values across the 5 maps, and none in the control

]

samples, suggesting modifications in the external emission behaviour, created by the addition of the AuNPs. The distribution about the mean for both control and plasmonic samples are displayed in Figure 4-13. This demonstrates that the extreme values are further from the normal distribution, and more prevalent in the plasmonic sample. The range of emission values in the control sample arises from a non-uniform density distribution of QDs on the sample surface. The QDs were deposited using electro spray ionisation, so the clustering of QDs on the surface explored earlier will contribute to a range of emission intensities.

To further demonstrate this increased range of emission generated by the combination of the Au plasmonic nanoparticles and the aluminium substrate, histograms of their peak emission counts are shown in Figure 4-13. The plasmonic sample has a much broader normal distribution, with the addition of several outlier peaks, up to an order of magnitude higher than the peak of the mean emission intensities. These outlier peaks are not exhibited on the control samples.

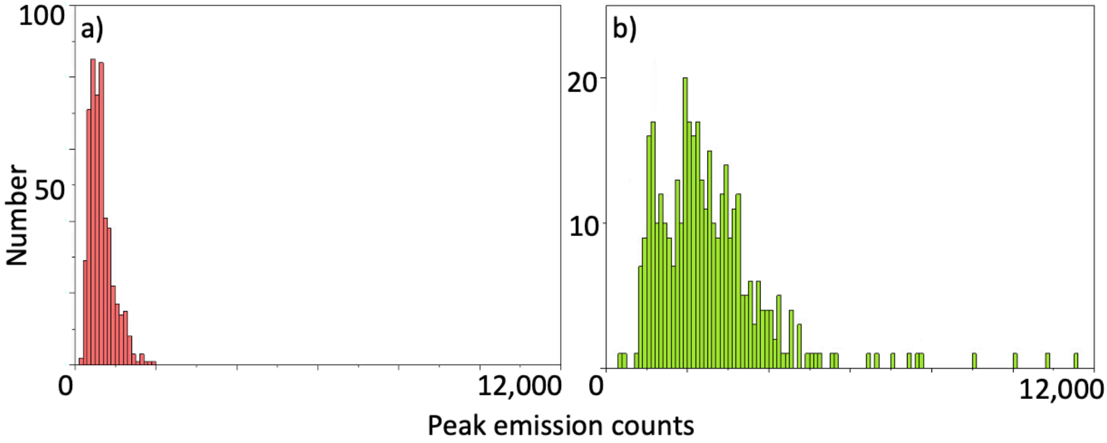

Figure 4-13 Histograms of the counts of each peak emission intensity value across maps of the control (a) and plasmonic (b) samples. The reflective aluminium substrate alongside local electromagnetic field variations from the AuNPs generates both a wider distribution and several outliers.

4.6 Conclusions

This chapter introduced a small and simple modification to improve an existing type of optical nanoparticle PUF. Whilst there is much discussion in the literature of different methods to authenticate this category of PUF, far-field optical methods are unquestionably one of the most practical techniques, requiring little to no additional equipment, such as filters or lenses.

By characterising the intrinsic behaviour of the excitonic states within the QDs, and how they interact with each other and their substrate, we have added a new dimension of security for this type of PUF. A simple characterisation technique is utilised, using far-field macro-photoluminescence, which, whilst the spatial resolution is lower than other techniques, is much more scalable and faster than alternative methods of constellation-style O-PUF interrogation.

The key property of constellation-style nanoparticle O-PUFs is the implicit security which originates from the unpredictable fabrication methods. This work has demonstrated an improvement to its unclonability by measuring additional properties of the QDs, including the linearity of the response, the position and width of the histogram peaks, and their position-dependent switch-on points. This introduces several new layers of authentication, without complex additional measurements, therefore increasing the total number of potential CRPs this device can store. This type of optical measurement increases the level of security of these devices, without additional hardware requirements as are commonly required for these types of PUF.

To further improve these devices' levels of security, there are other intrinsic properties of QDs that could be tested, such as blinking. This is a property that will be considered in more detail in Chapter 5. Blinking is a common phenomenon in QDs where their emission fluctuates irregularly, originating from the formation of long-lived dark excitons in the dots[91-94]. The macro-PL measurements used to characterise the O-PUFs in this chapter will measure the average emission of a region of QDs on the sample, therefore the small variations in emission brightness of individual dots are not observable using this method. However, with a sensitive and higher-resolution measurement technique, this effect could be used as another check to verify the PUF's authenticity, alongside all other techniques, to verify the presence of quantum dots.

Subsequently, the absolute emission intensity of regions on the tag as a security device was explored with a modification to the QD O-PUF fabrication method is developed, to create strong spatially dependent emission intensity variation. The device's structure is primarily made from the deposition of colloidal quantum dots, but deposited on a reflective layer of Al, with a random distribution of AuNPs. These plasmonic nanoparticles couple with the InP/ZnS QDs, modifying the PL intensity of the QDs locally. The combination of the QDs positioned amongst the AuNP distribution, with the highly reflective layer of Al, leads to the creation of randomly positioned 'hotspots' on the surface, a much larger dynamic range of emission peaks, and increased peak intensity, generating a greater number of CRPs. It was found that the addition of AuNPs to the QD samples increases the standard deviation of emission intensity from σ=260cts/s to σ=3360cts/s, demonstrating a significantly increased dynamic range of emission intensity values. This, therefore, increases the potential number of CRPs available to be stored within the same size tag, improving a key figure-of-merit for all PUFs by increasing the bit density of the device and making them easier to read. Additionally, the reflective properties of the Al coating increases the total external quantum efficiency of the device to improve this PUF's evaluability, creating the potential for these devices to be characterised by less sensitive measurement techniques.

Whilst this technique for fabricating and characterisation of an NP PUF has a key security advantage over the position and linearity-dependent PUF introduced earlier, this study required a higher-resolution measurement to characterise the 'hotspots', because they are so localised. Additionally, due to the mechanism of the plasmonic NPs enhancing the local electric field, the PL is only enhanced effectively when excited resonantly, by the emission of the QD. Due to the weaker coupling between QD and AuNP than a resonant interaction with a coherent excitation source would produce, macro-PL measurements will be less effective at strongly generating oscillations of plasmons to enhance the emission locally of the sample. Macro-PL uses a wide band of excitation spectra, so whilst an even wider range of PL emission intensities is theoretically possible with a plasmonic nanoparticle chosen to match the excitation laser, this would require the same light source for characterisation. This type of AuNP-enhanced O-PUF has a balance between increased dynamic range of emission values, and therefore increased entropy and bit-density, and simplified evaluability.

This chapter has shown incremental improvements to quantum dot-based O-PUFs, in both measurement technique and the overall bit density of a device by increasing the number of CRPs it can hold, with the addition of plasmonic nanoparticles.

Chapter 5

Local Modification of Monolayer Transition Metal Dichalcogenide Photoluminescence

This chapter combines the technique introduced in the previous chapter of modifying local emission of quantum emitters with plasmonic nanoparticles with the use of 2D materials to create a modification to the quantum dot physical unclonable function (QD-PUF). Here, the decoration of a silicon substrate with gold plasmonic nanoparticles is proposed to modify locally the emission properties of a transferred optical 2D material, to increase both the dynamic range of emission intensity due to the optical plasmonic enhancement, and the overall line shape and emission peak position from induced local defects and strain. It is hypothesised that due to the strong electromagnetic interactions of gold nanoparticles (AuNPs) at specific frequencies, they can locally alter the electromagnetic properties of the 2D materials.

2D materials are advantageous for quantum O-PUF applications for their low cost and more attractive material choice due to lower toxicity and increased sustainability[95]. Additionally, optical 2D materials, including transition metal dichalcogenides (TMDCs) such as MoS_2 and WS_2, as used in this work, are highly sensitive to localised defects, including strain or atomic defects, such as vacancies[77,96]. The dependence of optical 2D materials is detailed further in Chapter 2.2.5.7, but it is these properties and advantages that makes them exciting candidates for the next-generation quantum O-PUFs. However, for this application, monolayer TMDCs have some weaknesses, including a relatively low quantum yield, and high uniformity from mechanically exfoliated flakes[97-99]. Existing O-PUFs have utilised fundamental properties of optically emitting 2D materials, including their layer number-dependent band structure, and their sensitivity to defects as the source of entropy. This work builds on these designs and adds a new explicit source of randomness.

Room-temperature photoluminescence maps of control and plasmonic samples of WS_2 were performed to observe the spatial variation in emission intensity for samples with and without AuNPs. Subsequently, Raman maps, atomic force microscopy, and low-temperature PL measurements were performed on the same samples to investigate the origin of the observed properties, to verify the interaction of the 2DM with the AuNPs.

5.1 Introduction

In Chapter 4, the fabrication and characterisation of O-PUFs consisting of an array of quantum dots on a surface was introduced. This detailed their properties where their nonlinear optical response, or local modifications to the emission properties were stimulated through the addition of plasmonic AuNPs to the sample surface. Whilst QDs are advantageous for this application, colloidal QDs are expensive to manufacture, so these types of PUF are difficult to fabricate by scalable means without prohibitive cost. This chapter instead investigates monolayer WS_2 as a bright, direct-gap semiconductor as a potential alternative emitting material to develop an O-PUF without QDs.

Transition metal dichalcogenides (TMDCs) have potential in the field of quantum O-PUFs, due to their direct band gap, when a single layer, and the potential for lower fabrication costs than QDs[100]. As discussed in Chapter 3, due to their complex, layer-dependent band structure, different single-layer TMDCs vary in overall quantum yield. Therefore, some TMDCs will have some advantages over others. For example, whilst MoS_2 is attractive in this field due to its longevity and stability, its quantum yield is relatively low, making it more difficult to characterise by conventional optical methods[101,102]. WS_2 has a higher quantum yield, so it is easier to measure with conventional CCDs. Mechanically exfoliated flakes have a relatively uniform spatial emission, due to their relatively higher uniformity and purity, over other exfoliation techniques, such as liquid phase exfoliation (LPE) and chemical vapour deposition (CVD)[103,104]. However, the optical properties of 2D materials are strongly influenced by localised defects, such as vacancies, substitutions, or strain, which can arise during the micromechanical transfer process[105]. This chapter will explore some of these properties to investigate 2D materials as a feasible quantum O-PUF, when additional defects are induced with plasmonic nanoparticles.

Quantum dots typically are made from rare-earth elements, such as cadmium, which are highly toxic, and potentially carcinogenic, therefore alternatives are sought after, such as the InP/ZnS QDs used in Chapter 4. These alternatives are less toxic than typical cadmium-based QDs, but still use rare-earth elements, which may suffer from geopolitical conflict or low recycling rates, such as indium[106].

However, naturally occurring van der Waals crystals are a less expensive and common source of direct-gap semiconductor: due to their weakly-interacting layers, powder MoS_2 is very commonly used as an inexpensive industrial lubricant, so layers of 2D TMDCs are becoming easier and less expensive to fabricate than colloidal QDs[107-110]. This makes optically active 2D materials a natural next step for the development of O-PUFs, using quantum materials.

5.2 Sample Fabrication and Characterisation

To observe the effect of the addition of AuNPs to the 2D material, a control sample was fabricated simultaneously alongside the plasmonic samples. An optimised concentration of 100nm AuNPs was drop-cast onto clean Si/SiO_2 substrates, as discussed in Chapter 4. 100nm NPs were chosen for their broad plasmonic resonance peak, which overlaps with the sharp PL absorption peak of ML WS_2, such that the emission from the WS_2 resonates with the plasmonic oscillations. The concentration of AuNPs solution was optimised, such that the density on the surface was relatively low, around 0.5/μm^2. This ensured a monolayer flake of WS_2 which is on the order of 10s of μm^2, will have a few discrete NPs beneath the flake. This allowed for the observation of any effects caused by individual particles. A small gap between very closely spaced plasmonic particles can generate a significantly enhanced electromagnetic field when excited resonantly, known as gap plasmons. This effect, whilst it would be beneficial for increasing the overall QY from a 2DM, would not create the same degree of spatial variation compared with individual nanoparticles under the surface[111]. To uniformly increase the emission response of a 2D crystal, optical nanocavities can be fabricated as substrates, to enhance the overall light outcoupling across the flake[112]. A thin dielectric was deposited using Atomic Layer Deposition (ALD) on top of the AuNPs to remove the nonradiative recombination channel between an optically active semiconductor and a metallic surface. 5nm of Al_2O_3 deposition was determined to be close to the optimal thickness for these samples, for the greatest relative increase in emission intensity. Before this work started, the use of an ALD system became available for the project, which enabled a more controlled deposition technique of a dielectric to be deposited, so is advantageous over the oxidation of a thin metallic film used in Chapter 4.

Single layers of WS_2 were mechanically exfoliated from a bulk crystal. This method enables large-area flakes to be obtained, with a relatively high QY, where they can be individually manipulated and positioned. A WS_2 crystal was exfoliated as described in Chapter 3.1 using blue Nitto tape onto a PDMS stamp, creating several monolayer flakes simultaneously, which were used for both the control and plasmonic sample, to minimise significant variation between flakes from different batches of exfoliation. The control sample and the plasmonic sample were both fabricated by transferring these flakes to the substrates with/without AuNPs. Mechanical exfoliation of flakes onto a PDMS substrate allows for careful identification and precise manipulation, so they can be transferred to any specific position on a substrate. As exfoliated, these flakes have high uniformity, and a lower defect density than other methods, so they have a higher quantum yield than flakes fabricated with CVD, for example. Individual single-layer flakes were identified using optical microscopy, Raman spectroscopy, and macro-PL, before they were transferred onto the prepared substrates. Figure 5-1 shows a schematic of the plasmonic sample fabrication. As with the plasmonic samples fabricated in Chapter 4, there will be a shadowing effect created, where the dielectric is not deposited underneath the NP. A choice was made to transfer the 2D monolayers onto the AuNP substrate, due to the practicality of the fabrication technique: the crystals are small (>50µm^2) relative to the size of the substrate, so it is unlikely that the desired distribution of AuNPs on the surface would be achieved. If this method were to be extended using 2D material fabrication techniques which create much larger areas of 2D crystal (such as LPE or CVD), deposition of the plasmonic NPs onto the 2D film would remove the effects of strain on the TMDC crystal.

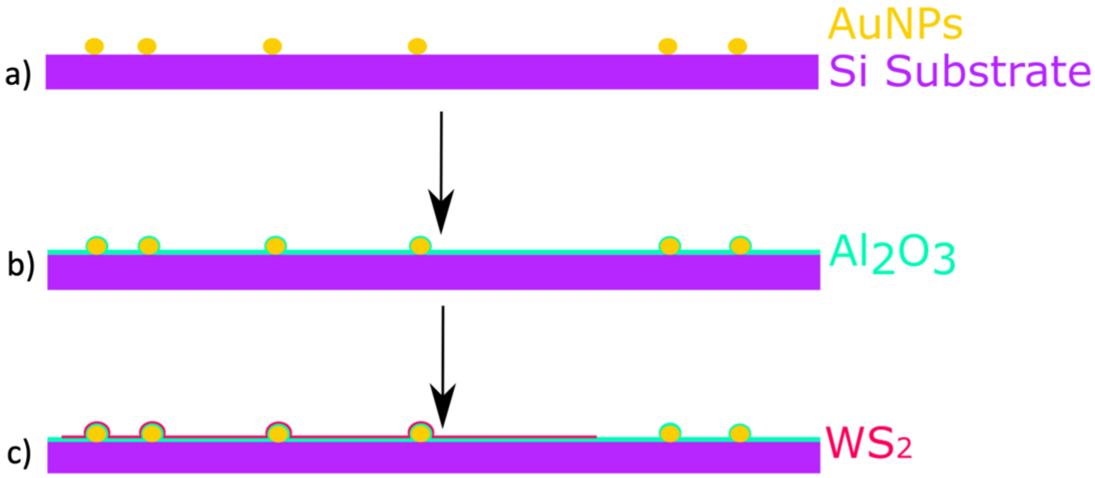

Figure 5-1: Fabrication schematic of Au+2DM samples. a) A dilute solution of 100nm AuNPs (gold) in ethanol is drop-cast onto a clean Si substrate (purple). b) A 5nm layer of Al_2O_3 dielectric (blue) is deposited as a separator, onto the substrate. c) A monolayer of WS_2 (red) is transferred onto the prepared substrate.

5.2.1 Liquid-Phase 2D Exfoliation

To investigate the ability to make large areas of optical devices made from 2D materials, liquid-phase exfoliation of MoS_2 was explored. Liquid-phase exfoliation of 2D-materials for optically emitting 2D inks was performed using a high-frequency sonication technique, using both bath-sonication and probe sonication techniques.

MoS_2 powder was obtained from both ACS nanomaterials and Sigma Aldrich for the inks fabricated in this study. The solvent used during LPE sonication of 2D materials is required to be carefully chosen: the surface tension of the solvent must carefully match the energy of the inter-layer bonds of the specific 2D crystal to be effective. For MoS_2, as investigated in this study, two different solutions were used: a 70:30 IPA:H_2O mixture was used, and n-methyl pyrrolidone. Both solutions match the inter-layer energy of MoS_2 crystals, and have been extensively studied in LPE of this vdW semiconductor.

Initially, materials were exfoliated using a 280W sonic bath, using a 1mg ml^{-1} solution of MoS_2 in a 70:30 IPA:H_2O solution for 1 hour. Continuous sonication of a solvent for (up to) several hours generates a lot of heat within the bath, so the water was continuously replaced using a water aspirator to keep the system cool, with a constant bath volume.

Whilst this process was designed to reduce the thickness of the crystals within the solution, naturally variation in finalised crystal thicknesses occur. To isolate the crystals with fewer layers, and remove the thicker ones, the resulting solution underwent a series of centrifugation steps.

The solution was transferred from the sonication vessel into small centrifuge Eppendorf tubes, and centrifuged initially for 45’ at 500 rpm. This step is to remove the largest, thickest crystals within the solution. These crystals are the heaviest, so after centrifugation they form a dense pellet at the bottom of the tube, where the remaining solution was carefully removed with a narrow-gauge Hamilton syringe. This process was repeated increasing centrifuge speeds up to 22,000g, until only the lightest flakes remained. The change in ink after removing increasingly light flakes is shown in Figure 5-2. This cascade centrifuge technique is designed to isolate the single-layer flakes of 2D material[113].

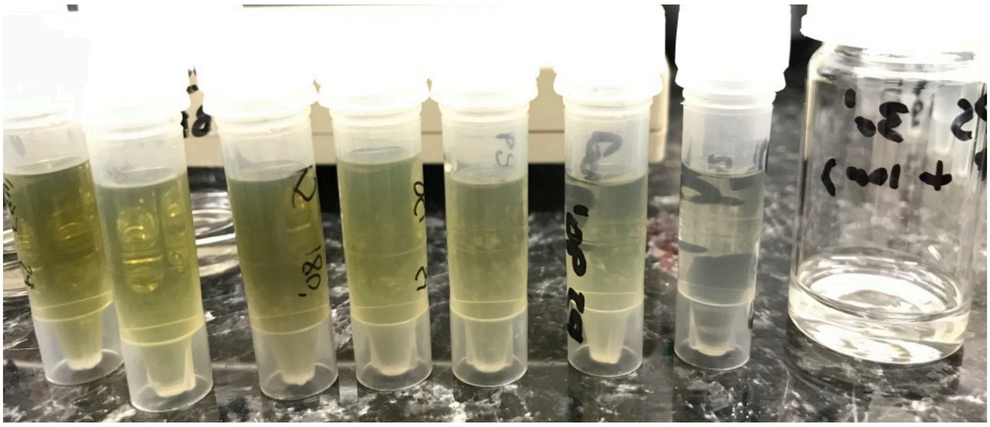

Figure 5-2: MoS_2 inks after bath sonication and several cascade centrifugation steps. The ink after the slowest centrifuge speed (500g) is on the left, and speeds are progressively faster, up to 22,000g on the right.

The change in absorption of each of the solutions, as determined by the absorption properties of different thicknesses of the semiconductor, are shown in Figure 5-3**.** As the thicker flakes are removed, the darker material is removed, leaving a yellow solution, which should only contain the lightest flakes (which are, in principle, the thinnest). Only at the lowest centrifuge speeds, the absorption peaks of the MoS_2 A and B transitions are visible, which would suggest the removal of too much material at higher centrifuge speeds. Absorbance spectra for centrifugation at different speeds is shown in Figure 5-3. Additionally, the exfoliation parameters of the inks must be tuned: a sonication power too low will not successfully exfoliate the layers of the crystals, but if the power is too high, this risks damaging the crystals, essentially making nanoparticles, which will significantly affect their optical properties by confining the charge carriers spatially.

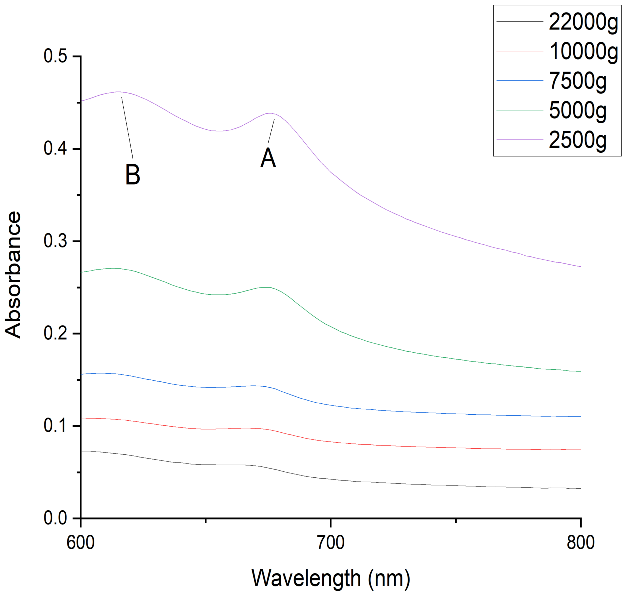

Figure 5-3 Absorbance spectra of MoS_2 which has been bath sonicated, after several cascade centrifugation steps, showing both the A and B absorption peaks disappear with high centrifugation speeds.

5.2.2 Optical and Atomic Force Microscopy

Optical bright and dark field microscopy enabled both confirmation of single-layer WS_2 on the sample surface, and the presence of resonant plasmonic nanoparticles underneath the flake. Figure 5-4a shows an optical image bright-field (BF) of the control sample, with a flake of $WS_{2,}$ transferred onto the SiO_2 + Al_2O_3 substrate. Point 'C' marked on the image is the point from which the individual PL spectra were measured. Figure 5-4 b shows the dark-field image, demonstrating no scattering from AuNPs under the flake. Figure 5-4c/d show the plasmonic sample, in BF (c) and dark field (DF) (d) image, where P1 and P2 are the point measurements taken: P1 corresponds to the measurements directly on the AuNPs, where P2 corresponds to measurements taken on the plasmonic sample, around 2µm away from the AuNPs. The AuNPs can be clearly seen in the DF image underneath the 2D flake. The samples fabricated in this chapter involved the deposition of the 2D TMDC flake on top of a distribution of AuNPs. This naturally induces several external factors, including cracks and strain. This order of device fabrication was chosen because of the relatively small flake size – it is impractical to deposit the NPs onto the crystals, and obtain the required distribution of NPs. In the future, this work could be repeated with larger areas of 2D crystal, from CVD flakes.

To verify the nanoparticles were under the surface of the plasmonic sample, dark-field optical microscopy and PeakForce atomic force microscopy (AFM) were utilised. In dark-field imaging, the nanoparticles fluoresce strongly, so they are seen clearly beneath the 2DM in Figure 5-4d.

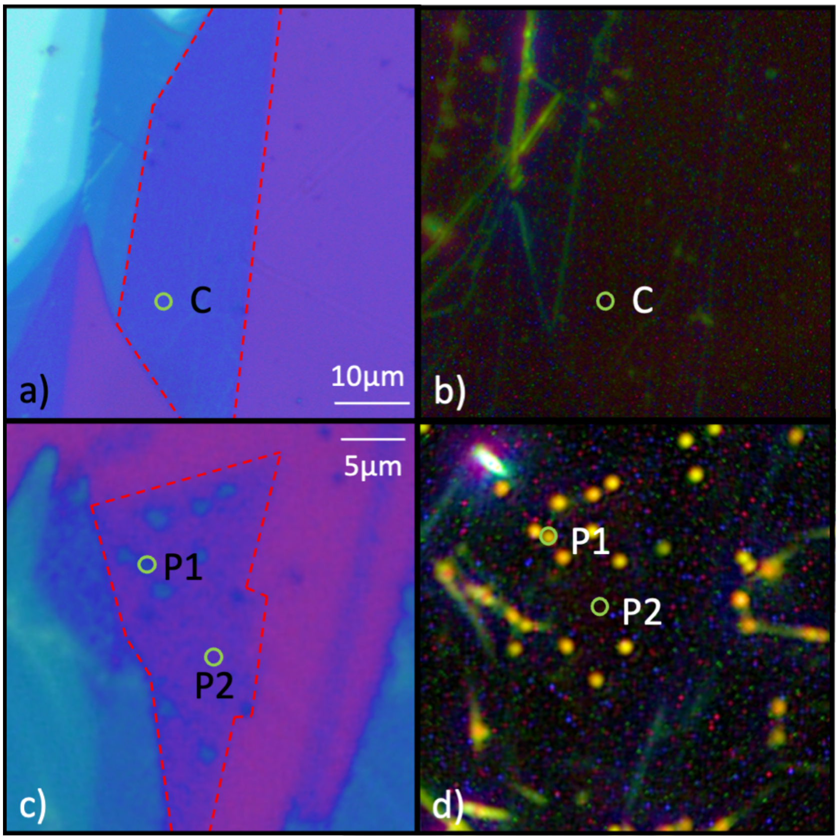

Figure 5-4: a) Optical bright-field b) and dark-field images of the control sample c) shows the bright-field and d) dark-field images of the plasmonic sample. Points C, P1, and P2 show the points on each sample where individual measurements were taken during initial characterisation. Red dotted line on a,c indicate regions of monolayer.

To observe the physical properties of the flakes, quantitative nanomechanical mapping (QNM) ‘PeakForce’ AFM was conducted on both samples. This technique images both the topography of the surface, so ripples and bubbles can be seen, but also the underlying nanomechanical features of the sample. The bubbles and ripples which form during polymer-based 2D transfer are visible in both samples, with very large structures formed near the 100nm AuNPs. The information from the QNM AFM can then be used to correlate optical properties with the physical and nanomechanical properties of the flakes in the next section. Using QNM, the spatial variation in DMT modulus of the sample can be extracted. The DMT model (named after Derjaguin, Muller, and Toropov) is a model of extracting the Young’s modulus of a surface during AFM. It is linearly related to the force on the tip during retraction in QNM by:

$$\mathrm{F_{tip}} = \frac{4}{3}\mathrm{E^{*}}\sqrt{\mathrm{Rd^{3}}} + \mathrm{F_{adh}} \tag{5-1}$$

where F_{tip} is the force exerted on the tip, R is the tip radius, d is the tip-sample separation, F_{adh} is the adhesion force, and E^* is the reduced Young’s modulus[114], which, when calibrated with a material of known Young’s modulus, enables determination of the Young’s modulus of the sample. This scale allows for the extraction of some of the nanomechanical properties of the supported and suspended flakes.

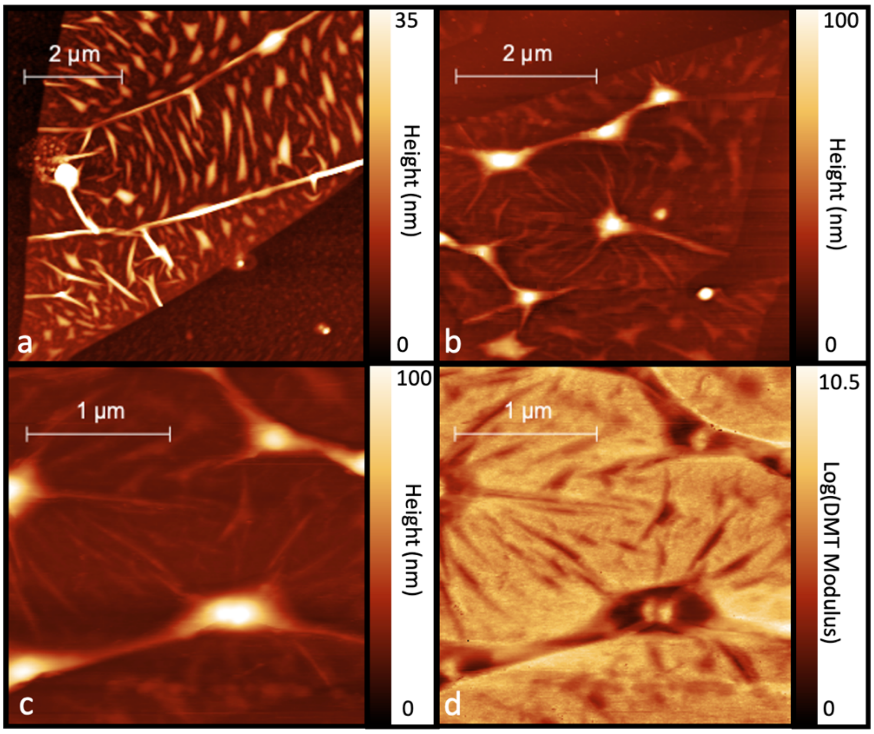

Figure 5-5: AFM/PeakForce QNM images of plasmonic and control samples. a) shows a topographical image of the control sample, showing small bubbles and folds across the sample. b) shows a topographical image of the plasmonic sample, showing the large 'tent-like' bubbles, caused by the stretching of the flake over the AuNPs. c) shows a zoomed-in topographical image of AuNPs under the flake. Small ripples where the 2DM is under strain are visible. d) shows the DMT modulus of image c), obtained using PeakForce QNM: Darker areas in the image are more compliant, and lighter areas are stiffer.

5.3 Optical Measurements

5.3.1 Photoluminescence Maps

High-resolution room-temperature photoluminescence maps of both control and plasmonic samples were taken with a 532nm CW DPSS laser, to compare both absolute emission intensity differences between the samples, and across each sample. Figure 5-6 shows PL maps with the absolute emission intensity of each sample, with 1µm steps. Figure 5-6a shows a map of the peak emission intensity measured at each point across the control sample, and Figure 5-6b shows the peak emission over the plasmonic sample. The peak absolute intensity in the plasmonic sample is around 2x greater than that of the control sample, from 18,000 cts vs 9,000 cts, for the brightest area of each flake.

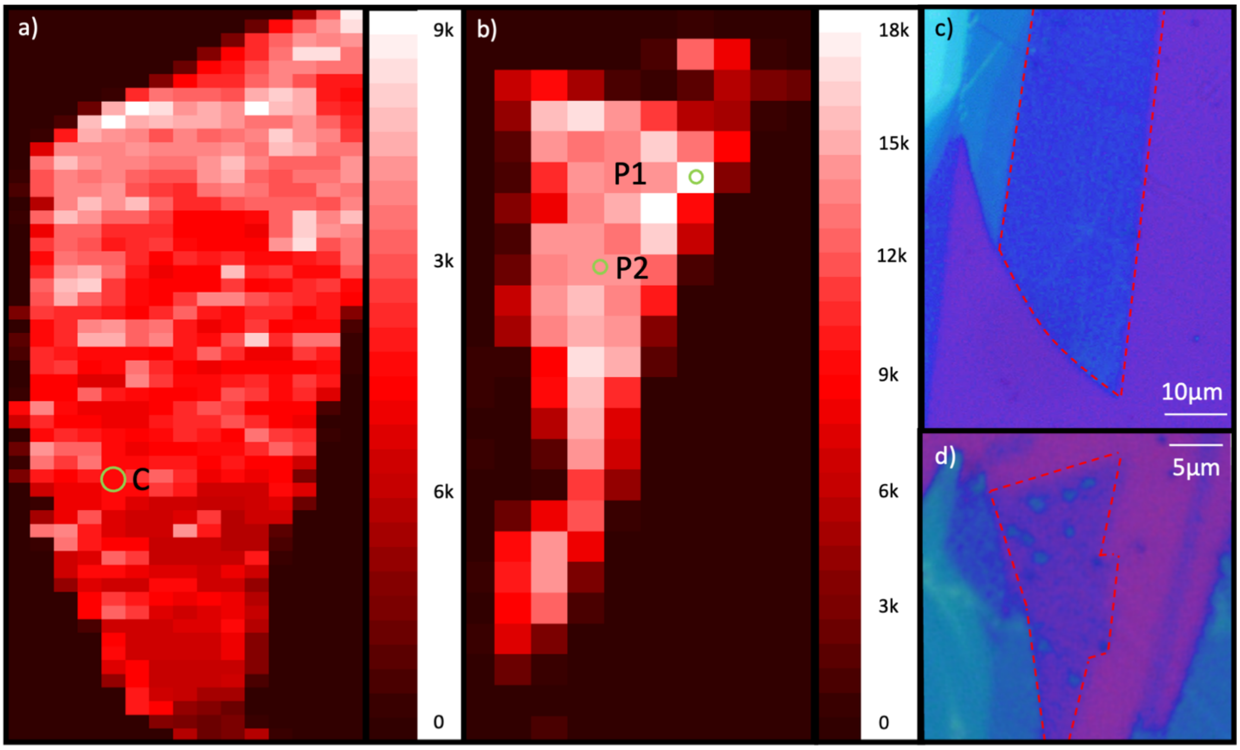

Figure 5-6: Shows PL maps across control a) and plasmonic sample b). The plasmonic sample exhibits a much wider range of emission values. c) A bright-field optical microscope image of the control sample. d) A bright-field optical microscope image of the plasmonic sample.

There is some spatial variation in the peak emission of the control sample, which appears to correlate with specific physical features across the sample, including folds and bubbles. A natural consequence of the polymer-based dry transfer mechanism is that bubbles and ripples are formed as the 2D material on the flexible substrate is pressed onto the sample surface. This results in the suspended flakes exhibiting different emission properties than the regions of flake in good contact with the substrate. This can be aided somewhat by carefully controlling the speed, pressure applied, and temperature during transfer, but bubbles, folds and some organic contamination is often uncontrollable. The control sample was transferred directly onto an SiO_2 substrate, with minimised surface defects, so the bubbling/rippling formed was relatively uniform and consistent across the flake. However, due to the large AuNPs on the plasmonic surface, large, long bubbles were formed, as the crystal is deposited around the AuNPs.

The plasmonic sample shows some hotspots in four locations across the flake, which are attributed to the interaction with the AuNPs under the flake. To correlate the optical and the physical/nanomechanical properties of the 2D materials, PeakForce QNM images of both samples were taken, as can be seen in Figure 5-5c/d. Figure 5-5c shows the topography AFM image of the control sample, showing a reasonably uniform flake, with several bubbles across the surface. The sample with the plasmonic nanoparticles underneath the surface, displayed very large 'tent-like' structures, where the 2D flake is suspended on top of the AuNPs. This creates very large areas where the flake is suspended above the substrate, with a very small contact area between the AuNP and the 2D material at the centre. Figure 5-5c shows a small-area topographical scan of one of these regions. Figure 5-5d shows the DMT modulus of this area, extracted from the PeakForce QNM, where the lighter areas are stiffer, with darker areas representing more compliant regions of the flake. This shows the 2D material itself is relatively stiff, but the compliant areas are the unsupported areas of the flake around the AuNP. There is a stiff region (similar DMT modulus to the WS_2 on SiO_2) in the very centre of the 'tent', where it is supported by the AuNP, and very compliant areas around it, where the flake is unsupported. This induces strain in the flake, relative to the regions which are flat to the substrate. Figure 5-7 shows the average PL emission from across the emitting regions of the flake. The range of emission values for the plasmonic sample is much higher than for the control sample.

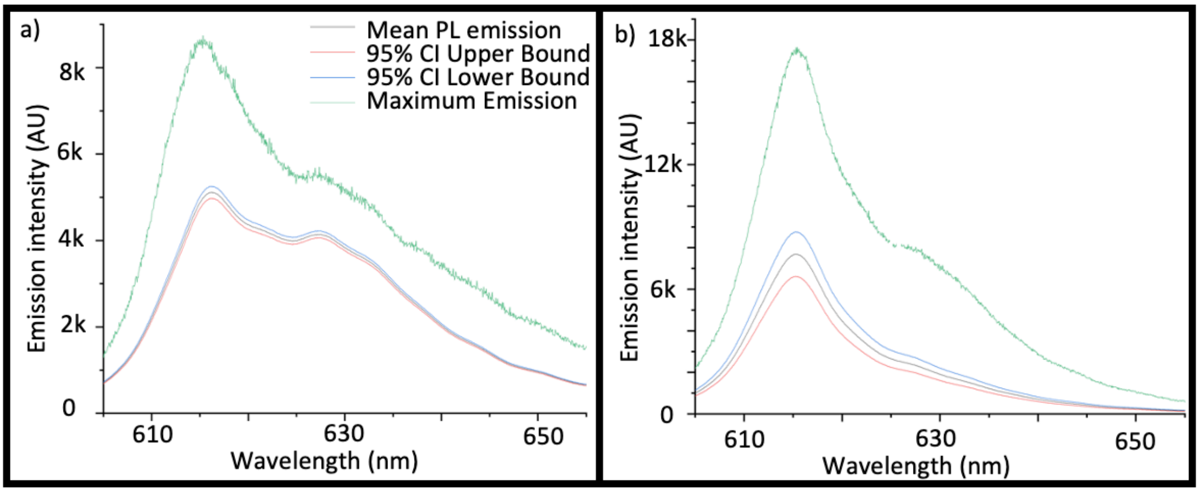

Figure 5-7: The mean emission values for a) control sample and b) plasmonic sample. There is a wider confidence interval for the plasmonic sample due to the increased range of potential emission values caused by the addition of the plasmonic nanoparticles.

To help deconvolute the effects of strain induced by the deposition of the 2D crystal, and doping or plasmonic effects, deposition of silica nanospheres onto the same Si+SiO_2 substrates was investigated.

These nanoparticles were used as-purchased from nanoComposix. Drop-casting of the silica nanospheres created high density regions of aggregation, so spin coating was investigated. 10µl of the solution was spin-coated onto the clean substrates. Even with variation in the spin speed from 1000 to 5000 rpm for 60", this technique did not produce a good surface distribution of the SNS. This technique generated very large clusters of nanoparticles on the surface, but with very few individual particles between. The best regions with individually separated particles are generally very close to large clusters of several hundred nanoparticles, which inhibits the transfer of 2D crystals.

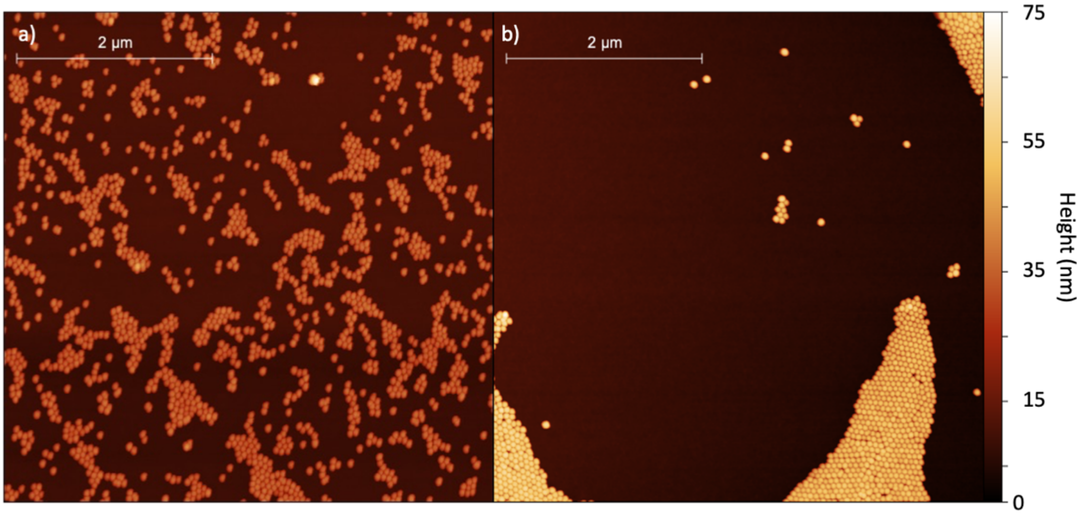

Figure 5-8: AFM images of 50nm SiO_2 nanospheres on an Si+SiO_2 substrate. The nanoparticles naturally cluster together, leaving very few individual particles. a) 1000rpm b) 5000rpm spin speeds.

Further work is subsequently required to investigate deposition methods of these silica NPs. The large areas of high-density NPs which cover the surface using these techniques are not suitable for the facile transfer of large micromechanically exfoliated 2D crystals.

5.3.2 Raman Measurements

Raman measurements of both plasmonic and control samples were taken to investigate the physical differences between the samples. There are two key peaks of interest in the Raman spectra: the in-plane (E^1_{2G}) and out-of-plane (A_{1G}) modes, which are shown in Figure 5-9a. These Raman modes are highly sensitive to local induced defects: the A_{1G} and E^1_{2G} peaks are sensitive to doping and strain respectively[115,116]. Multiple Lorentzian peaks were fitted to the Raman spectra for positions P1, P2 and C. The Raman spectra from both samples were compared to investigate whether the presence of the individual AuNPs impacted the doping or strain between samples. Figure 5-9b shows the Raman spectra of the E^1_{2G} peak at P2 with a peak intensity at 358.0cm^{-1}, whereas the E^1_{2G} peak of the plasmonic P1 sample was 357.2cm^{-1}, indicating increased relative strain on the flake at P1. A third resonance, the 2LA(M) (longitudinal acoustic) mode is a second-order Raman peak, which overlaps with the E^1_{2G} peak. This peak arises not from the optical phonon modes, but from the movements of the atoms in the lattice[115,117,118]. This peak, which has a higher intensity than the E^1_{2G} peak, is the result of the periodic compression and expansion of the lattice, along a specific direction: the M refers to the specific direction and magnitude of the phonon: they occur at the M point in the Brillouin zone[118].

Because the A_{1G} peak is sensitive to local doping, it can be used to determine whether or not the local doping of the sample changes across the flake. There is a relative blue-shift in the A_{1G} peak at the site of the NP, which is suggestive of a relative p-doping of the flake at the NP site[115,119].

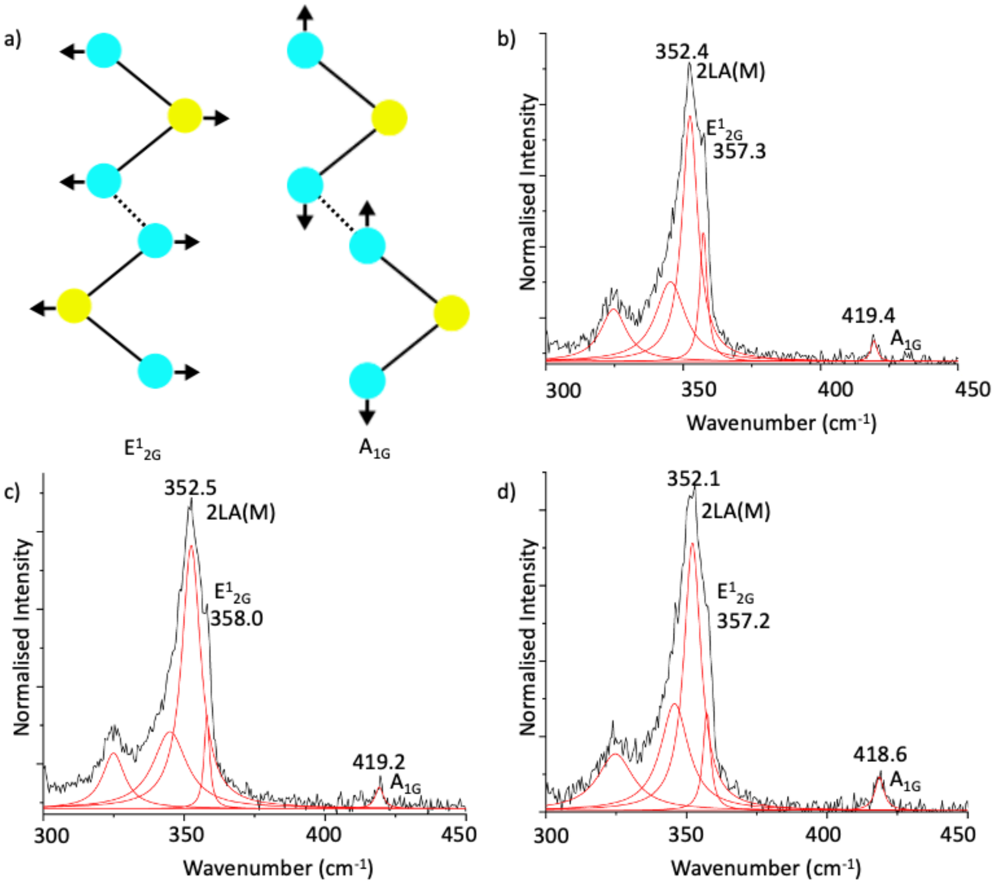

Figure 5-9: a) Shows the origin of the key vibrational Raman modes of WS_2. A_{1G} is the out-of-plane mode, and the E^1_{2G} peak is the in-plane mode. b-d) Shows the Raman spectra with Lorentz fitting for b) control sample c) P2 plasmonic sample and d) P1 plasmonic sample.

5.3.3 Low Temperature Photoluminescence

Individual PL measurements from the points on the control and the plasmonic sample at low temperatures were taken to observe features that cannot be resolved at room temperature, so the samples were cooled in an AttoCube dry cryostat to 5K. Reducing the sample temperature removes the effects of phonon scattering observed at higher temperatures, so peak widths narrow, and individual peaks can be resolved. Figure 5-10 shows measurements from individual points on both samples. The control sample measured at point C (labelled on Figure 5-6) shows characteristics as would be expected of temperature-dependent PL measurements of as-exfoliated WS_2. Conversely, the power-dependent measurements of the plasmonic sample measured at P1, where there is the densest region of AuNPs, and the brightest hotspot, displayed several sharp peaks, instead of a single sharp peak.

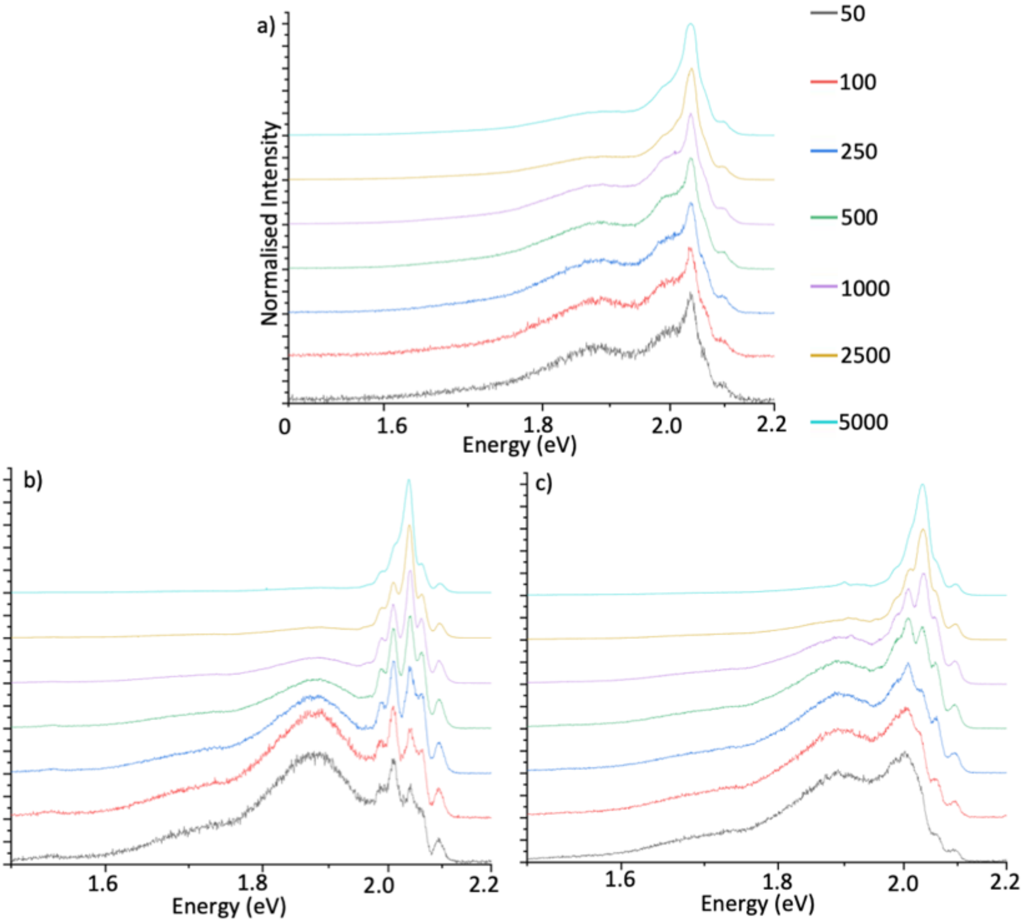

Figure 5-10: Normalised 5K power-dependent measurements of both control sample C (a), and plasmonic sample (b,c). b) A region on the plasmonic sample 2µm away from the nanoparticles (P2), and c) The spectra taken directly on top of the AuNPs (P1). The excitation powers are measured in nW.

Observed in both control and plasmonic samples are the peaks associated with the neutral exciton peak (X) at 590nm (2.1eV), and the charged exciton (trion, X^-) peak, at 600nm (2.05eV). The evolution of the PL spectra of WS_2 with respect to sample thickness is covered in more detail in Section 2.2.5.7. The neutral exciton peak arises from charge-carrier recombination when electrons raised to the CB from the illumination source relax across the direct bandgap, as shown in Figure 2-10. The trion peak is also strong at room and low temperatures. A trion is a three-body quasiparticle, constituted of two like-charged charge carriers, and one carrying opposite charge. They are more commonly observed in low-dimensional optical semiconductors due to their increased binding energy[120,121]. At room temperature, and in the control sample, the dominant peaks in the PL spectra are the exciton and trion peaks, as shown in Figure 2-10. WS_2 flakes which have been micro mechanically exfoliated using this method with a polymer stamp are naturally n-type doped, resulting in the charged exciton (X^-), which will involve the recombination of two electrons and a hole[122]. In CVD WS_2, the trion peak is not observed in the monolayer, so the observation of this peak can be attributed to global doping across the flake during the mechanical exfoliation and transfer technique.

The sharp peaks which resolve at low powers in the plasmonic sample, shown in Figure 5-10b/c, are known as 'low-energy' peaks, L_1-L_4. At low temperatures, with a low excitation power, these peaks are observed, but as the incident power and sample temperature increase, these peaks rapidly quench[123]. This effect is observed in the plasmonic sample strongly, at both P1, directly at the site of an AuNP, and P2, slightly away from the NPs, but peaks L_1-L_4 are not observed in the control sample. The origin of these sharp low energy lines is not fully understood, but they have been attributed to localised defects or indirect exciton recombination[124]. As discussed earlier, the plasmonic sample exhibits very large and tall bubbles in the 2D layer, relative to the thickness of the flake, which creates large areas of the sample under strain. One explanation for the observation of these low-energy peaks is, due to the presence of relatively large particles on the substrate, more localised defects have been induced in the sample, which could lead to the generation of the low-energy peaks from the energy traps which are created. This makes these peaks prominent when the sample is at a low temperature and with a low relative incident power. The strong exciton and trion states which are still visible in the control sample is suggestive that these are free states, but the L lines are strongly localised, and directly related to defect-bound excitons and biexcitons in the sample[120]. These peaks are also observed at P2, which is suggestive that, although the spectrum is from a region that is around 2µm from the NPs, the defects induced from the AuNPs have influence beyond the physical extent of the 100nm particle.

5.4 Manufacturing Weaknesses and Shortcomings

To investigate the repeatability of the measurements and the hotspots, further plasmonic samples (labelled A and B), were fabricated alongside the primary plasmonic sample with 5nm of ALD-deposited Al_2O_3 layer between the sample and the 100nm AuNPs. Two of these samples are shown in Figure 5-11, where similar hotspots were observed on these samples which correlate with the position of the AuNPs.

However, it is notable that on sample B, in addition to spots that have a brighter emission, the flake is much more uniform overall than the original plasmonic sample. Additionally, there are several ‘cold spots’ that correlate to the position of larger clusters of AuNPs under the surface. These spots are likely to be caused by the efficient non-radiative recombination channel, with electrons instead recombining through the AuNPs, due to an uneven thickness of the dielectric medium. However, this method in reducing locally the PL emission does still increase the overall dynamic range of the emission intensity.

These variations could be attributed to inconsistency in thickness of the dielectric layer, due to the nature of this type of thin film deposition, so the AuNPs are too close or far away from the WS_2 layer, causing quenching, or a weaker coupling between the NP and the 2DM. Additionally, large folds are created by the AuNPs on the surface. A stronger enhancement of the local electric field could be obtained by modifying the size of the nanoparticles such that the SPR overlaps not with the emission peak of the WS_2, but with the energy of the excitation source, in this case, the laser, but this introduces limitations on measurement techniques available.

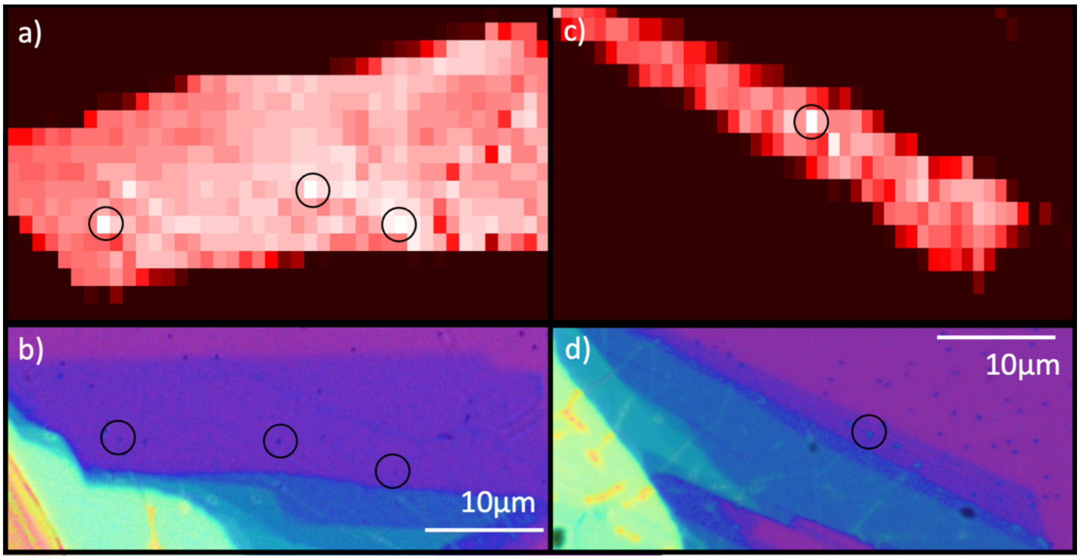

Figure 5-11 Additional WS_2 flakes on Al_2O_3 with 100nm AuNPs, demonstrating the repeatability of the experiment. a,c PL peak intensity maps. Several hotspots (labelled) which correlate with the position of the nanoparticles can be seen. b) Optical microscope image of sample c. d) Optical microscope image of sample b.. In sample a, some ‘cold spots’ which correlate to larger clusters of AuNPs can be observed, which may be attributed to quenching of emission.

A sample with 7.5nm Al2O3 and a layer of WS2 was fabricated, which is shown in Figure 5-12. This thickness of dielectric is too thick, such that it screens the effect of the enhanced electric field from the AuNPs. Further work should be completed to optimise fully the dielectric thickness.

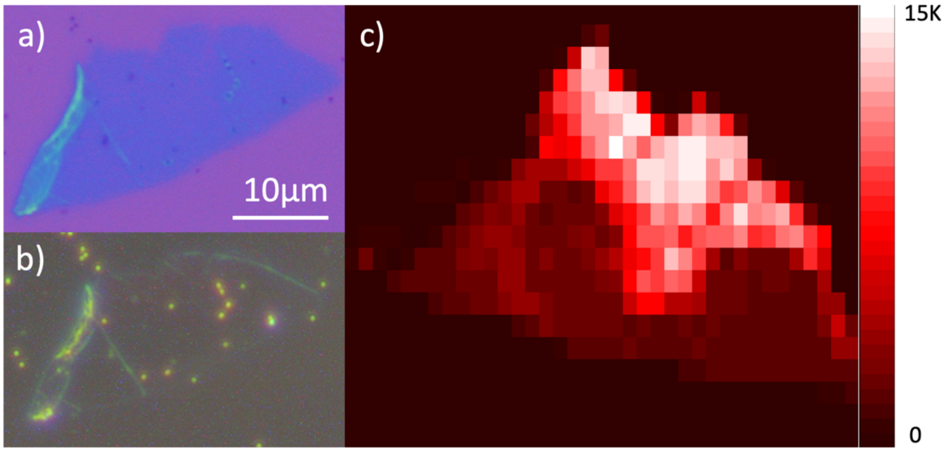

Figure 5-12 Sample of WS_2 with 7.5nm Al_2O_3. A) Optical bright field image, b) Optical dark field image, c) Peak emission intensity (cts/s) from PL map.

5.4.1 Liquid-Phase Exfoliation of 2D Crystals

To characterise these 2D liquid-phase exfoliated solutions, atomic force microscopy (AFM), Raman, and micro-photoluminescence techniques were used. A drop (10µl) of the final 2D solution was drop-cast onto a clean Si+SiO_2 substrate and left in ambient conditions to dry.

Optical and AFM images shown in Figure 5-13, show what appear to be flakes of MoS_2 on the surface, and whilst not a single-layer thick, their physical size and Raman spectroscopy suggests they are MoS_2, because they match the powder size used.

Raman spectroscopy across the samples indicated the presence of Mos_2 in the exfoliated inks, but did not indicate the presence of single, or few-layer flakes. Monolayer MoS_2 has a well-defined separation of the A_{1G} and E^1_{2G} peaks of 19cm^{-1} [35], and as the number of layers increases, this separation of Raman peaks increases, to around 24.5cm^{-1} for bulk MoS_2[125]. For these samples of MoS_2, a range of peak separation was observed, across the substrates, but most had a separation of around 23.5cm^{-1} indicating only few-layer to bulk crystals were obtained using this technique.

Micro-photoluminescence was used to determine the emission properties, if any, of the exfoliated flakes. No PL was observed from the samples which were drop-cast onto an SiO_2 substrate. It was hypothesised that the drying process of the drop-cast solutions on the surface was causing the flakes to form large clusters, which may reduce any PL. PL in solution was investigated, both with micro-PL of the post-centrifuged ink on a concave glass slide, and with a custom-built macro-PL setup. Unfortunately, neither of these techniques generated any observable PL from the inks. This may be solved by exfoliating with the same technique for a longer period of time, but more work needs to be completed to optimise this process.

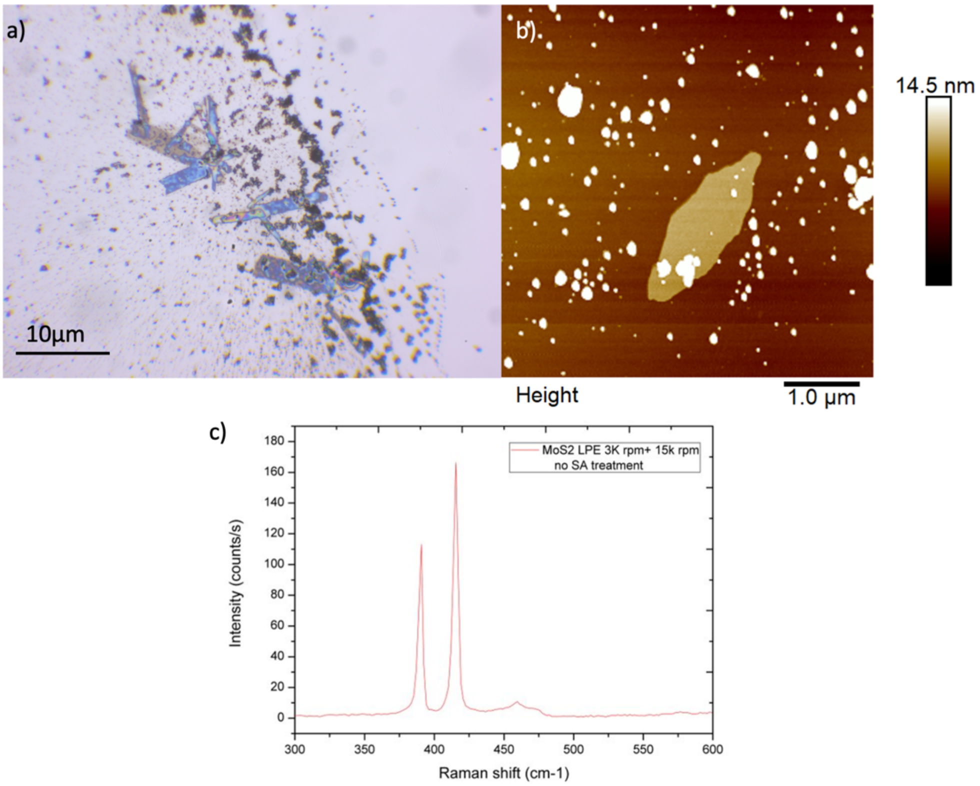

Figure 5-13 Liquid-phase exfoliated 2D flakes. a) Optical image of ink deposited on SiO_2 substrate. b) AFM image of a multi-layer MoS_2 flake. c) Raman spectra of the MoS_2 ink showing a peak separation of 23.5cm^{-1}.

There is a threshold of energy of the system which must be met for the exfoliation to be successful: if the energy generated during sonication is not enough to overcome the vdW bonds between the crystal layers, exfoliation for any time will never be sufficient to effectively separate the crystals.

Conversely, a powerful exfoliation technique, especially for the 150W sonic probe may damage any crystals within the solution. If the spatial area of the crystals is reduced, charge charrier confinement in the x-y plane will start to modify the exciton binding energies, blue-shifting their emission wavelength.

Another consideration is the excitation wavelength-dependence of the emission of the resulting 2D ink. It has been shown in literature that 2D inks exfoliated using this technique can have a strong dependence on their emission intensity on the excitation wavelength, whilst in solution.

5.4.2 2D Vertical Heterostructures

To investigate the potential for 2D material devices as quantum O-PUFs, the vertical stacking into vertical heterostructures (VHS) was explored. The addition of one or more stacked layers of optical 2D materials gives the potential for an increased number of challenge-response pairs (CRPs) by modifying their emission properties, both with emission peaks from more than one emitting material, and the potential for inter-layer excitonic features. Van der Waals crystals are attractive for stacked heterostructures, due to their weak inter-layer bonds, enabling the facile stacking of semiconductors, with less consideration for lattice matching[126].

The stacking technique for these materials is fundamentally the same as for a single-transferred layer onto a substrate, using a PDMS pick-up stamp technique. Due to the behaviours of the PDMS, as discussed earlier in this chapter, this enables the deposition of a second 2D flake onto a previously transferred crystal. Figure 5-14 shows a small 2D vertical heterostructure of $MoSe_2$ on top of a layer of WSe_2 on an Si+SiO_2 substrate. As discussed in Chapter 3**,** the transfer process using the PDMS stamp induced several defects into the 2D crystals, including, organic compounds, which arise from the PDMS stamp, and from the environment. Alternative stacking arrangements were attempted, including Wse_2 capped with a MoS_2 monolayer. Optical and AFM images of a Wse_2 + $MoSe_2$ VHS on SiO_2 can be seen in Figure 5-14a/b.

Raman spectroscopy and PL was performed on the sample, where the expected Raman peaks for both Wse_2 and $MoSe_2$ could be seen using both optical techniques, but no inter-layer features, such as inter-layer excitonic peaks, were observed.

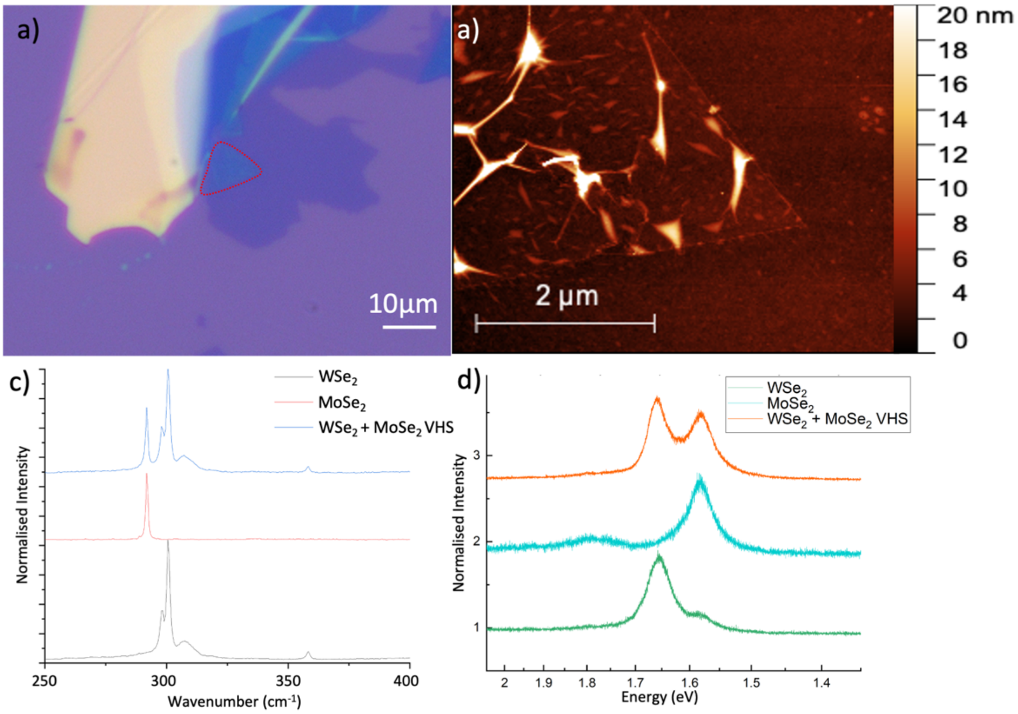

Figure 5-14 a) $MoSe_2$ + Wse_2 mechanically stacked vertical heterostructure on Si+SiO_2 The Wse_2 monolayer is marked with the red line. B) AFM image of vertical heterostructure, c) Raman spectra of $MoSe_2$ + Wse_2 d) PL spectra of $MoSe_2$ + Wse_2 mechanically stacked vertical heterostructure on SiO_2.

A sample of Wse_2 capped with a monolayer of MoS_2 on HOPG was fabricated, where the PL peak for Wse_2 was much brighter than that of MoS_2, so the MoS_2 emission peak, and any potential inter-layer peaks, were not observed. It is likely the MoS_2 emission was also quenched, from being in direct contact with the HOPG. This sample and it's PL spectra is shown in Figure 5-15.

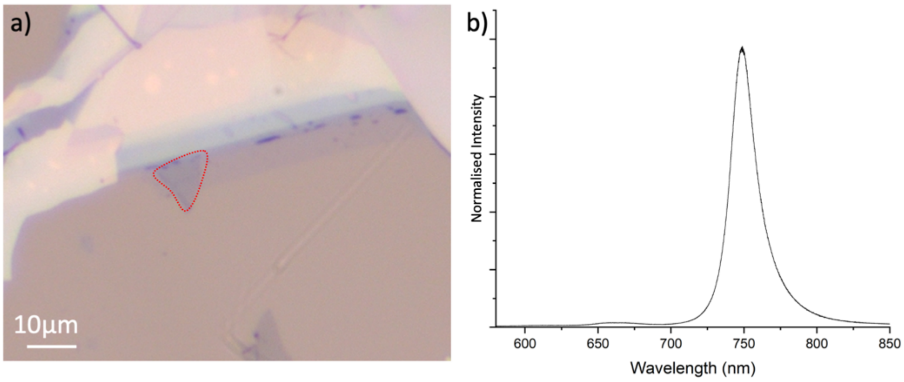

Figure 5-15 a) Optical microscope image of MoS_2 monolayer (marked) on top of Wse_2 monolayer. b) Measured PL from this sample.

To obtain a high-quality 2D VHS, the fabrication procedures and conditions should be optimised and improved: the fabrication conditions require a clean, environment (such as a glovebox), in addition to the ability to carefully control the crystal angle.

Because of these strict requirements for effective inter-layer excitonic features to be exhibited, they are not observed in these samples fabricated. The features usually exhibited by the single-layer TMDCs used are present, but the weak coupling between the deposited layers in these samples means more work is required to obtain a higher quality 2D VHS.

5.5 Conclusions

In this chapter, the spatial modification of a monolayer WS_2 flake with the addition of plasmonic nanoparticles, separated by a dielectric layer of Al_2O_3, has been demonstrated. The overall dynamic range of emission values is increased with localised hotspots on the surface, alongside a change in line shape through the induction of local defects to the flake.

These hotspots can be used not only to increase the overall dynamic range of emission intensity values across a sample but also the line shape and peak position. The samples with physical defects introduced from the electromagnetic interactions with the individual AuNPs leads to the generation of defect-mediated low-energy peaks, which are not observed in pristine crystals of ML WS_2. The next stage of development of this tag is the optimisation of nanoparticle size and dielectric thickness to obtain peak coupling between plasmonic resonance frequency and 2D material emission frequency. Whilst some work was undertaken to deconvolute the different effects which caused the change in optical behaviour of the samples, including Raman measurements and power-dependent low-temperature PL, further investigations need to be taken to fully understand the 2D material's behaviour.

Further work should be undertaken to optimise the best nanoparticle-2DM separation: 5nm of ALD Al_2O_3 was the optimal coupling determined from the material obtained in the time available: only 2 thicknesses of Al_2O_3 were characterised, and the peak coupling between plasmonic nanoparticle and emitter is very sensitive to dielectric thickness[50].

For this type of O-PUF to be scalable in the future, techniques to fabricate 2DM+plasmonic nanoparticle samples must enable the fabrication of larger, bright areas of 2D material. Reliable methods of creating larger areas of 2D materials include chemical vapour deposition (CVD), or atomic layer deposition (ALD) where precursors are injected as a vapour into a furnace, where they react under controlled conditions to form islands of 2D materials on a substrate[98,127,128]. Whilst faster and more scalable than micromechanical exfoliation, it is an expensive method. An alternative technique is liquid phase exfoliation. This technique was demonstrated here, but requires more work to produce reliable, brightly emitting inks. The creation of 2D inks which are capable of being printed gives the potential for a large surface area coverage of emitting 2D materials. On a large scale, these techniques provide a much more efficient method to create large areas of optically active 2D semiconductors.

To be more scalable for an effective O-PUF, not only does the fabrication method, but also the type of characterisation, need to be simplified. The work in this chapter primarily focussed on characterisation techniques using laboratory instruments. Subsequent modifications and improvements of this design would involve macroscopic measurements, as described in Chapter 3. With effective LPE, areas covered by light-emitting 2D materials can be large enough to be characterised with macroscopic techniques, such as macro-PL, including simpler characterisation methods, such as with a smartphone camera system. Whilst WS_2 has a relatively high QY, relative to other 2D TMDCs, additional modifications can be made to improve their overall external QE[129]. A common technique used to improve the overall brightness of sulphur-based 2D TMDCs is the treatment of the materials with superacid[130-132]. This treatment can increase the overall QY of the flakes to almost unity. The mechanism behind this improvement is not fully understood, but it is thought to be related to the passivation or repairing of sulphur vacancies (V_S) in the 2D flake.

Whilst the addition of AuNPs to the substrate onto which ML optical 2DMs are transferred induces new optical effects, including brighter ‘hotspots’ and other localised defects which change the photoluminescence line shape, these effects are not easily characterised without advanced techniques. With a powerful broad-band light source and a sensitive enough detector, there is the potential for this design of 2D material-based O-PUF to be effectively characterised with macro-PL.

Here, a promising potential modification to the emission properties of 2D WS_2 is demonstrated, to increase the feasibility of this classification of material to be used for O-PUFs, but they still require some further improvements in characterisation technique and optimisation of PL-nanoparticle interactions.

Chapter 6

Conclusions and Future Work

6.1 Conclusions

The works described in this thesis aimed to demonstrate fundamental improvements to optical physical unclonable functions (O-PUFs). The O-PUFs described in these works were based on the properties of low-dimensional semiconductors, namely quantum dots (QDs) and 2D materials, and their interactions with light and plasmonic nanoparticles. Investigations were undertaken to improve this classification of O-PUF by adding both an additional set of linearity measurements to an existing classification of O-PUF. Subsequent modification of these nanomaterial-based O-PUFs was made with metallic nanoparticles, or optical 2D materials. These modifications have improved the device's security, material cost, fabrication scalability, and material sustainability.

Fundamentally, the security of each of the three O-PUFs described in this work arises from the implicit unpredictability and uncontrollability in the fabrication mechanism of the devices, in addition to the explicit addition of metallic nanoparticles to modify their emission characteristics. These three modifications aim to develop some of the key figures of merit applicable for all PUFs, which are used as the benchmark for improvements made in each design.

The first step in improving quantum O-PUF figures of merit was to consider improvements to the existing 'constellation-style' QD O-PUFs discussed in literature. Whilst many existing O-PUFs of this type satisfy the requirement of PUFs to be unique from uncontrollable randomness in the fabrication process, improvements can be made to reduce the likelihood of counterfeiting, such as from a replay attack. This QD-PUF is similar in construction to other optical nanoparticle PUFs, but the modification in measurement introduced here improves its robustness against this type of attack. Optically active quantum dots have known emission characteristics in response to the excitation. The random deposition process of the colloidal QDs onto a partially reflective surface naturally creates a nonuniform and anisotropic distribution of emitters, with an unpredictable spatial distribution and random densities of QDs. The change in density of QDs across the surface ensures both the overall emission intensity and emission response characteristics is intrinsically random across the surface at the point of fabrication: clusters of QDs respond differently to a uniform film, due to both their local density and the charge carrier exchange between the QDs, which can reduce their recombination lifetimes.

Crucially, the QDs emission response is nonlinear, from a linear excitation source. The emission from the neutral exciton saturates when the incident power reaches a threshold: this behaviour makes the tag more difficult to replicate by adding a second layer of authentication. For a nefarious party to replicate the O-PUF, an attacker would not only have to replicate the physical position of the emitters, but also their brightness and emission rate as a function of incident power. This nonlinearity check simply confirms whether or not there are indeed quantum emitters on the surface of the tag.

To further improve this design, the second PUF modification investigated in this work was the addition of plasmonic gold nanoparticles (AuNPs) to the surface. These AuNPs were selected so their plasmonic resonance peak overlaps with the absorption and emission peak of the emitting QDs. This enabled the coupling of the excitons with the plasmons in the AuNPs, to further modify the emission properties of the O-PUF.

Conventionally, position-based (‘constellation-type’) O-PUFs have only a single type of measurement (i.e., the spatial position of the nanoparticles) which confirms the identity and authenticity of the tag. However, this modification to QD O-PUF design, which, because it is made from optically emitting quantum materials, the relative emission intensity of regions of the tag are used as an additional set of challenge-response pairs (CRPs) for the PUF’s authentication. We observed an increase in the mean emission intensity of 3x and an increase in peak emission value from 1500cts/s in the control sample to over 11,000cts/s in the plasmonic sample. This led to an increase in the standard deviation of emission values from σ=260 cts/s to σ=3360 cts/s. The coupling between plasmons in the AuNPs and the excitons in the QDs is very sensitive to several factors, including spacing between AuNP and QD, AuNP size, and AuNP density. Because of this, we see a highly increased dynamic range of emission values across the plasmonic device, relative to QD tags with no nanoparticles. This increased dynamic range of emission values, therefore, creates a much larger pool of potential CRPs available when initially characterising the device. The uncontrollable factors in fabrication, including dielectric spacer thickness, and local surface density of emitters enables a higher entropy density than other nanoparticle O-PUF concepts.

The next modification of nanomaterial-based O-PUF developed here used monolayer WS_2 as the source of the optical emission, due to its cost, environmental benefits, and future potential in fabrication scalability. Due to the relative uniformity of a single monolayer of micromechanically exfoliated WS_2, the previously established technique of the addition of AuNPs to the sample substrate to locally modify the emission properties of the 2D TMDC is used. The interaction between the 2D material and the AuNPs both increases the dynamic range of emission intensity, as with the PUF modification introduced in Chapter 4, and, because it induces structural defects, they modify the peak PL position and line shape, increasing the range of potential CRPs within the device. It was shown that not only does the peak emission value of the flake increase, but the increased strain, doping, or any other local defect that arises during this process also modifies the peak position, line shape, and Raman spectra. The sensitivity of the optical properties to naturally occurring defects make them attractive as the foundation of unique objects.

6.1.1 Key Improvements to O-PUF Design.

The developments of some of the key figures of merit of O-PUFs which were established in Chapter 2.1.3 and are detailed in this thesis are summarised in Table 2. Here, the current key figures of merit and remaining weaknesses of existing constellation-style O-PUFs are addressed with the improvements made throughout this thesis.

Figure of merit	Existing O-PUF weakness	Improvements made
Evaluability	Many O-PUFs require high-resolution optical or microscopy-based techniques.	The characterisation of the QD linearity in Chapter 4 using far-field macro-PL paves the way for QD O-PUF characterisation with more practical means in real-world applications.
Unclonability	Some constellation-style O-PUF designs are vulnerable to simulation or cloning attacks.	Procedural challenges of the same QD-based O-PUF with an increased excitation power verifies a nonlinear response, which confirms the presence of quantum emitters on the surface.
High entropy density	Increasing the entropy density of a constellation-style O-PUF requires a higher resolution tag.	Addition of plasmonic nanoparticles in Chapter 4 increased the dynamic range of emission, therefore the density of possible CRPs (bit density), without increasing the size of the tag, or resolution of the measurement.
Suitability for a wide variety of applications, including food-safe applications	QD-based O-PUFs may be toxic, so are not suitable for pharmaceutical applications.	Development of 2D material-based O-PUF removes harmful components for food/pharmaceutical applications and reduces material cost.

Table 2: Improvements to key figures of merit for PUFs made in this work.

6.2 Future Work

There are several natural next steps for this work to continue, to improve the viability and reliability of the concept of the nanomaterial O-PUF, which were not explored in this work due to the complexity of the work, or time restraints on the project. This section will predominantly discuss works which follow from the works for the TMDC O-PUF introduced in Chapter 5: additional measurements and modifications in the natural next avenue of exploration would be to fully unite the techniques utilised earlier in the work, where the overall linearity of the 2D material emission in response to a variable excitation source can be explored with far-field optical techniques. Subsequently, details and potential further developments to improve the key figures of merit of O-PUFs introduced in Chapter 2.1.3 are discussed.

6.2.1 Scalability of 2D Material Fabrication

WS_2 was selected as the optical 2D material for the TMDC-based O-PUF because it has emission in the visible range of the spectrum and has a relatively high external quantum efficiency[101]. However, micro-mechanically exfoliated layers of 2D crystals have disadvantages.

Firstly, the individual exfoliation, manipulation and transfer of ML flakes, whilst very useful for ‘prototype’ devices, is not at all scalable and is a time-consuming and expensive process for device manufacture. Because of this limitation, liquid-phase exfoliation (LPE) is a technique for the fabrication of 2D ‘inks’. There are several techniques within the classification of LPE, including sonication and shear-force exfoliation of 2D powders or crystals in a solvent, or the intercalation of Li^+ between the individual layers of the crystals, to separate them into few and single-layers, to create ‘inks’: suspensions of flakes of 2D materials, which can be deposited using several methods, including drop-casting, electrospray, and inkjet printing[133-139]. These techniques utilise the surface tension of the selected solvent, which is closely related to the inter-layer energy of the vdW crystals[134,140]. The suspension is then ultrasonicated, with a probe, or a bath sonicator. If the energy provided to the suspension is great enough to overcome the vdW bonds between the layers, the crystals will be exfoliated to thinner structures[141].

This resulting ink will have a wide distribution of sizes and thicknesses of flakes, which need to be purified to ensure only flakes with a few-number of layers (the flakes which are most likely to emit brightly) remain. A series of centrifugation steps of the solution, from a lower speed to a higher speed, gradually removes unwanted flakes. At lower speeds, the very large, thick flakes are separated from the solution, until eventually, only the lightest, thinnest flakes remain, leaving a solution of 2D flakes, which can be deposited with a variety of techniques, including drop-casting, spray-coating[142], spin coating[143], or inkjet printing[144,145].

6.2.2 Investigation of the Effect of Local Defects in 2D Materials

Introduced briefly in Chapter 5, both the process of micromechanical transfer of 2D flakes, and the addition of relatively large (on the scale of 2D material thickness) nanoparticles underneath the surface will induce local structural defects. Primarily, these 100nm nanoparticles will induce strain, but also could cause doping, cracks, grain boundaries and point defects, such as vacancies. All of these defects will have an effect on the local PL from the samples. Preliminary work had been started on this project, including experiments into the deposition of inert (SiO_2) nanoparticles, and extensive maps over large areas of 2D flakes, to correlate them with their physical properties. However, more work needs to be done to create a uniform, discrete distribution of these NPs on a surface. A large (25x25µm) map was performed across a large, damaged MoS_2 flake on an Si+SiO_2 substrate, to correlate the physical properties with the optical emission properties of the semiconductor. The peak emission intensity map of the flake is shown in Figure 6-1. The next steps would be to take much higher resolution AFM and PL measurements, in conjunction with Raman, and potentially other techniques, such as X-ray photoelectron spectroscopy (XPS), to obtain a better understanding of the underlying physics of these local defects, and what effect they have on the optical properties of these materials.

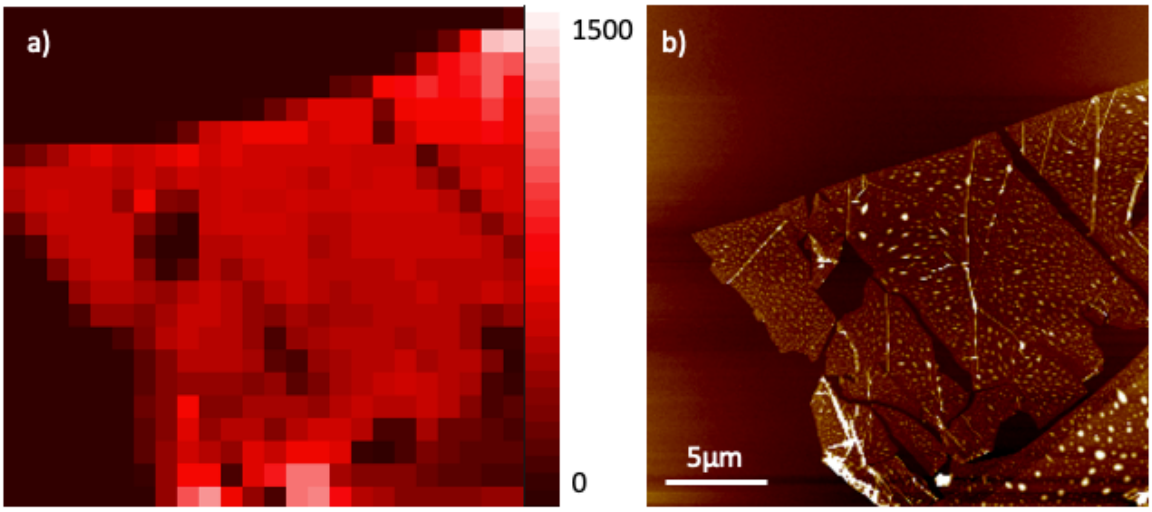

Figure 6-1: a) A micro-PL map of an as-transferred MoS_2 flake onto a Si/SiO_2 substrate, showing the peak emission cts/s. b) A contact-mode AFM image of the flake, showing clear cracks, bubbles, and different layer thicknesses. Some of the features in the PL can be attributed to physical properties through AFM.

6.2.3 PUF Evaluability

This section considers potential developments to QD and 2D material-based O-PUFs discussed in this thesis to improve their evaluability, including their overall emission brightness, and long-term stability.

6.2.3.1 Improvement of the External Quantum Efficiency of 2D Crystals

Whilst WS_2 was used for the 2D O-PUF because it is a relatively bright TMDC, for practical use in a commercial PUF, it should have an external QY similar to that of the InP/ZnS QDs used in the QD-PUFs. This would improve the evaluability of the 2D O-PUF, for evaluation and interrogation with a far-field, less sensitive optical system. A well-studied mechanism for significantly increasing the QY from sulphur based monolayer TMDCs (WS_2, MoS_2) involves the treatment of the flakes with a superacid. The addition of bis(trifluoromethane)sulfonimide to a prepared layer of MoS_2 has been demonstrated to increase its QY from <1% in untreated flakes to almost unity[131,132]. The mechanism for this increase is not fully understood, but it potentially introduces a pathway that passivates any sulphur vacancies which would decrease the radiative recombination rate. It is likely that the addition of the acid will dope the ML: WS_2 and MoS_2 are naturally n-type semiconductors, so treatment with the superacid which p-dopes the flake will suppress non-radiative interactions with excess negative charges[146,147].

6.2.3.2 Longevity, Protection of Samples and Tamper Resistance

To be useful as a consumer-grade PUF, all of the O-PUFs introduced in this thesis must be stable, so it provides the same response when challenged during their lifetime. Therefore, not only does the PUF need to be robust enough to not be easily damaged, but the material components (specifically the QDs or 2DM layer) are required to be stable over time. Under ambient conditions, emitting TMDCs are known to oxidise, reducing their optical performance over time. Therefore, protecting the samples will prevent oxidation, and reduce the likelihood of damage. Work has been shown to be effective in increasing the light output from 2D materials by the addition of a solid immersion lens (SIL), which may also provide adequate protection of these devices, whilst making them easier to characterise by far-field optical techniques[148]. Alternatively, the addition of a transparent polymer layer (e.g. lamination) to the samples to protect them may be effective, so a study to investigate the longevity of the QDs and 2D TMDCs would be valuable for the development of these O-PUFs[149].

A figure of merit for any PUF which has not yet been discussed in this work is tamper evidence: the act of tampering with the system is to permanently damage or alter the physical state of the system, usually with malicious intent. For the device to be tamper-resistant, it must provide some evidence, and generate a different response[2]. For example, if the nanomaterials are enclosed in a sealed environment that has been tampered with, their response will change, as the ambient conditions start to modify their emission. WS_2 ages and oxidises relatively quickly in ambient conditions, so the doping of the flake which occurs over time changes the emission spectra lineshape, and peak position, due to the increase in charged exciton population. Figure 6-2 shows the normalised spectra of a fresh crystal of monolayer WS_2, and a flake which has been left in ambient conditions for >2 months. The change in exciton population produces a significant shift in peak emission position.

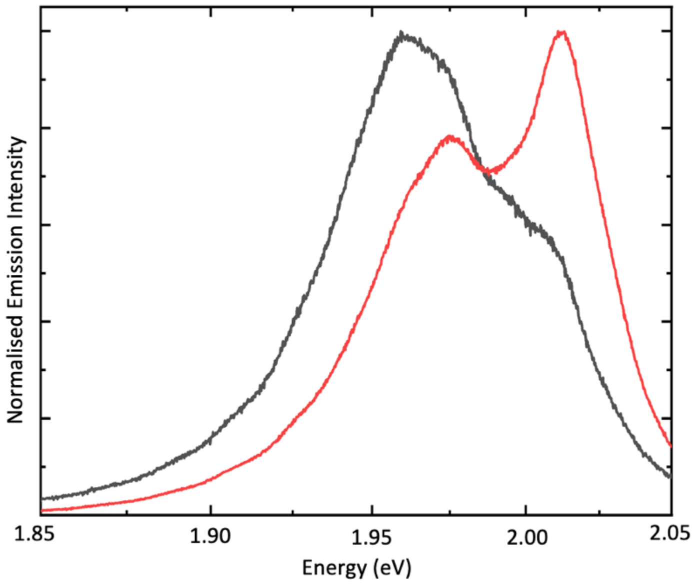

Figure 6-2 Change in peak emission intensity of monolayer WS_2 flake with time. Red trace is a freshly exfoliated monolayer. Black trace is a monolayer left in ambient conditions for 2 months.

6.2.3.3 Simplification of Interrogation Technique

The simpler the interrogation technique for an O-PUF, the better its evaluability. In Chapter 4, the main characterisation technique to demonstrate the nonlinearity of the QD response was macro photoluminescence. This was achievable because the devices being characterised were large, and emitted PL relatively brightly. However, in later chapters, the PUF's emission was modified with gold nanoparticles, which is a highly localised change. This change in PL properties approaches the spatial limit that is possible to be characterised by a far-field optical technique. In the case of the PUF designed in Chapter 5, the size of the optically active area is a limiting factor in measurement technique: the experimental sample was a 'relatively large' 2D flake, and yet was >100µm along its longest axis. This, when measured using a far-field technique, such as macro PL, won't produce enough CRPs, because the resolution and sensitivity of current systems is not great enough.

The linearity of the emission response of both the AuNP + QD O-PUF introduced in Chapter 4, and the 2D O-PUF described in Chapter 5 was not discussed or characterised, but is the natural next step of improvement for these PUFs, to combine the works discussed throughout this thesis with the measurement technique discussed in Chapter 4. As a quantum-confined optical material, the TMDC emission properties will have similar behaviour to that of the QDs, enabling a further layer of security to the 2D O-PUF, on top of the variation in emission characteristics from localised defects, substrate interaction and AuNPs.

Bibliography

1 Pappu, R., Recht, B., Taylor, J. & Gershenfeld, N. Physical One-Way Functions. *Science* **297**, 2026 (2002). https://doi.org:10.1126/science.1074376

2 Maes, R. *Physically Unclonable Functions: Constructions, Properties and Applications*. 2013 edn, Vol. 9783642413957 (Berlin, Heidelberg: Springer Berlin / Heidelberg, 2013).

3 Rührmair, U., Busch, H. & Katzenbeisser, S. in *Towards Hardware-Intrinsic Security: Foundations and Practice* (eds Ahmad-Reza Sadeghi & David Naccache) 79-96 (Springer Berlin Heidelberg, 2010).

4 Cao, Y. *et al.* Optical identification using imperfections in 2D materials. *2D Materials* **4**, 045021 (2017). https://doi.org:10.1088/2053-1583/aa8b4d

5 Elder, D. *The cost of drug counterfeiting*, <https://www.europeanpharmaceuticalreview.com/article/29919/the-cost-of-drug-counterfeiting/> (

6 Hammouri, G., Dana, A. & Sunar, B. in *Cryptographic Hardware and Embedded Systems - CHES 2009.* (eds Christophe Clavier & Kris Gaj) 348-362 (Springer Berlin Heidelberg).

7 Wong, C. & Wu, M. in *2015 IEEE International Workshop on Information Forensics and Security (WIFS).* 1-6.

8 National Research, C. *Counterfeit Deterrent Features for the Next-Generation Currency Design*. (The National Academies Press, 1993).

9 Bulens, P., Standaert, F. X. & Quisquater, J. J. How to strongly link data and its medium: the paper case. *IET Information Security* **4**, 125-136 (2010).

10 Smith, A. F., Patton, P. & Skrabalak, S. E. Plasmonic Nanoparticles as a Physically Unclonable Function for Responsive Anti-Counterfeit Nanofingerprints. *Advanced Functional Materials* **26**, 1315-1321 (2016). https://doi.org:10.1002/adfm.201503989

11 Kuemin, C., Nowack, L., Bozano, L., Spencer, N. D. & Wolf, H. Oriented Assembly of Gold Nanorods on the Single-Particle Level. *Advanced Functional Materials* **22**, 702-708 (2012). https://doi.org:10.1002/adfm.201101760

12 Liu, Y. *et al.* Inkjet-printed unclonable quantum dot fluorescent anti-counterfeiting labels with artificial intelligence authentication. *Nature Communications* **10**, 2409 (2019). https://doi.org:10.1038/s41467-019-10406-7

13 Chen, L., Lai, C., Marchewka, R., Berry, R. M. & Tam, K. C. Use of CdS quantum dot-functionalized cellulose nanocrystal films for anti-counterfeiting applications. *Nanoscale* **8**, 13288-13296 (2016). https://doi.org:10.1039/C6NR03039D

14 Ivanova, O., Elliott, A., Campbell, T. & Williams, C. B. Unclonable security features for additive manufacturing. *Additive Manufacturing* **1-4**, 24-31 (2014). https://doi.org:https://doi.org/10.1016/j.addma.2014.07.001

15 Agrawal, T. K., Campagne, C. & Koehl, L. Development and characterisation of secured traceability tag for textile products by printing process. *The International Journal of Advanced Manufacturing Technology* **101**, 2907-2922 (2019). https://doi.org:10.1007/s00170-018-3134-z

16 Kim, J. *et al.* Anti-counterfeit nanoscale fingerprints based on randomly distributed nanowires. *Nanotechnology* **25**, 155303 (2014). https://doi.org:10.1088/0957-4484/25/15/155303

17 Cheng, H. *et al.* Plasmonic nanopapers: flexible, stable and sensitive multiplex PUF tags for unclonable anti-counterfeiting applications. *Nanoscale* **12**, 9471-9480 (2020). https://doi.org:10.1039/D0NR01223H

18 Cui, Y. *et al.* Multiplex plasmonic anti-counterfeiting security labels based on surface-enhanced Raman scattering. *Chemical Communications* **51**, 5363-5366 (2015). https://doi.org:10.1039/C4CC08596E

19 Chong, C. N., Jiang, D., Zhang, J. & Guo, L. in *2008 Second International Conference on Emerging Security Information, Systems and Technologies.* 146-153.

20 Chen, F. *et al.* Unclonable fluorescence behaviors of perovskite quantum dots/chaotic metasurfaces hybrid nanostructures for versatile security primitive. *Chemical Engineering Journal* **411**, 128350 (2021). https://doi.org:https://doi.org/10.1016/j.cej.2020.128350

21 Alharbi, A., Armstrong, D., Alharbi, S. & Shahrjerdi, D. Physically Unclonable Cryptographic Primitives by Chemical Vapor Deposition of Layered MoS2. *ACS Nano* **11**, 12772-12779 (2017). https://doi.org:10.1021/acsnano.7b07568

22 Zheng, X. *et al.* Inkjet-Printed Quantum Dot Fluorescent Security Labels with Triple-Level Optical Encryption. *ACS Applied Materials & Interfaces* (2021). https://doi.org:10.1021/acsami.1c02390

23 Gu, Y. *et al.* Gap-enhanced Raman tags for physically unclonable anticounterfeiting labels. *Nature Communications* **11**, 516 (2020). https://doi.org:10.1038/s41467-019-14070-9

24 Kittel, C. *Introduction to solid state physics*. 8th ed. edn, (Wiley, 2005).

25 Guenault, T. *Statistical Physics*. 1st ed. edn, (1995).

26 Wigner, E. & Seitz, F. On the Constitution of Metallic Sodium. *Physical Review* **43**, 804-810 (1933). https://doi.org:10.1103/PhysRev.43.804

27 Shi, H. *et al.* Exciton dynamics in suspended monolayer and few-layer MoS_2 2D crystals.

28 Sattler, K. D. *Handbook of Nanophysics : Nanoparticles and Quantum Dots*. (Taylor & Francis Group, 2010).

29 Su, Q., Zhang, H. & Chen, S. Identification of excess charge carriers in InP-based quantum-dot light-emitting diodes. *Applied Physics Letters* **117**, 053502 (2020).

30 Zhang, W. *et al.* InP/ZnS/ZnS Core/Shell Blue Quantum Dots for Efficient Light‐Emitting Diodes. *Advanced functional materials* **30**, n/a (2020). https://doi.org:10.1002/adfm.202005303

31 Peng, X., Wickham, J. & Alivisatos, A. P. Kinetics of II-VI and III-V Colloidal Semiconductor Nanocrystal Growth: "Focusing" of Size Distributions. *Journal of the American Chemical Society* **120**, 5343-5344 (1998). https://doi.org:10.1021/ja9805425

32 Sinatra, L., Pan, J. & Bakr, O. M. Methods of synthesizing monodisperse colloidal quantum dots. *Material Matters* **12**, 3-7 (2017).

33 Novoselov, K. S., Mishchenko, A., Carvalho, A. & Castro Neto, A. H. 2D materials and van der Waals heterostructures. *Science* **353**, aac9439 (2016). https://doi.org:10.1126/science.aac9439

34 Novoselov, K. S. *et al.* Two-dimensional atomic crystals. *Proceedings of the National Academy of Sciences of the United States of America* **102**, 10451 (2005). https://doi.org:10.1073/pnas.0502848102

35 Mak, K. F., Lee, C., Hone, J., Shan, J. & Heinz, T. F. Atomically Thin ${\mathrm{MoS}}_{2}$: A New Direct-Gap Semiconductor. *Physical Review Letters* **105**, 136805 (2010). https://doi.org:10.1103/PhysRevLett.105.136805

36 Liu, H. *et al.* Phosphorene: An Unexplored 2D Semiconductor with a High Hole Mobility. *ACS Nano* **8**, 4033-4041 (2014). https://doi.org:10.1021/nn501226z

37 Chaves, A. *et al.* Bandgap engineering of two-dimensional semiconductor materials. *npj 2D Materials and Applications* **4**, 29 (2020). https://doi.org:10.1038/s41699-020-00162-4

38 Conley, H. J. *et al.* Bandgap Engineering of Strained Monolayer and Bilayer MoS2. *Nano Letters* **13**, 3626-3630 (2013). https://doi.org:10.1021/nl4014748

39 Zhu, C. R. *et al.* Strain tuning of optical emission energy and polarization in monolayer and bilayer MoS${}_{2}$. *Physical Review B* **88**, 121301 (2013). https://doi.org:10.1103/PhysRevB.88.121301

40 He, K., Poole, C., Mak, K. F. & Shan, J. Experimental Demonstration of Continuous Electronic Structure Tuning via Strain in Atomically Thin MoS2. *Nano Letters* **13**, 2931-2936 (2013). https://doi.org:10.1021/nl4013166

41 Wang, K. & Paulus, B. Tuning the binding energy of excitons in the MoS2 monolayer by molecular functionalization and defective engineering. *Physical Chemistry Chemical Physics* **22**, 11936-11942 (2020). https://doi.org:10.1039/D0CP01239D

42 Nan, H. *et al.* Strong Photoluminescence Enhancement of MoS2 through Defect Engineering and Oxygen Bonding. *ACS Nano* **8**, 5738-5745 (2014). https://doi.org:10.1021/nn500532f

43 Kang, N., Paudel, H. P., Leuenberger, M. N., Tetard, L. & Khondaker, S. I. Photoluminescence Quenching in Single-Layer MoS2 via Oxygen Plasma Treatment. *The Journal of Physical Chemistry C* **118**, 21258-21263 (2014). https://doi.org:10.1021/jp506964m

44 Faraday, M. X. The Bakerian Lecture. —Experimental relations of gold (and other metals) to light. *Philosophical Transactions of the Royal Society of London* **147**, 145-181 (1857). https://doi.org:10.1098/rstl.1857.0011

45 Maier, S. A. *Plasmonics : fundamentals and applications*. (Springer, 2007).

46 Pelton, M. & Bryant, G. W. *Introduction to Metal-Nanoparticle Plasmonics*. (John Wiley & Sons, Incorporated, 2013).

47 Wang, Z. *et al.* Giant photoluminescence enhancement in tungsten-diselenide–gold plasmonic hybrid structures. *Nature Communications* **7**, 11283 (2016). https://doi.org:10.1038/ncomms11283

48 Iwase, H., Englund, D. & Vučković, J. Analysis of the Purcell effect in photonic and plasmonic crystals with losses. *Opt. Express* **18**, 16546-16560 (2010). https://doi.org:10.1364/OE.18.016546

49 Francs, G. C. d. *et al.* Plasmonic Purcell factor and coupling efficiency to surface plasmons. Implications for addressing and controlling optical nanosources. *Journal of Optics* **18**, 094005 (2016). https://doi.org:10.1088/2040-8978/18/9/094005

50 Anger, P., Bharadwaj, P. & Novotny, L. Enhancement and Quenching of Single-Molecule Fluorescence. *Physical Review Letters* **96**, 113002 (2006). https://doi.org:10.1103/PhysRevLett.96.113002

51 Velicky, M. *et al.* Mechanism of Gold-Assisted Exfoliation of Centimeter-Sized Transition-Metal Dichalcogenide Monolayers. *Acs Nano* **12**, 10463-10472 (2018). https://doi.org:10.1021/acsnano.8b06101

52 Godin, K., Cupo, C. & Yang, E. H. Reduction in Step Height Variation and Correcting Contrast Inversion in Dynamic AFM of WS2 Monolayers. *Scientific Reports* **7** (2017). https://doi.org:ARTN 17798
10.1038/s41598-017-18077-4

53 Pini, V. *et al.* Spatially multiplexed dark-field microspectrophotometry for nanoplasmonics. *Scientific Reports* **6** (2016). https://doi.org:ARTN 22836
10.1038/srep22836

54 Chaabani, W. *et al.* Large-Scale and Low-Cost Fabrication of Silicon Mie Resonators. *Acs Nano* **13**, 4199-4208 (2019). https://doi.org:10.1021/acsnano.8b09198

55 Bruker. *Quantitative Mechanical Property Mapping at the Nanoscale with PeakForce QNM*, <www.bruker.com> (

56 Huang, Y. *et al.* Reliable Exfoliation of Large-Area High-Quality Flakes of Graphene and Other Two-Dimensional Materials. *ACS Nano* **9**, 10612-10620 (2015). https://doi.org:10.1021/acsnano.5b04258

57 Anderson, B. R., Gunawidjaja, R. & Eilers, H. Initial tamper tests of novel tamper-indicating optical physical unclonable functions. *Appl. Opt.* **56**, 2863-2872 (2017). https://doi.org:10.1364/AO.56.002863

58 Arppe-Tabbara, R., Tabbara, M. & Sørensen, T. J. Versatile and Validated Optical Authentication System Based on Physical Unclonable Functions. *ACS Applied Materials & Interfaces* **11**, 6475-6482 (2019). https://doi.org:10.1021/acsami.8b17403

59 Wu, P., Xu, C., Hou, X., Xu, J.-J. & Chen, H.-Y. Dual-emitting quantum dot nanohybrid for imaging of latent fingerprints: simultaneous identification of individuals and traffic light-type

visualization of TNT. *Chemical Science* **6**, 4445-4450 (2015). https://doi.org:10.1039/C5SC01497B

60 Marcinkevicius, P. *et al.* in *2019 Design, Automation & Test in Europe Conference & Exhibition (DATE).* 198-203.

61 Smith, A. M. & Nie, S. Semiconductor Nanocrystals: Structure, Properties, and Band Gap Engineering. *Accounts of Chemical Research* **43**, 190-200 (2010). https://doi.org:10.1021/ar9001069

62 Yang, S., Zhao, P., Zhao, X., Qu, L. & Lai, X. InP and Sn:InP based quantum dot sensitized solar cells. *Journal of Materials Chemistry A* **3**, 21922-21929 (2015). https://doi.org:10.1039/C5TA04925C

63 Brus, L. E. Electron–electron and electron‐hole interactions in small semiconductor crystallites: The size dependence of the lowest excited electronic state. *The Journal of Chemical Physics* **80**, 4403-4409 (1984). https://doi.org:10.1063/1.447218

64 Murray, C. B., Norris, D. J. & Bawendi, M. G. Synthesis and characterization of nearly monodisperse CdE (E = sulfur, selenium, tellurium) semiconductor nanocrystallites. *Journal of the American Chemical Society* **115**, 8706-8715 (1993). https://doi.org:10.1021/ja00072a025

65 Frederick, M. T., Amin, V. A. & Weiss, E. A. Optical Properties of Strongly Coupled Quantum Dot–Ligand Systems. *The Journal of Physical Chemistry Letters* **4**, 634-640 (2013). https://doi.org:10.1021/jz301905n

66 Brichkin, S. B. & Razumov, V. F. Colloidal quantum dots: synthesis, properties and applications. *Russian Chemical Reviews* **85**, 1297-1312 (2016). https://doi.org:10.1070/rcr4656

67 Kang, H.-G. *et al.* Probing dynamic fluorescence properties of single and clustered quantum dots toward quantitative biomedical imaging of cells: Probing dynamic fluorescence properties of single and clustered quantum dots. *Wiley interdisciplinary reviews. Nanomedicine and nanobiotechnology* **2**, 48-58 (2010). https://doi.org:10.1002/wnan.62

68 Novotny, L. & Hecht, B. *Principles of Nano-Optics*. (Cambridge University Press, 2006).

69 Forchel, A. *et al.* Optical studies of free-standing single InGaAs/GaAs quantum dots. *Semiconductor Science and Technology* **11**, 1529-1533 (1996). https://doi.org:10.1088/0268-1242/11/11s/013

70 Alejo, T. *et al.* Influence of 3D aggregation on the photoluminescence dynamics of CdSe quantum dot films. *Journal of Luminescence* **183**, 113-120 (2017). https://doi.org:https://doi.org/10.1016/j.jlumin.2016.11.002

71 Noh, M. *et al.* Fluorescence quenching caused by aggregation of water-soluble CdSe quantum dots. *Colloids and Surfaces A: Physicochemical and Engineering Aspects* **359**, 39-44 (2010). https://doi.org:https://doi.org/10.1016/j.colsurfa.2010.01.059

72 Kumar, B. G. *et al.* Structural control of InP/ZnS core/shell quantum dots enables high-quality white LEDs. *Nanotechnology* **29**, 345605 (2018). https://doi.org:10.1088/1361-6528/aac8c9

73 He, L., Smith, E. A., Natan, M. J. & Keating, C. D. The Distance-Dependence of Colloidal Au-Amplified Surface Plasmon Resonance. *The Journal of Physical Chemistry B* **108**, 10973-10980 (2004). https://doi.org:10.1021/jp048536k

74 Swierczewska, M., Lee, S. & Chen, X. The design and application of fluorophore–gold nanoparticle activatable probes. *Physical Chemistry Chemical Physics* **13**, 9929-9941 (2011). https://doi.org:10.1039/C0CP02967J

75 Jiao, X., Wang, Y. & Blair, S. Plasmonic Enhancement of UV Fluorescence. *Surface Plasmon Enhanced, Coupled and Controlled Fluorescence*, 295-308 (2017). https://doi.org:10.1002/9781119325161.ch18

76 Kelly, K. L., Coronado, E., Zhao, L. L. & Schatz, G. C. The Optical Properties of Metal Nanoparticles: The Influence of Size, Shape, and Dielectric Environment. *The Journal of Physical Chemistry B* **107**, 668-677 (2003). https://doi.org:10.1021/jp026731y

77 Zheng, Y. *et al.* Unclonable Plasmonic Security Labels Achieved by Shadow-Mask-Lithography-Assisted Self-Assembly. *Advanced Materials* **28**, 2330-2336 (2016). https://doi.org:10.1002/adma.201505022

78 Heydari, E., Greco, T. & Stumpe, J. Enhancement of QDs photoluminescence by localized surface plasmon effect of Au-NPs. *Proc. of SPIE* **8424**, 55 (2012). https://doi.org:10.1117/12.922778

79 Mueller, N. S. *et al.* Plasmonic enhancement of SERS measured on molecules in carbon nanotubes. *Faraday Discuss* **205**, 85-103 (2017). https://doi.org:10.1039/c7fd00127d

80 Born, M. *Principles of optics. Electromagnetic theory of propagation, interference, and diffraction of light*. 5th ed. edn, (Pergamon Press, 1975).

81 Gorobez, J., Maack, B. & Nilius, N. Growth of Self-Passivating Oxide Layers on Aluminum-Pressure and Temperature Dependence. *Phys Status Solidi B* **258** (2021). https://doi.org:ARTN 2000559
10.1002/pssb.202000559

82 Abdelazim, N. M. *et al.* Hotspot generation for unique identification with nanomaterials. *Scientific Reports* **11** (2021). https://doi.org:ARTN 1528
10.1038/s41598-020-79644-w

83 Eklöf, J., Gschneidtner, T., Lara-Avila, S., Nygård, K. & Moth-Poulsen, K. Controlling deposition of nanoparticles by tuning surface charge of SiO2 by surface modifications. *RSC Advances* **6**, 104246-104253 (2016). https://doi.org:10.1039/C6RA22412A

84 Paul, S. *et al.* Langmuir−Blodgett Film Deposition of Metallic Nanoparticles and Their Application to Electronic Memory Structures. *Nano Letters* **3**, 533-536 (2003). https://doi.org:10.1021/nl034008t

85 Solis, H., Clark, N., Azofeifa, D. & Avendano, E. Room temperature gas-solid reaction of titanium on glass surfaces forming a very low resistivity layer. *Aip Adv* **6** (2016). https://doi.org:Artn 095218
10.1063/1.4963679

86 Mubeen, S. *et al.* Plasmonic Properties of Gold Nanoparticles Separated from a Gold Mirror by an Ultrathin Oxide. *Nano Letters* **12**, 2088-2094 (2012). https://doi.org:10.1021/nl300351j

87 Nychyporuk, T. *et al.* Strong photoluminescence enhancement of silicon quantum dots by their near-resonant coupling with multi-polar plasmonic hot spots. *Nanoscale* **3**, 2472-2475 (2011). https://doi.org:10.1039/C1NR10241A

88 Naumov, I. I., Li, Z. & Bratkovsky, A. M. Plasmonic resonances and hot spots in Ag octopods. *Applied Physics Letters* **96**, 033105 (2010). https://doi.org:10.1063/1.3273859

89 Bek, A. *et al.* Fluorescence Enhancement in Hot Spots of AFM-Designed Gold Nanoparticle Sandwiches. *Nano Letters* **8**, 485-490 (2008). https://doi.org:10.1021/nl072602n

90 Coblentz, W. W. The reflecting power of various metals. *J Frankl Inst* **170**, 169-193 (1910). https://doi.org:Doi 10.1016/S0016-0032(10)90867-3

91 Nirmal, M. *et al.* Fluorescence intermittency in single cadmium selenide nanocrystals. *Nature* **383**, 802-804 (1996). https://doi.org:10.1038/383802a0

92 Ghimire, S. & Biju, V. Relations of exciton dynamics in quantum dots to photoluminescence, lasing, and energy harvesting. *Journal of Photochemistry and Photobiology C: Photochemistry Reviews* **34**, 137-151 (2018). https://doi.org:https://doi.org/10.1016/j.jphotochemrev.2018.01.004

93 Efros, A. L. Almost always bright. *Nature Materials* **7**, 612-613 (2008). https://doi.org:10.1038/nmat2239

94 Efros, A. L. & Nesbitt, D. J. Origin and control of blinking in quantum dots. *Nature Nanotechnology* **11**, 661-671 (2016). https://doi.org:10.1038/nnano.2016.140

95 Lin, J., Li, X., Wang, M., Liu, L. & Dai, T. How Can China's Indium Resources Have a Sustainable Future? Research Based on the Industry Chain Perspective. *Sustainability* **13** (2021). https://doi.org:10.3390/su132112042

96 Cui, Q. *et al.* Robust and High Photoluminescence in WS2 Monolayer through In Situ Defect Engineering. *Advanced Functional Materials* **31**, 2105339 (2021). https://doi.org:https://doi.org/10.1002/adfm.202105339

97 Ren, D.-D. *et al.* Photoluminescence inhomogeneity and excitons in CVD-grown monolayer WS2. *Optical Materials* **80**, 203-208 (2018). https://doi.org:https://doi.org/10.1016/j.optmat.2018.04.043

98 Xu, Z. *et al.* CVD controlled growth of large-scale WS2 monolayers. *RSC Advances* **9**, 29628-29635 (2019). https://doi.org:10.1039/C9RA06219J

99 Xu, L. *et al.* Analysis of photoluminescence behavior of high-quality single-layer MoS2. *Nano Research* **12**, 1619-1624 (2019). https://doi.org:10.1007/s12274-019-2401-0

100 Manikandan, A. *et al.* A critical review on two-dimensional quantum dots (2D QDs): From synthesis toward applications in energy and optoelectronics. *Progress in Quantum Electronics* **68**, 100226 (2019). https://doi.org:https://doi.org/10.1016/j.pquantelec.2019.100226

101 Roy, S. *et al.* Measurement of Quantum Yields of Monolayer TMDs Using Dye-Dispersed PMMA Thin Films. *Nanomaterials* **10** (2020). https://doi.org:10.3390/nano10061032

102 Mohamed, N. B. *et al.* Long radiative lifetimes of excitons in monolayer transition-metal dichalcogenidesMX2(M= Mo, W;X= S, Se). *Applied Physics Express* **11**, 015201 (2017). https://doi.org:10.7567/apex.11.015201

103 Brent, J. R., Savjani, N. & O'Brien, P. Synthetic approaches to two-dimensional transition metal dichalcogenide nanosheets. *Progress in Materials Science* **89**, 411-478 (2017). https://doi.org:https://doi.org/10.1016/j.pmatsci.2017.06.002

104 Kandhasamy, D. M. *et al.* Synthesis and Photoluminescence Properties of MoS2/Graphene Heterostructure by Liquid-Phase Exfoliation. *ACS Omega* **7**, 629-637 (2022). https://doi.org:10.1021/acsomega.1c05250

105 Verhagen, T., Guerra, V. L. P., Haider, G., Kalbac, M. & Vejpravova, J. Towards the evaluation of defects in MoS2 using cryogenic photoluminescence spectroscopy. *Nanoscale* **12**, 3019-3028 (2020). https://doi.org:10.1039/C9NR07246B

106 Rhodes, C. J. Endangered elements, critical raw materials and conflict minerals. *Science Progress* **102**, 304-350 (2019). https://doi.org:10.1177/0036850419884873

107 Singh, K. K., Prabhu B, R., Choudhary, S., Pramanik, C. & John, N. S. Effect of Graphene and MoS2 Flakes in Industrial Oils to Enhance Lubrication. *ACS Omega* **4**, 14569-14578 (2019). https://doi.org:10.1021/acsomega.9b01799

108 Drummond, C., Alcantar, N., Israelachvili, J., Tenne, R. & Golan, Y. Microtribology and Friction-Induced Material Transfer in WS2 Nanoparticle Additives. *Advanced Functional Materials* **11**, 348-354 (2001). https://doi.org:https://doi.org/10.1002/1616-3028(200110)11:5<348::AID-ADFM348>3.0.CO;2-S

109 Hilton, M. R. & Fleischauer, P. D. Applications of solid lubricant films in spacecraft. *Surface and Coatings Technology* **54-55**, 435-441 (1992). https://doi.org:https://doi.org/10.1016/S0257-8972(07)80062-4

110 Cohen, S. R. *et al.* The tribological behavior of type II textured MX2 (M=Mo, W; X=S, Se) films. *Thin Solid Films* **324**, 190-197 (1998). https://doi.org:https://doi.org/10.1016/S0040-6090(97)01218-2

111 Butun, S., Tongay, S. & Aydin, K. Enhanced Light Emission from Large-Area Monolayer MoS2 Using Plasmonic Nanodisc Arrays. *Nano Letters* **15**, 2700-2704 (2015). https://doi.org:10.1021/acs.nanolett.5b00407

112 Lee, Y.-C., Tseng, Y.-C. & Chen, H.-L. Single Type of Nanocavity Structure Enhances Light Outcouplings from Various Two-Dimensional Materials by over 100-Fold. *ACS Photonics* **4**, 93-105 (2017). https://doi.org:10.1021/acsphotonics.6b00601

113 Ogilvie, S. P. *et al.* Size selection of liquid-exfoliated 2D nanosheets. *2d Materials* **6** (2019). https://doi.org:ARTN 031002
10.1088/2053-1583/ab0dc3

114 Brucker. *Overview of AFM Operation*, <http://nanophys.kth.se/nanophys/facilities/nfl/afm/icon/bruker-help/Content/PeakForceQNM/Operation/Channels.htm> (2010).

115 Iqbal, M. W., Shahzad, K., Akbar, R. & Hussain, G. A review on Raman finger prints of doping and strain effect in TMDCs. *Microelectronic Engineering* **219**, 111152 (2020). https://doi.org:https://doi.org/10.1016/j.mee.2019.111152

116 Wang, Y. *et al.* Strain-induced direct–indirect bandgap transition and phonon modulation in monolayer WS2. *Nano Research* **8**, 2562-2572 (2015). https://doi.org:10.1007/s12274-015-0762-6

117 Shuai, Q., Hang, Y., Zongqi, B., Gang, P. & Xueao, Z. in *Proceedings of the 2017 5th International Conference on Mechatronics, Materials, Chemistry and Computer Engineering (ICMMCCE 2017).* 1408-1413 (Atlantis Press).

118 Berkdemir, A. *et al.* Identification of individual and few layers of WS2 using Raman Spectroscopy. *Scientific Reports* **3**, 1755 (2013). https://doi.org:10.1038/srep01755

119 Sasaki, S. *et al.* Growth and optical properties of Nb-doped WS2 monolayers. *Applied Physics Express* **9** (2016). https://doi.org:10.7567/APEX.9.071201

120 Plechinger, G. *et al.* Identification of excitons, trions and biexcitons in single-layer WS2. (2015). https://doi.org:10.1002/pssr.201510224

121 Zhu, B., Chen, X. & Cui, X. Exciton Binding Energy of Monolayer WS2. *Scientific Reports* **5**, 9218 (2015). https://doi.org:10.1038/srep09218

122 Lin, Y. *et al.* Dielectric Screening of Excitons and Trions in Single-Layer MoS2. *Nano Letters* **14**, 5569-5576 (2014). https://doi.org:10.1021/nl501988y

123 McCreary, A. *et al.* Distinct photoluminescence and Raman spectroscopy signatures for identifying highly crystalline WS2 monolayers produced by different growth methods. *Journal of Materials Research* **31**, 931-944 (2016). https://doi.org:10.1557/jmr.2016.47

124 Gołasa, K. *et al.* Optical Properties of Molybdenum Disulfide (MoS 2). *Acta Physica Polonica, A.* **124** (2013).

125 Li, H. *et al.* From Bulk to Monolayer MoS2: Evolution of Raman Scattering. *Advanced Functional Materials* **22**, 1385-1390 (2012). https://doi.org:10.1002/adfm.201102111

126 Geim, A. K. & Grigorieva, I. V. Van der Waals heterostructures. *Nature* **499**, 419-425 (2013). https://doi.org:10.1038/nature12385

127 Zhang, Y. *et al.* Controlled growth of high-quality monolayer WS2 layers on sapphire and imaging its grain boundary. *ACS nano* **7**, 8963-8971 (2013). https://doi.org:10.1021/nn403454e

128 Song, J.-G. *et al.* Layer-Controlled, Wafer-Scale, and Conformal Synthesis of Tungsten Disulfide Nanosheets Using Atomic Layer Deposition. *ACS Nano* **7**, 11333-11340 (2013). https://doi.org:10.1021/nn405194e

129 Zhao, W. *et al.* Evolution of Electronic Structure in Atomically Thin Sheets of WS2 and WSe2. *ACS Nano* **7**, 791-797 (2013). https://doi.org:10.1021/nn305275h

130 Kim, H., Lien, D.-H., Amani, M., Ager, J. W. & Javey, A. Highly Stable Near-Unity Photoluminescence Yield in Monolayer MoS2 by Fluoropolymer Encapsulation and Superacid Treatment. *ACS Nano* **11**, 5179-5185 (2017). https://doi.org:10.1021/acsnano.7b02521

131 Amani, M. *et al.* Recombination Kinetics and Effects of Superacid Treatment in Sulfur- and Selenium-Based Transition Metal Dichalcogenides. *Nano Letters* **16**, 2786-2791 (2016). https://doi.org:10.1021/acs.nanolett.6b00536

132 Amani, M. *et al.* Near-unity photoluminescence quantum yield in MoS2. *Science* **350**, 1065-1068 (2015). https://doi.org:10.1126/science.aad2114

133 Shen, J. *et al.* Liquid Phase Exfoliation of Two-Dimensional Materials by Directly Probing and Matching Surface Tension Components. *Nano Letters* **15**, 5449-5454 (2015). https://doi.org:10.1021/acs.nanolett.5b01842

134 Coleman Jonathan, N. *et al.* Two-Dimensional Nanosheets Produced by Liquid Exfoliation of Layered Materials. *Science* **331**, 568-571 (2011). https://doi.org:10.1126/science.1194975

135 Benavente, E., Santa Ana, M. A., Mendizábal, F. & González, G. Intercalation chemistry of molybdenum disulfide. *Coordination Chemistry Reviews* **224**, 87-109 (2002). https://doi.org:https://doi.org/10.1016/S0010-8545(01)00392-7

136 Miremadi, B. K. & Morrison, S. R. The intercalation and exfoliation of tungsten disulfide. *Journal of Applied Physics* **63**, 4970-4974 (1988). https://doi.org:10.1063/1.340441

137 Yuwen, L. *et al.* Rapid preparation of single-layer transition metal dichalcogenide nanosheets via ultrasonication enhanced lithium intercalation. *Chemical Communications* **52**, 529-532 (2016). https://doi.org:10.1039/C5CC07301D

138 Ghorai, A., Midya, A., Maiti, R. & Ray, S. K. Exfoliation of WS2 in the semiconducting phase using a group of lithium halides: a new method of Li intercalation. *Dalton Transactions* **45**, 14979-14987 (2016). https://doi.org:10.1039/C6DT02823C

139 Eda, G. *et al.* Photoluminescence from Chemically Exfoliated MoS2. *Nano Letters* **11**, 5111-5116 (2011). https://doi.org:10.1021/nl201874w

140 Hernandez, Y. *et al.* High-yield production of graphene by liquid-phase exfoliation of graphite. *Nature Nanotechnology* **3**, 563-568 (2008). https://doi.org:10.1038/nnano.2008.215

141 Alzakia, F. I., Jonhson, W., Ding, J. & Tan, S. C. Ultrafast Exfoliation of 2D Materials by Solvent Activation and One-Step Fabrication of All-2D-Material Photodetectors by Electrohydrodynamic Printing. *ACS Applied Materials & Interfaces* **12**, 28840-28851 (2020). https://doi.org:10.1021/acsami.0c06279

142 Blake, P. *et al.* Graphene-Based Liquid Crystal Device. *Nano Letters* **8**, 1704-1708 (2008). https://doi.org:10.1021/nl080649i

143 Yang, S., Jiang, C. & Wei, S.-h. Gas sensing in 2D materials. *Applied Physics Reviews* **4**, 021304 (2017). https://doi.org:10.1063/1.4983310

144 McManus, D. *et al.* Water-based and biocompatible 2D crystal inks for all-inkjet-printed heterostructures. *Nature Nanotechnology* **12**, 343-350 (2017). https://doi.org:10.1038/nnano.2016.281

145 Zhang, C. *et al.* Additive-free MXene inks and direct printing of micro-supercapacitors. *Nature Communications* **10**, 1795 (2019). https://doi.org:10.1038/s41467-019-09398-1

146 Molas, M. R. *et al.* Tuning carrier concentration in a superacid treated MoS2 monolayer. *Scientific Reports* **9**, 1989 (2019). https://doi.org:10.1038/s41598-018-38413-6

147 Feng, Q. *et al.* Highly Photoluminescent Monolayer MoS2 and WS2 Achieved via Superacid Assisted Vacancy Reparation and Doping Strategy. *Laser & Photonics Reviews* **15**, 2100104 (2021).

148 Woodhead, C. S. *et al.* Increasing the light extraction and longevity of TMDC monolayers using liquid formed micro-lenses. *2D Materials* **4**, 015032 (2016). https://doi.org:10.1088/2053-1583/4/1/015032

149 Longmate, K. D., Abdelazim, N. M., Ball, E. M., Majaniemi, J. & Young, R. J. Improving the longevity of optically-read quantum dot physical unclonable functions. *Scientific Reports* **11**, 10999 (2021). https://doi.org:10.1038/s41598-021-90129-2

Glossary and List of Abbreviations

2DM – Two-Dimensional Material. See vdW crystal.

AFM – Atomic Force Microscopy

AuNPs (Gold Nanoparticles) – Small, usually spherical particles of gold with electromagnetic properties closely related to their size and shape.

CCD – Charged Coupled Device. A 2D array of Si detectors that convert incident photons to charge which can be measured.

CQD – Colloidal Quantum Dot

CVD – Chemical Vapour Deposition

CBM – Conduction Band Minimum

Dielectric – An electrical insulator, which can be polarised by an incident electromagnetic field.

FGR (Fermi's Golden Rule) – A description of the probability of a quantum-mechanical transition.

FoM – Figure of Merit

Fermi level – A theoretical electron energy level at which at 0K, there is a 50% probability of it being occupied.

Fermi-Dirac function – A function that describes the probability that an energy level will be occupied by an electron at a given temperature.

HOPG (Highly orientated pyrolytic graphite) – A very high quality, synthetic graphite. A suitable flat substrate for 2D material or molecular transfer.

InP (Indium Phosphide) – A direct-gap semiconductor which is commonly used to make colloidal QDs.

LPE – Liquid Phase Exfoliation

ME – Micromechanical Exfoliation.

Photon – A single particle of light.

PDMS (Polydimethylsiloxane) – A polymer with advantageous properties for exfoliation, identification and transfer of 2D materials.

PL (Photoluminescence) – The emission of light from a material with a bandgap through excitation with another light source, usually a laser.

PUF (Physical Unclonable Function) – An object that, when challenged, generates a unique set of responses.

QD (Quantum Dot) – A small (nm scale) semiconductor, with optoelectronic properties highly-dependent on its size.

QNM – Quantitative Nanomechanical Mapping

QE – Quantum Efficiency

QY (Quantum Yield) – Number of photons emitted from a sample for each photon absorbed.

SEM – Scanning Electron Microscopy

SPR – Surface Plasmon Resonance

TMDC (Transition Metal Dichalcogenide) – A class of 2DM, which consists of a transition metal between two layers of chalcogen atoms, in the form MX_2, where M is a transition metal (e.g., W, Mo), and X is a chalcogen (e.g., S, Se).

WS_2 (Tungsten Disulphide) – A van der Waals crystal, which has attractive optical properties.

vdW Crystal (Van der Waals crystal) – A crystal that naturally occurs in layers. The intra-layer bonds are very strong, but the inter-layer bonds are weak, van der Waals bonds, enabling them to be easily separated.

VBM – Valence Band Maximum

ZnS (Zinc Sulphide) – A wide gap semiconductor, commonly used as a shell in core-shell quantum dots.